Search for the Higgs boson decaying to W^+W^- with associated jets and measurement of the W^+W^- production cross section and differential cross sections with jets in $p\bar{p}$ collisions at $\sqrt{s} = 1.96$ TeV

By

William Chesluk Parker

A dissertation submitted in partial fulfillment of
the requirements for the degree of

Doctor of Philosophy

(Physics)

at the
UNIVERSITY OF WISCONSIN–MADISON
2014

Date of final oral examination: December 17, 2014

The dissertation is approved by the following members of the Final Oral Committee:

Matthew F Herndon, Professor, Physics
Robert Mathieu, Professor, Astronomy
Yang Bai, Assistant Professor, Physics
Yibin Pan, Associate Professor, Physics
Stefan Westerhoff, Professor, Physics

SEARCH FOR THE HIGGS BOSON DECAYING TO W^+W^- WITH ASSOCIATED JETS AND MEASUREMENT OF THE W^+W^- PRODUCTION CROSS SECTION AND DIFFERENTIAL CROSS SECTIONS WITH JETS IN $P\bar{P}$ COLLISIONS AT $\sqrt{S} = 1.96$ TEV

William Chesluk Parker

Under the supervision of Professor Matthew Herndon

At the University of Wisconsin-Madison

A cross section measurement for the production of W^+W^- is performed. Differential measurements are reported as a function of jet multiplicity and transverse energy. The inclusive cross section is measured to be $\sigma(p\bar{p} \to W^+W^- + X = 14.0 \pm 0.6(\text{stat})^{+1.2}_{-1.0}(\text{syst}) \pm 0.8(\text{lumi})$ pb, consistent with the Standard Model prediction. Additionally, a search for the Higgs boson is performed in the final state of W^+W^- with two or more associated jets. Limits on the production cross section are set at the 95% confidence level, and combined with limits from related analyses. Both analyses use data collected by the CDF II detector from $9.7\,\text{fb}^{-1}$ of luminosity

Matthew Herndon

To my wife Dana Craft-Parker

ACKNOWLEDGMENTS

First and foremost I wish to acknowledge my tremendous debt to my advisor, Professor Matthew Herndon. This work was made possible by his insight, guidance, and support. Thanks are also due to University of Wisconsin CDF Professors Duncan Carlsmith and Lee Pondrom for their invaluable knowledge and experience. I am grateful to Professor Wesley Smith and the University of Wisconsin CMS group who introduced me to high energy experiment, and to Professor Lisa Everett, for her advice and encouragement. Thanks to my committee: Professors Yang Bai, Robert Mathieu, Yibin Pan, and Stefan Westerhoff.

Thanks also to the University of Wisconsin administrative staff, especially Aimee Lefkow, Renee Lefkow, and Giles Hietpas.

The research presented in this thesis could not have been done without the hard work of the many people who designed, built, and operated the Tevatron accelerator and the CDF detector. I wish to thank Eric James, Sergo Jindariani, and the CDF HWW group on whose work these analyses depend. I am similarly grateful to Dave Toback, Bo Jayatilaka, Christina Mesropian, Mark Kruse, Mark Lancaster, and Vadim Rusu for their help with the approval process for the WW cross section measurement.

I wish to thank my fellow graduate students at the University of Wisconsin, Andrea Peterson, Bethany Reilly, Ian Ross, Kenneth Rudinger, Ian Wisher, and others too numerous to mention for their companionship and conversation.

Finally I wish to thank my family. My father, John Parker, introduced me to science. My mother, Celia Chesluk, ensured my education. My sister, Maya Chesluk Parker, inspires me with her determination and enthusiasm. And my wife, Dana Craft-Parker is a source of strength and support.

TABLE OF CONTENTS

Page

Page

Page

LIST OF TABLES

Table Page

LIST OF FIGURES

Chapter 1

Introduction

The Standard Model of particle physics is a theoretical model that describes the nature of matter and its interactions through three fundamental forces: the electromagnetic force, the weak nuclear force, and the strong nuclear force. The Standard Model enjoys unparalleled success in describing the behavior of particles. The search for the Higgs boson is a test of two critical predictions of the Standard Model: The means by which particles acquire mass, and the source of the difference in strength between the weak and electromagnetic forces at low energy scales. At the same time, advances in theoretical techniques have made it possible to calculate the rates of production and decay to higher precisions and for processes complicated by additional strong force interactions. These processes can share the experimental signature of new physics events, making accurate calculation and simulation necessary for new physics searches, including that for the Higgs boson. This thesis describes a search for the Higgs boson in events with two W bosons and two or more jets, and a measurement of the production rate of W boson pairs. Both analyses use the Collider Detector at Fermilab to study collisions in the Tevatron, a proton-antiproton collider operating at a center of mass energy of 1.96 TeV. Chapter 2 gives an overview of the Standard Model of particle physics, its scope and history, and the means by which particles and their interactions are described. Chapter 3 discusses the Standard Model processes that are the focus of this thesis: Higgs and diboson production. Chapter 4 presents the experimental foundations of our understanding of electroweak physics, as well as other searches and measurements of Higgs and diboson

production. The experimental setup used in this analysis, the Tevatron collider and the Collider Detector at Fermilab, is described in Chapter 5. The method by which an event is reconstructed from a measurement in the detector is detailed in Chapters 6-7. The analysis begins with selection of events described in Chapter 8. The Standard Model processes that appear in this selection are investigated in Chapter 9, and means of distinguishing the processes of interest are given in Chapter 10. In Chapter 11, the W boson pair production cross section as a function of jet multiplicity and energy is presented, while Chapter 12 sets limits on the mass of the Higgs boson in events with two or more jets, and combines the result with other high mass subchannels.

Chapter 2

The Standard Model

The development of the Standard Model of particle physics (SM) was the primary task of theoretical particle physics for the latter half of the 20^{th} century. The first of the forces to be understood as we do today was the electromagnetic force. Feynman[1], Tomonaga[2], and Schwinger[3], working independently, formulated quantum electrodynamics(QED) in its covariant and gauge invariant form. The Standard Model describes the particles that make up matter and the forces through which they interact at the sub-atomic scale. Particles can be divided by their spin (intrinsic angular momentum) into fermions and boson. The particles that make up matter are fermions, while the force-carrying particles are bosons. The fermions can be divided into quarks, which interact via the strong nuclear force, and leptons, which do not. The fermions can then be further organized into generations which share certain properties such as electrical charge which further dictate via which forces the particles interact, shown in Table 2.1. With the possible exception of neutrinos, higher generations have higher mass than their lower-generation counterparts. Because of the ability of the weak nuclear force to interact across generations, these higher generations are unstable against weak decays. As a result, ordinary matter is composed entirely of bound states of particles of the first generation. The Standard Model is a gauge field theory, which starts from the requirement that physical observables be invariant under local gauge transformations. This requirement leads to the introduction of gauge fields which interact with particles that carry conserved charges. The interactions mediated by the vector bosons listed in

				1st Generation		2nd Generation		3rd Generation	
s	Q	T_3	C	f	mc^2/eV	f	mc^2/eV	f	mc^2/eV
$\frac{1}{2}$	$\frac{2}{3}$	$\frac{1}{2}$	1	u	$2.3^{+0.7}_{-0.5} \times 10^6$	c	$1.28 \pm 0.03 \times 10^9$	t	$173.1 \pm 0.9 \times 10^9$
$\frac{1}{2}$	$-\frac{1}{3}$	$-\frac{1}{2}$	1	d	$4.8^{+0.5}_{-0.3} \times 10^6$	s	$95 \pm 5 \times 10^6$	b	$4.18 \pm 0.03 \times 10^9$
$\frac{1}{2}$	0	$\frac{1}{2}$	0	ν_e	< 2.2	ν_μ	$< 170 \times 10^3$	ν_τ	$< 15.5 \times 10^6$
$\frac{1}{2}$	-1	$-\frac{1}{2}$	0	e	0.511×10^6	μ	106×10^6	τ	$1776.8 \pm 0.2 \times 10^6$

Table 2.1 The fermions of the Standard Model. Each fermion f has spin s, electric charge Q, weak isospin T_3 (only if left-handed), and mass m. Presence or absence of color charge is indicated by C, with each quark having one unit of red, blue, or green. Each fermion listed has a corresponding antiparticle with mass m, charge $-Q$, and weak isospin $-T_3$. The rows are referred to respectively as up-type quarks, down-type quarks, neutrinos, and charged leptons.

Table 2.2 correspond to invariance of the Standard Model Lagrangian under three groups of transformations

$$SU(3)_C \times SU(2)_L \times U(1)_Y \tag{2.1}$$

discussed below. We are studying processes involving multiple W bosons and the Higgs boson, which interacts with the W and other particles to give them mass.

2.1 Quantum Chromodynamics

We study the W and Higgs bosons by producing them in proton-antiproton collisions. This means that our initial state will always be composed of quark and gluons. Quantum Chromodynamics (QCD) describes their interactions via the strong nuclear force. Quarks carry one of three color charges (labeled red, blue and green) corresponding to the fundamental representation of the $SU(3)_C$ group. Antiquarks carry anticolor charges, while gluons carry one of eight combinations of color and anticolor charge corresponding to the adjoint representation. A notable feature of QCD is its non-abelian nature. In order to preserve gauge invariance, the gluons must carry color charge, and so can self-interact. The

s	Q	T_3	C	Boson	mc^2/eV	Interaction
1	0	0	0	γ	0	Elecromagnetic
1	±1	±1	0	W	$80.39 \pm 0.02 \times 10^9$	Weak
1	0	0	0	Z	$91.188 \pm 0.002 \times 10^9$	Weak
1	0	0	1	g	0	Strong
0	0	0	0	H	$125.9 \pm 0.4 \times 10^9$	–

Table 2.2 The bosons of the Standard Model. Each boson has spin s, electric charge Q, weak isospin T_3, and mass m. The gluon is the only boson with color charge, carrying a superposition of color and anticolor.

fundamental interactions of QCD are a quark-antiquark-gluon coupling, a three gluon vertex, and a four gluon vertex shown in Figure 2.1. The strength of the strong interaction is determined by the coupling constant α_S. α_S exhibits assymptotic freedom, with a strength that decreases as energy scale increases. In interactions involving production of a Higgs or a WW pair, α_S is of order 0.1. Due to the strength of this coupling, a significant fraction of these events will have one or more additional radiated strongly interacting particles, making perturbative QCD an essential tool to fully describe the process of interest. In the calculation of amplitudes for higher order processes infinities can appear. These infinities are eliminated by imposing an energy cutoff in the calculation, referred to as regularization. The resulting dependence on the cutoff energy is cancelled by varying quantities such as charge and mass with the cutoff energy, effectively renormalizing the charge and mass to measured values. The value of the quantity is then specified at a specific (arbitrary) energy scale, the renormalization scale. In QED, a natural choice for this scale is zero, but in QCD this is exactly where α_S is large, invalidating a perturbative approach. As a result, a choice of scale μ_R must be made. The scale would not affect the calculation of an observable if a sum of all orders in perturbation theory could be calculated. For smaller coupling constants the scale will have less of an effect on a truncated perturbative series. For α_S of order 0.1 a second order calculation, known as a Next-to-Leading Order (NLO) calculation will typically converge to good accuracy.

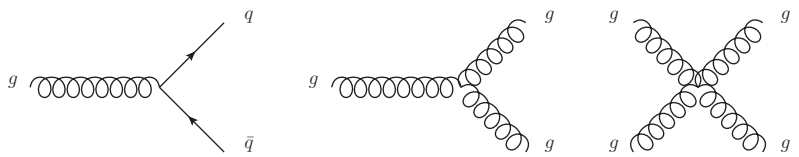

Figure 2.1 The fundamental QCD interactions

The nature of the running of the α_S coupling makes it energetically favorable for quarks to hadronize into color-neutral bound states of one quark and one anti-quark (a meson) or three quarks or anti-quarks (a hadron), referred to as quark confinement. An energetic parton (quark or gluon) produces many more partons (parton showering) which hadronize. The timescale on which this process ocurrs means that the particles produced in high energy collisions are only detected after parton showering and hadronization has occurred. The large strong coupling constant even at high energies and the mix of perturbative and non-perturbative behaviors that have to be understood make the prediction of cross sections and differential properties in hadron colliders difficult and an area of active study experimentally and theoretically.

2.2 The Electroweak Model

W bosons are produced through the electroweak interaction, either by radiation or annihilation of fermions, or through interaction with gauge bosons. Together, $SU(2)_L \times U(1)_Y$ describe the mixing and unification of the electromagnetic and weak forces, achieved by Glashow[4], Weinberg[5], and Salam[6]. $SU(2)_L$ describes three vector fields W_μ which couple to weak isospin with strength g, while $U(1)_Y$ describes one vector field B_μ which couples to hypercharge Y with strength g'. Only left-handed particles couple to weak isospin. The electroweak Lagrangian describes the interactions of the weak bosons with fermions:

$$\mathcal{L}_{fermion} = \bar{R}\gamma^\mu(i\partial_\mu - g'\frac{Y}{2}B_\mu)R + \bar{L}\gamma^\mu(i\partial_\mu - g\frac{1}{2}\tau \cdot W_\mu - g'\frac{Y}{2}B_\mu)L \tag{2.2}$$

Where L denotes a left-handed fermion doublet and R a right-handed fermion singlet. τ are the Pauli isopsin matrices. As in QCD the non-abelian structure of the theory results in self-interactions between the gauge bosons, described by:

$$\mathcal{L}_{gauge} = -\frac{1}{4}W_{\mu\nu} \cdot W^{\mu\nu} - \frac{1}{4}B_{\mu\nu}B^{\mu\nu} \tag{2.3}$$

The forces we observe in nature are described by a superposition of the W_μ and B_μ fields. The charged weak, neutral weak, and electromagnetic fields are given by

$$W_\mu^\pm = \frac{1}{\sqrt{2}}(W_\mu^1 \mp W_\mu^2) \tag{2.4}$$

$$Z_\mu = -B_\mu \sin\theta_W + W_\mu^3 \cos\theta_W \tag{2.5}$$

$$A_\mu = B_\mu \cos\theta_W + W_\mu^3 \sin\theta_W \tag{2.6}$$

Where θ_W, the Weinberg angle, is given by $\tan\theta_W = g/g'$. The fundamental electroweak interactions are a photon coupling to charged fermion-antifermion pair, a Z coupling to a fermion anti-fermion pair, a W boson coupling to a charged lepton and neutrion or an up type and down type quark, and any coupling of two W bosons to one or two vector bosons that conserves electric charge. These vertices are shown in Figure 2.2. In our analysis, W bosons can be radiated from quarks/antiquarks or produced through coupling to other vector bosons, while we will study decay to a charged lepton and neutrino. The probabilities for electromagnetic and weak interactions both include a factor $g^2/(M^2+q^2)$. For the electromagnetic interaction, the mass of the photon is zero and this reduces to 1/137. However in the weak interaction the mass of the vector bosons cannot be neglected, and indeed dominates at low energies, reducing this factor to the Fermi constant: $G_F = \frac{\sqrt{2}g^2}{8M_W^2} = 1.17 \times 10^{-5}$ GeV^{-2}. The lesser strength of the weak interaction at low energies is a consequence of the mass of the weak bosons. This lesser strength means that self-interaction of the weak bosons does not lead to the non-perturbative behavior observed in QCD. The means by which the W and Z bosons acquire mass is discussed below. A unique property of the charged weak interaction is the ability to interact across generations of fermions. Because this interaction

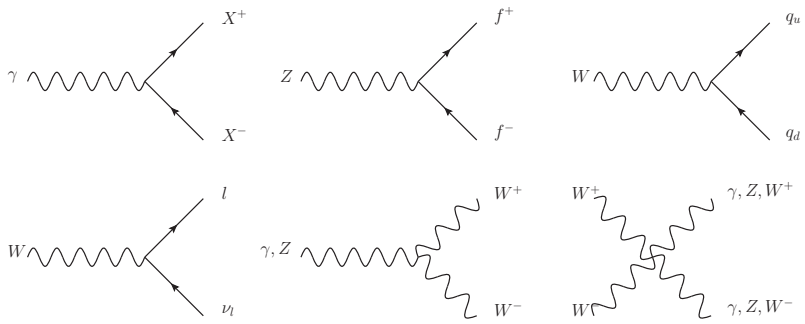

Figure 2.2 The fundamental electroweak interactions

is weak it occurs on a longer time scale than other interactions, being observed when there is no other possibility, for example in the decay of a b-quark.

2.3 Electroweak Symmetry Breaking and the Higgs Mechanism

The mechanism by which the W and Z bosons acquire mass was proposed independently by Brout and Englert[7], by Higgs[8], and by Guralnik, Hagen, and Kibble[9]. Including a simple mass term for the bosons is forbidden by the requirement of gauge invariance. An $SU(2)$ doublet of scalar fields ϕ is introduced with potential

$$V = \mu^2 \phi^\dagger \phi + \frac{\lambda^2}{2}(\phi^\dagger \phi)^2 \tag{2.7}$$

A negative value of μ^2 results in a degenerate minimum with non-zero expectation value which we can choose to be $\phi_0 \equiv \sqrt{\frac{1}{2}}\binom{0}{v}$, with $v = \sqrt{-\frac{\mu^2}{\lambda}}$. Substituting into the Higgs part of the Lagrangian

$$\mathcal{L}_{scalar} = |(i\partial_\mu - g\frac{1}{2}\tau \cdot W_\mu - g'\frac{Y}{2}B_\mu)\phi|^2 - V(\phi) \tag{2.8}$$

We can reorganize the Higgs part of the Lagrangian:

$$\mathcal{L}_H = \frac{1}{2}\partial^\mu H \partial_\mu H + \frac{1}{4}g^2 v^2 W^+_\mu W^{-\mu} + \frac{1}{8}\frac{g^2 v^2}{\cos^2(\theta_W)} Z_\mu Z^\mu + \frac{1}{2}g^2 v H W^+_\mu W^{-\mu}$$
$$+\frac{1}{4}\frac{g^2 v}{\cos^2(\theta_W)} H Z_\mu Z^\mu + \frac{1}{4}g^2 H^2 W^+_\mu W^{-\mu} + \frac{1}{8}\frac{g^2}{\cos^2(\theta_W)} H^2 Z_\mu Z^\mu - \lambda v^2 H^2 - \lambda v H^3 - \frac{1}{4}\lambda H^4 \tag{2.9}$$

Where we can observe quadratic terms, which are identified as a self energy associated with the particle, i.e. interpreted using Einstein's relativistic equivalence of mass and energy, $E = mc^2$, a mass.

$$M_W = \frac{1}{2}gv \tag{2.10}$$

$$M_Z = \frac{M_W}{\cos\theta_W} \tag{2.11}$$

Along with couplings to the Higgs in proportion to their mass squared. The symmetry of $SU(2)_L \times U(1)_Y$ is broken, only the $U(1)_{em}$ symmetry and massless photon remain. Three of the four introduced degrees of freedom go into the longitudinal components of the $W^\pm$ and Z The remaining degree appears as a spinless scalar particle of mass $M_H = \lambda v$, the Higgs boson. Note that λ is a new parameter, without a predicted value. As a result the physical value of the Higgs mass cannot be determined *a priori*. The Higgs field couples to fermions proportionally to their mass via the Yukawa couplings, which must also be determined experimentally. The discovery of the Higgs boson completes the Standard Model picture, and illuminates the observed difference in strength of the electromagnetic and weak forces.

$$\mathcal{L}_Y = -\sum_f \frac{m_f}{v} H \bar{f} f \tag{2.12}$$

Chapter 3

Phenomenology of Higgs and Diboson Production and Decay

3.1 Diboson Production and Decay

As discussed in Chapter 2, the W boson interacts with leptons, quarks, and electroweak bosons. Because the Tevatron is a proton-antiproton collider, W bosons are most commonly produced in quark-antiquark interactions via radiation or quark anti-quark annihilation. The W boson decays to either leptons or hadrons, with branching ratios shown in Table 3.1. While the branching ratio for leptonic decay is lower than hadronic, leptonic decays are more easily separated from background, as the production of leptons is rare compared to the large production rate of quark or gluon jets in strong interactions between the constituents of the proton and anti-proton. For this reason we only consider the leptonic final state in this analysis, as shown in Figure 3.2.

Mode	Fraction (Γ_i/Γ)
$e\nu$	$(10.75 \pm 0.13)\%$
$\mu\nu$	$(10.57 \pm 0.15)\%$
$\tau\nu$	$(11.25 \pm 0.20)\%$
hadrons	$(67.60 \pm 0.27)\%$

Table 3.1 Branching ratios of W boson decay

Occasionally, two W bosons might be produced in the same event, referred to as diboson production. While this is much rarer than single boson production, it is still readily observable at the Tevatron. Figure 3.1 shows some simple examples of W^+W^- (WW) production with zero, one, and two jets. Note that the diagrams shown have the least number of vertices possible to produce the final state of interest. Experimentally, we cannot discriminate between these diagrams and more complicated ones with additional internal vertices. However, the small size of the weak coupling constant means that the contribution of diagrams with additional vertices are greatly suppressed and leading order diagrams dominate the total production rate. For strong interactions this is not necessarily the case, making higher orders especially important for understanding QCD processes. Events with associated jets are of particular interest because they must be higher order in QCD and test our ability to predict complex topologies involving multiple vector bosons and multiple jets using combinations of perturbative and non-perturbative techniques. Other WW analyses have looked for new physics via an anomalous gauge coupling, but we do not do so here, instead concentrating on looking for new physics directly in the form of production and decay of Higgs bosons to WW.

The WW cross section has been calculated at Next-to-Leading order with MCFM [10] and MC@NLO [11]. Included in the NLO diagrams are both diagrams with a parton in the WW final state and diagrams involving an extra internal QCD loop interaction. However, as discussed in Section 2.1 any additional partons will fragment and hadronize before being observed as jets in the final state. This process is non-perturbative, and is accounted for by interface to a specialized parton shower model such as Pythia [12]. As this process involves the radiation of additional partons and the grouping of quarks into hadrons it can result in additional quark jets. Another approach used to model WW production with associated jets is fixed order generation, for example with Alpgen [13]. The fixed order calculation performs separate leading order calculations in perturbation theory and generates discrete samples for zero jets, one jet, and so on up to a specified n jets. Both of these methods can result in

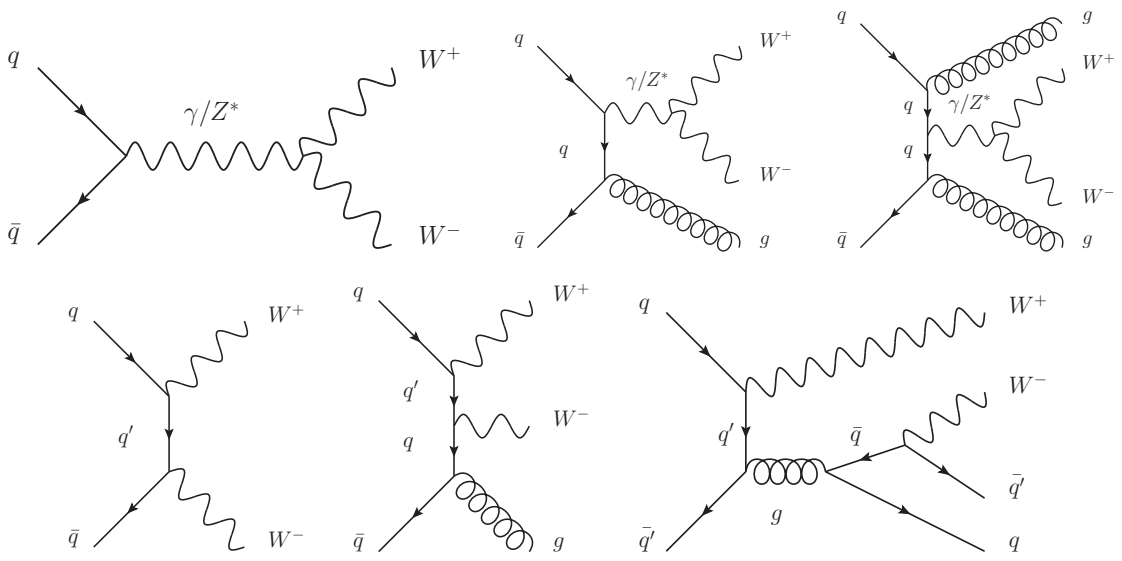

Figure 3.1 Examples of diboson production with zero, one, or two associated jets from left to right

events with two W bosons and multiple jets. Events with two jets result from direct simulation in the fixed order case and from $WW + 1$ jet at NLO with an additional jet produced in the parton shower process in the NLO case. For a given number of jets, events produced directly by the NLO method would be expected to more accurately simulate the total cross section and differential distribution of the process. Thus NLO would be expected to be more accurate for $WW + 0$ jet and $WW + 1$ jet events. In the $WW + 2$ jets case, fixed order simulation has the advantage of directly producing the final state of interest while an NLO simulation has the advantage of including the NLO effects. Comparing the two methods is of interest to determine which method is more accurate. Final states involving two vector bosons and two jets occur in new physics searches, studies of electroweak symmetry breaking using the vector boson scattering process where one way vector bosons can scatter is via a Higgs boson, and, as examined in this thesis, direct searches for the Higgs boson.

Predictions for the inclusive WW cross section are shown in Table 3.2.

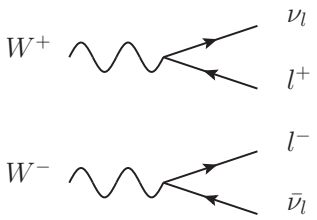

Figure 3.2 Two W bosons decaying leptonically

Generator	σ_{Exp}(fb)	Uncertainty(fb)
MCFM	11.34	$\pm$0.70
MC@NLO	11.3	$\pm$0.9
Alpgen	11.7	$\pm$1.4

Table 3.2 Cross sections and uncertainties for non-resonant WW production

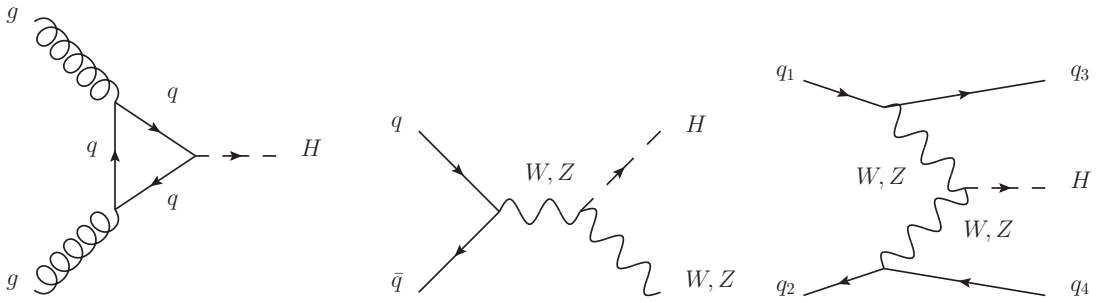

Figure 3.3 Dominant methods of Higgs boson production from left to right: gluon fusion, associative production, and vector boson fusion

3.2 Higgs Production and Decay

The Higgs boson is predicted as a consequence of the Higgs mechanism. It is the final particle predicted by the Standard Model to be discovered. The Higgs is neutral, spin zero, and scalar, and couples directly to fermions in proportion to their mass and vector bosons in proportion to their mass squared, as shown in Equations 2.9- 2.12. Direct production of the Higgs via the initial state quarks and gluons is not expected, as they have small and zero masses, respectively. Production instead occurs indirectly via the couplings discussed above, and three modes dominate at the Tevatron, shown in Figure 3.3. The dominant method is gluon fusion, via the coupling of the gluon to the top quark loop. Additionally, the quarks couple to the vector bosons, meaning that associative production(VH) where the Higgs is radiated from a W or Z, and vector boson fusion(VBF) where a virtual W or Z pair fuse to form a Higgs boson also contribute significantly to the overall rate. Production and decay rates are shown in Figure 3.4 and 3.5 as a function of Higgs mass. Production and decay rates both depend on couplings of particles to the Higgs (and to the initial state partons) and energy considerations, with particles much less likely to be produced far off shell and sufficient energy in the initial partons necessary to produce the final state. For $m_H > 130$ GeV, the dominant decay mode is a WW pair. While the ZZ branching ratio is significant, the $Z \to ll$ branching ratio is lower than $W \to l\nu$. Additionally, the angular acceptance of the CDF detector limits the number of events in which all four leptons from a $H \to ZZ \to lll'l'$ decay can be reconstructed. For $m_H < 130$ GeV, the dominant decay modes is to a $b\bar{b}$ pair. However, due to the difficulty of distinguishing $H \to b\bar{b}$ from the background of multijet events, the $H \to WW$ channel contributes significantly to the sensitivity of Higgs searches at low mass. An irreducible background to the $H \to WW$ search is non-resonant WW production, discussed above.

The dominant Higgs production mechanism, gluon fusion, is a QCD process that proceeds via a loop. At leading order, the cross section is proportional to $\alpha_S^2(\mu^2)$, resulting in a large scale uncertainty [14]. The NLO [15] [16] [17] prediction at the Tevatron is typically a factor

Process	σ_{Exp}(fb)	Uncertainty(fb)
ggH	949.3	$\pm$107.5
WH	130	$\pm$6.5
ZH	78.5	$\pm$3.9
VBF	65.3	$\pm$6.5

Table 3.3 Expected cross sections and uncertainties of 125 GeV Higgs production processes

of two larger than the LO [18] prediction, and the NNLO [19] [20] prediction is another factor of 1.4 larger, due largely to additional classes of diagrams that enter at these orders. The NNLO calculations incorporate contributions from both top and bottom quark loops, effects of finite quark masses, electroweak contributions from two-loop diagrams, interference effects from mixing of electroweak and QCD contributions, leading logarithmic resummation of soft gluon contributions, and MSTW2008 NNLO parton distribution functions [21]. Uncertainties in the NNLO cross section calculation are evaluated by studying the effect on the result of factorization and renormalization scale choices. We take an uncertainty on the production cross section corresponding to the shift observed when these scales are varied coherently upwards and downwards by factors of two. The uncertainty on the inclusive gluon fusion cross section is found to be 11.3%, and calculations that have been performed including the primary amplitudes at NNNLO indicate that no additional large modification of the cross section is expected [22]. Vector boson fusion and associative production are electroweak processes. As a result, the NLO and NNLO calculations used for VBF [23] [24] [25] and VH [26] [27] [23] [28] [29] have associated uncertainties of 10% and 5% respectively. Values and associated uncertainties for the cross section are shown for 125 GeV Higgs boson in Table 3.3.

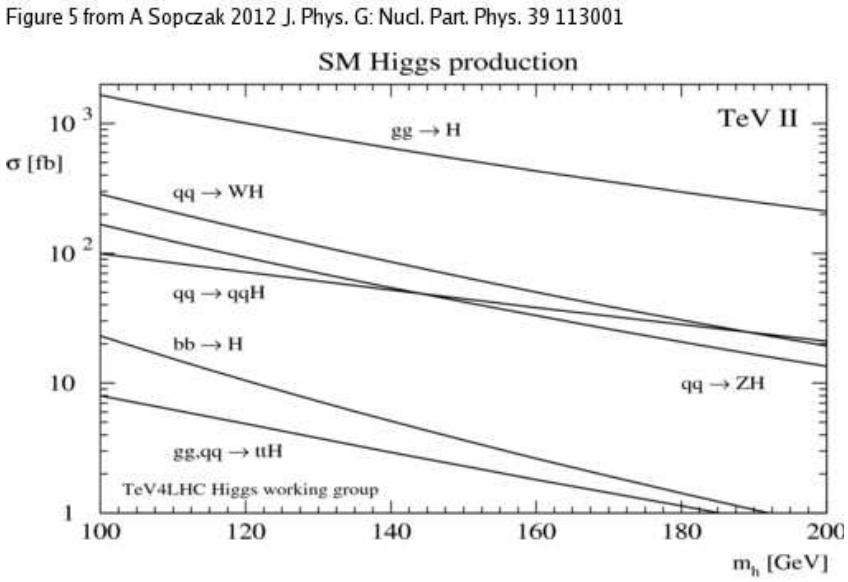

Figure 3.4 Cross section for Higgs boson production as a function of Higgs mass

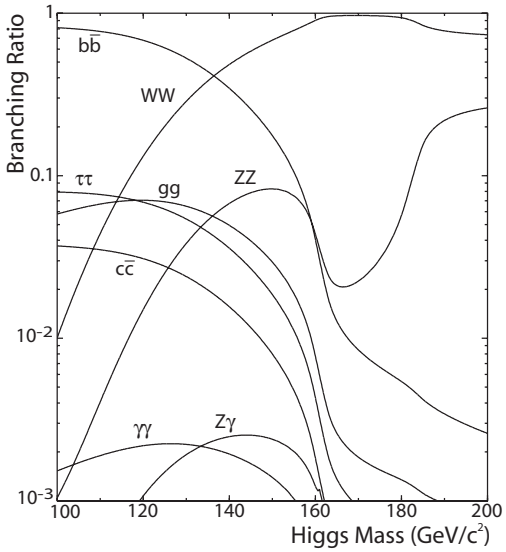

Figure 3.5 Branching ratios of Higgs boson decay as a function of Higgs mass

Chapter 4

Previous Measurements

4.1 Previous Diboson Results

The W boson was first observed in 1983 at the Super Proton Synchrotron(SPS) by the UA1[30] and UA2[31] experiments, confirming a fundamental prediction of Glashow's electroweak theory. The W was observed in the leptonic decay channel, as a single electron with substantial missing transverse energy due to the neutrino. The reconstructed mass was found to be consistent with theoretical predictions. The SPS was used to accelerate electrons and positrons for the Large Electron-Positron Collider(LEP), which began running in 1989. LEP collided electrons and positrons, allowing a precise center of mass energy to be achieved. During LEP phase two, the center of mass energy was gradually increased, reaching the threshold for production of a W boson pair, observed by all four experiments [32][33][34][35] in $ll\nu\nu$ events. WW production at the Tevatron was first observed by CDF[36] during run I. Both CDF and D0 reported higher statistics WW cross section measurements in leptonic decays during run II CDF[37], D0[38]. Most recently, both ATLAS [39] [40] and CMS [41] [42] have measured the WW production cross section at the LHC. In all of the measurements discussed below, the W^+W^- pair is decaying to a final state of $l^+\bar{\nu}l^-\nu$, referred to as $ll\nu\nu$. Results from the Tevatron and LHC are shown in Table 4.1. Note that in order to simplify analysis and reduce the $t\bar{t}$ background previous measurements have employed a jet veto (though D0 has also made an inclusive measurement [43]). No differential measurement of WW+jets has been previously made.

$\sqrt{s}$	Experiment	Luminosity	Cross Section	Prediction	Jet Info
1.96 TeV	D0	9.7fb^{-1}	11.6 ± 0.7 pb	11.3 ± 0.7 pb	Veto $p_T > 20$ GeV
					$N > 1$
	CDF	3.6fb^{-1}	$12.1^{+1.8}_{-1.6}$ pb	11.7 ± 0.7 pb	Veto $E_T > 15$ GeV
7 TeV	ATLAS	4.6fb^{-1}	51.9 ± 4.8 pb	$49.04^{+1.03}_{-0.88}$ pb	Veto $p_T > 25$ GeV
	CMS	4.9fb^{-1}	52.4 ± 5.1 pb		Veto $E_T > 30$ GeV
8 TeV	CMS	3.5fb^{-1}	69.9 ± 7.0 pb	$59.84^{+1.32}_{-1.14}$ pb	Veto $p_T > 30$ GeV
	ATLAS	20.3fb^{-1}	$71.4^{+5.6}_{-5.0}$ pb	$58.7^{+3.0}_{-2.7}$ pb	Veto $p_T > 25$ GeV

Table 4.1 Previous Tevatron and LHC WW production cross section measurements

4.1.1 D0

The current D0 measurement is an extension of the Higgs search in the WW final state, using the full 9.7fb^{-1} dataset. Events are required to have exactly two high-p_T leptons of opposite charge originating from within 2 cm along the beamline from each other. The highest p_T lepton, or electron in an $e\mu$ event, is required to have $p_T > 15$ GeV, the subleading or muon (in $e\mu$) $p_T > 10$ GeV. In same-flavor final state m_{ll} is required to be greater than 15 GeV. Boosted decision trees are trained on kinematic variables to discriminate against Drell-Yan, and a cut is applied. A second set of boosted decision trees is trained separately on lepton flavor combinations, and zero and one jet events. In addition to kinematic variables, lepton reconstruction quality and b-tagging variables are also included. Events with more than one jetof $p_T > 20$ GeV are vetoed. The cross section $\sigma(p\bar{p} \rightarrow WW)$ is measured to be 11.6 ± 0.7 pb, consistent with the Standard Model prediction of 11.3 ± 0.7 pb.

4.1.2 CDF

The previous CDF measurement uses 3.6fb^{-1} of data, also collected with high-p_T single-electron and single-muon triggers. Electrons are selected by cuts on calorimeter and track information. Muons can be identified by the muon detectors, but also by a track pointing only to the calorimeter, with energy deposition consistent with a muon. Finally, a category is included for isolated tracks not fiducial to the calorimeter. Isolated tracks at high transvserse momentum are enriched in charged leptons from vector boson decay, but the candidate type cannot be identified as either an electron or muon, and is treated as either in the event selection. Two leptons of opposite charge are required, and Drell-Yan is suppressed by a requirement on the variable

$$\not\!\!E_{T,spec} \equiv \begin{cases} \not\!\!E_T & \text{if} \Delta\phi(\vec{\not\!\!E}_T, lepton, jet) > \frac{\pi}{2} \\ \not\!\!E_T sin(\Delta\phi(\vec{\not\!\!E}_T, lepton, jet) & \text{if} \Delta\phi(\vec{\not\!\!E}_T, lepton, jet) < \frac{\pi}{2} \end{cases} \tag{4.1}$$

Events in which the transverse energy of a lepton or jet is undermeasured may have substantial apparent $\not\!\!E_T$, but it will tend to be parallel to the mismeasured object, resulting

in a minimal contribution to the $\not\!\!E_{T,spec}$. The $t\bar{t}$ background is almost entirely rejected by vetoing events with one or more jets. Kinematic cuts are kept deliberately loose to maximize acceptance. Matrix element probabilities are calculated with MCFM[44], based on the kinematics of leptons and $\not\!\!E_T$, for WW, ZZ, $W\gamma$, and W+jets. The matrix element probabilities are combined in a likelihood ratio that serves as the final discriminant. The cross section is extracted from the shape and normalization of the likelihood ratio distributions via a binned maximum likelihood method. The measured cross section, $\sigma(p\bar{p} \rightarrow WW) = 12.1^{+1.8}_{-1.6}$(stat+syst+lumi) pb is consistent with the Standard Model expectation of 11.66±0.7 pb.

4.1.3 ATLAS and CMS

The ATLAS and CMS collaborations have made recent measurements of the WW production cross section at both 7 and 8 TeV. Both experiments collect data with a combination of single and dilepton triggers. Events are selected with exactly two oppositely charged leptons and considerable $\not\!\!E_T$. Both experiments identify electrons via a likelihood-based method using calorimeter and tracking information, and muons via a cut-based method using the tracker and muon spectrometer. The high luminosity of the LHC allows (and requires) relatively tight lepton quality requirements. Substantial $\not\!\!E_{T,rel}$, defined above, is required and related variables taking advantage of vertex information are used to maintain effectiveness of the selection with increasing pileup. The dominant background to this measurement at the LHC is top quark pair production, and extraordinary measures must be taken to suppress it. Both experiments veto events with one or more jets over some transverse energy threshold. CMS additionally vetos events with jets below threshold identified as originating from a b quark. Further rejection of Drell-Yan is achieved by requiring that the invariant mass of the lepton pair not be too low or too close to the mass of the Z, and cuts on the ϕ distribution of leptons and $\not\!\!E_T$. The cross section can be determined by background subtraction in the signal region, as is done by CMS, or by a likelihood fit, as done by ATLAS. At 7 TeV, CMS measures a cross section of 52.4±5.1 pb using 4.9fb^{-1} of data, while ATLAS measures a cross

section of 51.9 ± 4.8 pb in 4.6fb^{-1}. At 8 TeV, CMS measures a cross section of 69.9 ± 7.0 pb with 3.5fb^{-1} of data and ATLAS measures a cross section of $71.4^{+5.6}_{-5.0}$ pb in 20.3fb^{-1}. These results are consistent with the most recent NNLO predictions [45]: $49.04^{+1.03\%}_{-0.88\%}$ at 7 TeV and $59.84^{+1.32\%}_{-1.14\%}$ at 8 TeV. Note that this includes an irreducible contribution from $gg \to H \to WW^*$, which is negligible at the lower energy of the Tevatron.

4.2 Previous Higgs Results

At LEP, the Higgs boson was searched for through primarily through ZH production. The cross section is extremely low below the production threshold $E_{CM} = m_H + m_Z$. Data from each center of mass energy and experiment was combined to set a lower bound of 114.4 GeV on the mass for a SM Higgs [46]. Prior to 2012, searches for the Higgs were conducted at both the Tevatron and LHC.

4.2.1 Tevatron Combination

At the Tevatron, the CDF and D0 collaborations searched for the Higgs boson in the bb WW, ZZ, $\tau\tau$, and $\gamma\gamma$ final states. In 2011, a combination of results from both experiments was published [47] using up to 8.6fb^{-1} of data from each experiment. Different channels are combined by Bayesian and CL$_S$ methods, accounting for correlations of systematic uncertainty between analysis channels and experiments. The resultant limits are shown in Figure 4.1. The Tevatron combination excluded mass regions of $100 < m_H < 108$ GeV and $156 < m_H < 177$ GeV at a confidence level of 95%, consistent with the expectation, though an excess of $\sim$ one standard deviation was observed in the region from $125 < m_H < 155$ GeV. The channels with the most sensitivity to a Higgs boson are bb at low mass and WW at high mass.

4.2.2 LHC Initial Results

At the LHC, the nature proton proton collisions and the ATLAS and CMS detectors means that different channels have greater sensitivity to the Higgs boson. The improved

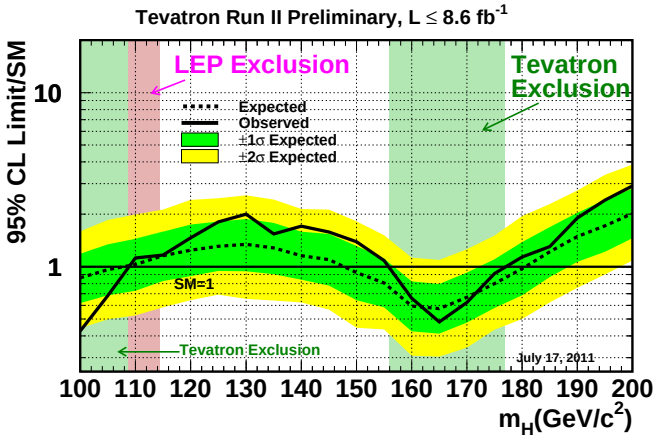

Figure 4.1 2011 Tevatron combination Higgs exclusion

lepton acceptance of the detectors makes full reconstruction of $H \rightarrow ZZ \rightarrow lll'l'$ decays feasible with good statistics. Similarly, improved detector resolution makes reconstruction of an invariant mass peak possible in the $H \rightarrow \gamma\gamma$ channel. The proton proton initial reduces the relative rate of associative production, which requires a quark anti-quark initial state. VH production is used as a handle to distinguish $H \rightarrow b\bar{b}$ from multijet backgrounds, and together with an increase in the multijet production rate the $H \rightarrow b\bar{b}$ channels is not as sensitive at the LHC. Each experiment published a combination of analysis channels using approximately 5fb^{-1} of data [48] [49]. CMS excluded the mass range of $127 < m_H < 600$ at 95% confidence, and a local excess of 3.1 standard deviations at 124 GeV was observed. ATLAS excluded ranges of $112.9 < m_H < 115.5$ GeV, $131 < m_H < 238$ GeV, and $251 < m_H < 466$ GeV, and observed an excess of 3.5 standard deviations around 126 GeV. Both results strongly indicated a need for further study in the low mass region.

4.2.3 Higgs Discovery

With additional data at 8 TeV, both LHC experiments observed evidence for a Higgs-like boson with ATLAS reporting a mass of 126.0 ± 0.6 GeV and a significance of 5.9σ [50], CMS a mass of 125.3 ± 0.6 GeV and significance of 5.0 standard deviations [51]. Measurements indicate that the Higgs bosons is a scalar, with couplings consistent with the Standard Model predictions. Of particular importance are the couplings of the Higgs to the W and Z bosons, necessary for its role in electroweak symmetry breaking.

Chapter 5

Experimental Setup

5.1 The Tevatron

The Tevatron was a proton-antiproton collider that operated from 1987 to 2011. The data used in this analysis was collected during Run II, which began in 2001. During Run II, the Tevatron operated at a center of mass energy of $\sqrt{s} = 1.96$ TeV and collected approximately 9.7fb^{-1} of data, with a peak luminosity of 4×10^{32}cm^{-2}s^{-1}, corresponding to an average of ~ 12 interactions per bunch crossing. Proton-antiproton collisions maximize the probability of a high-energy interaction between a valence quark and antiquark. However, creating and storing antiprotons is a limiting factor on the rate of collisions, The first step to proton-antiproton collisions was to produce a proton beam. Hydrogen was ionized and accelerated to an energy of 750 keV by a Cockroft-Walton device. The Hydrogen ions were accelerated by the Linac (linear accelerator) to 400 MeV and passed through a carbon foil to remove the remaining electrons, leaving a beam of protons. The protons were then passed to a synchrotron, called the Booster. Over the course of roughly 20,000 rotations, the protons were accelerated by radio frequency (RF) cavities to 8 GeV and passed to a multipurpose accelerator called the Main Injector. The Main Injector was an upgrade to the previous Main Ring that marked the beginning of Tevatron Run II, featuring superconducting, rather than conventional, magnets. The Main Injector served a number of purposes, the first of which was to accelerate protons to 120 GeV for antiproton production. At the antiproton source, this beam was collided with a fixed target of nickel. Antiprotons produced in the resulting collisions were selected via a lithium lens and dipole magnet, debunched and cooled

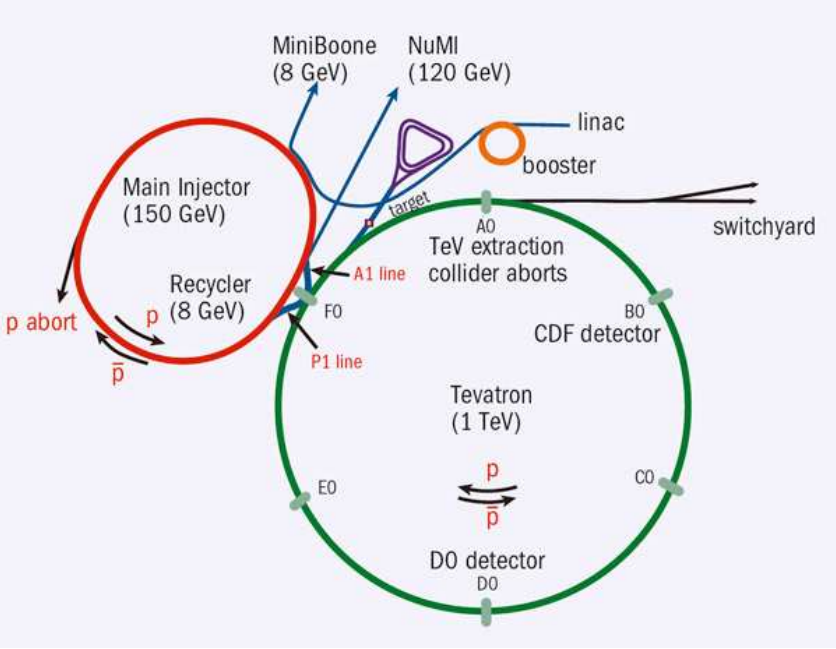

Figure 5.1 The Tevatron accellerator at Fermilab

in the Debuncher and cooled and accumulated in the Accumulator. Antiprotons are also stored in the Recycler, an 8 GeV fixed energy ring built to recycle antiprotons from the Tevatron. Because the Accumulator stacks antiprotons more rapidly with a smaller stack of antiprotons, a small stack was quickly accumulated and then stored in the Recycler, improving the overall stacking rate. Using the recycler for this purpose was more effective in increasing antiproton intensity than recycling antiprotons from the Tevatron. The next step was the second function of the Main Injector, accelerating both protons and Antiprotons to 150 GeV prior to injecting them into the Tevatron. The Tevatron is the 6.86km accelerator ring at which protons and antiprotons were collided. The beam itself consisted of 36 bunches of protons or antiprotons, arranged in 3 trains of 12 bunches each. Approximately 10^{13} protons and 10^{12} antiprotons circulated with a frequency of 47.7 kHz. Each bunch was separated by 396 ns, with a 2.6 μs abort gap between trains. Protons and antiprotons were accelerated to an energy of 980 GeV by RF cavities, focused, and collided. As the beams accelerated they were kept on track by dipole magnets with a field strength of up to 4.5T. Quadrupole magnets with a strength of 2.5T focused the beam in alternating planes, counteracting natural divergence. Collisions took place at two interaction points, the sites of the D0 and CDF detectors. Many of the steps described above, through the acccumulation of antiprotons in the Main Injector, could take place while collisions were already ocurring. After the beam was dumped, it took roughly half an hour to inject and accelerate protons and antiprotons, focus the beam, and remove the halo of particles far from the center of the beam. At this point, the detectors could be turned on and data taking could resume. A typical store started with a luminosity of $3.6 - 3.8 \times 10^{32}\text{cm}^{-2}\text{s}^{-1}$, decaying exponentially over the course of $12 - 18$ hours. As the luminosity approached $0.5 \times 10^{32}\text{cm}^{-2}\text{s}^{-1}$ the beam would be dumped and injection would begin again. Such a run would typically deliver $7 - 8$ pb^{-1}, collected with $80 - 90\%$ efficiency.

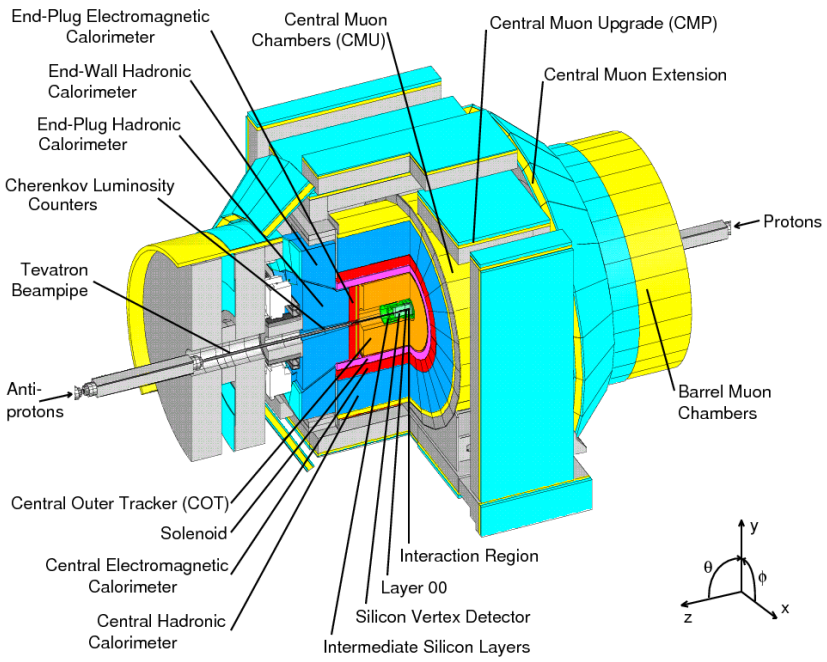

Figure 5.2 Cutaway model of the CDF detector

5.2 The CDF Detector

This analysis uses data collected with the Run II Collider Detector at Fermilab (CDF). CDF was a general-purpose particle detector with a cylindrical layout and aziuthal and forward-backward symmetry. The detector was made up of multiple layers serving complementary physics purposes, making it suitable to a wide variety of physics analyses. Throughout this work we describe positions and angles with a cylindrical coordinate system, where the origin lies at the center of the detector, and the z axis is directed along the proton beam. The azimuthal angle ϕ around the beam axis is defined with respect to a horizontal vector pointing outwards from the center of the Tevatron, and radii are measured with respect to the beam axis. The polar angle θ is defined with respect to the proton beam direction, and the transverse energy and momentum of a particle are defined as $E_T = E\sin(\theta)$ and $p_T = p\sin(\theta)$ respectively. Underlying QCD events tend to have momenta along the direction of the beamline, while production of more massive final states tends to be more spherical. For this reason, it is useful to define a variable called pseudorapidity: $\eta = -\ln[\tan(\theta/2)]$. QCD events are produced with approximately equal occupancy in η, while massive states are produced at lower η, making it advantageous to instrument the central region of the detector.

5.2.1 Silicon Tracking

Closest to the beamline was a layered silicon microstrip detector. When a charged particle passes through silicon, it ionizes the silicon, creating electron-ion(hole) pairs. With the application of a voltage, these pairs will drift apart and can be collected by readout strips at the edge of the silicon. The position of the incident particle can be determined from the amount of charge collected by each strip, and the position resolution depends on the distance between strips (pitch). In the CDF detector, an $r-\phi$ pitch of $\sim 60\mu$m, and an $r-z$ pitch of up to 141μm gives an impact parameter resolution of 40μm and a z_0 resolution of 70μm. Within the silicon acceptance, the efficiency for attaching three or more hits from the inner silicon detectors to a COT track is approximately 92%. The purpose of this detector

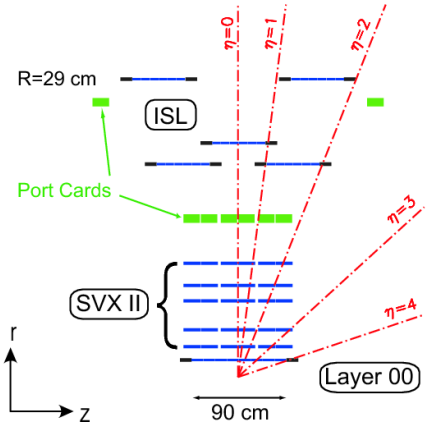

Figure 5.3 An $r-z$ view of the CDF silicon detector [52].

was three-dimensional precision tracking, particularly important for the identification of b-quarks, which are identified by a vertex displaced from the primary event. A readout time of ten microseconds allowed silicon detector information to be used for higher-level triggering. The silicon detector was made up of layers of silicon microstrips arranged in three barrels. The innermost layer, immediately outside the beampipe at a radius of 1.6 cm, was Layer 00 (L00), intended to preserve efficiency even after high doses of radiation. Outside of this were five Silicon Vertex (SVX) layers, extending from a radius of 2.1 to 17.3 cm and making up the majority of the detector with coverage out to $|\eta| \leq 2.0$. The outermost region, the Intermediate Silicon Layer, occupied the radius from 20 to 28 cm. This component consisted of one layer in the central region ($|\eta| \leq 1.0$) and two in the forward region ($1.0 < |\eta| \leq 2.0$) to enhance linking of silicon tracks to the Central Outer Tracker and tracking in the forward region respectively. Each layer of the detector had silicon microstrips arranged axially on the inner side, measuring $r-\phi$. On the outer side, layers 0, 1, and 3 had strips at a 90°angle measuring $r-z$, while layers 2, 4 and the ISL had strips at a 1.2°angle for stereo information. Layer 00 was single sided. An $r-z$ view of the silicon detector is shown in Figure 5.3.

5.2.2 Central Outer Tracker

Outside of the silicon detector was the Central Outer Tracker (COT), an open cell drift chamber. A drift chamber is filled with gas that ionizes when a charged particle travels through the chamber. The electrons and ions travel towards sense and field wires, which detect ionized electrons and create the potential difference in the cell. The position of the incident particle can be inferred from the timing and location of the charge depostion, and the drift velocity of electrons in the gas. Sense wires in the COT were separated by 7.62 mm and the maximum drift time was 100 ns, preventing pileup from multiple bunch crossings. Hits are read out and tracks reconstructed in the COT in time for the level one trigger, discussed below. The COT provided general purpose tracking, measuring position and momentum of charged particles with a position resolution of 140 μm and a momentum resolution of $0.0015/p_T^2(\mathrm{GeV/c})^-1$, and triggering on high p_T charged leptons from W bosons. The COT occupied a radius of 40 to 137 cm and had an active region in z of 310 cm. It was composed of 8 superlayers of cells covering a range of $|\eta| \leq 1.0$. Each cell had a wire plane containing 12 sense wires and 13 field wires, with two additional field shaping wires at either end. In the second, fourth, sixth, and eighth layers, the wires are aligned axially along the beamline, while the other layers are offset by 2°to measure stereo. The cells were filled with a 50/50 argon-ethane gas mixture. The tracking efficiency of the COT was measured in W candidate events to be 98.6% for tracks that cross all 96 layers of the COT, with limited tracking possible out to $|\eta| \leq 1.8$. An $x - y$ view of a COT cell is shown in Figure 5.4.

5.2.3 Solenoid

The COT and silicon detectors measure position. In the presence of a magnetic field of strength B, a charged particle of mass m, charge q, and velocity v curves with a radius of

$$r = \frac{mv}{qB} \tag{5.1}$$

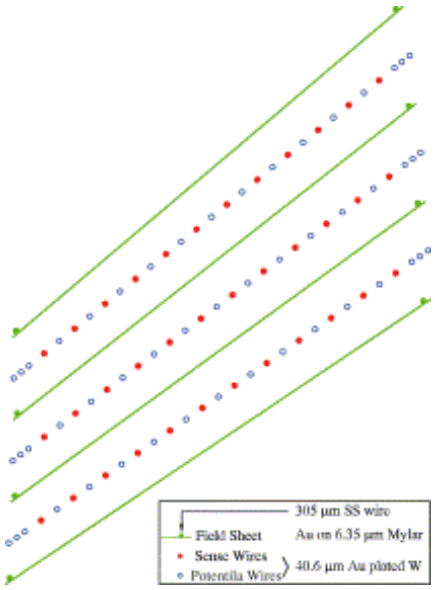

Figure 5.4 An $x - y$ view of the CDF COT [53].

The solenoid has a radius of 1.5m and is 4.8m in length, situated between the Time of Flight detector and calorimeters (discussed below). It creates a uniform magnetic field of 1.4T, allowing the sign of charge and momentum to be determined from the curvature of tracks in the silicon and COT detectors. The resolution of the curvature, and thus momentum measurement depends on the amount of curvature, degrading at higher momenta, but improving with magnetic field strength.

5.2.4 Calorimeters

Outside of the solenoid was the Electromagnetic Calorimeter (ECAL). This detector measured the energy of electromagnetic showers, achieving an energy resolution of $13.5\%/\sqrt{E_T} \bigoplus 2\%$ in the central region (CEM, $|\eta| < 1.1$) and $16\%/\sqrt{E_T} \bigoplus 1\%$ in the forward region (PEM, $1.1 < |\eta| \leq 3.64$). The ECAL was a sampling calorimeter composed of alternating layers of lead and scintillator, read out by PMTs. Traveling from the beamline, a particle encountered 0.93 radiation lengths of material, where each radiation length is 7/9 of the mean free path for pair production by a high energy photon. Distinguishing pair-produced electrons from those originating from W boson decays is important for the analyses discussed here. The first layer of the ECAL was read out separately to obtain pre-shower information, improving particle discrimination. Wire strips known as ShowerMax detectors (CES/PES) were embedded in the ECAL approximately six radiation lengths deep at the expended maximum of electromagnetic showers. Their purpose was position measurements for linking showers to tracks and determining shower shape to further improve particle identification. The ECAL itself had $19 - 21$ radiation lengths of material, depending on η, sufficient to contain high-energy electrons. An electron trigger running at the beam crossing rate was formed by matching calorimeter information to COT tracks. Muons, as minimum ionizing particles, can be identified from their minimal energy deposits in the calorimeter. Beyond the ECAL was the Hadronic Calorimeter (HCAL), a sampling calorimeter which used steel as an absorber instead of lead. This calorimeter measured the energy of hadronic showers with an energy resolution of $75\%/\sqrt{E_T} \bigoplus 3\%$ in the central region (CHA, $|\eta| < 1.3$) and $74\%/\sqrt{E_T} \bigoplus 4\%$ in

the forward region (PHA, $1.1 < |\eta| \leq 3.64$). The ratio of energy deposition in the hadronic and electromagnetic calorimeters is used in identifying leptons, which deposit little or no energy in the HCAL. The calorimeters are also used to detect the presence of missing transverse energy, the experimental signature of a neutrino, by looking for an imbalance in the vector sum of energy deposited in calorimeter towers.

5.2.5 Muon System

The outermost component of the CDF detector was the muon system, composed of a number of different drift chambers and scintillators. Multiple layers of drift chambers found track stubs of muons, and scintillators provided timing information used to reject non-collision beam related and cosmic background. Muon detectors were placed outside of as much material as possible; muons deposit relatively little of their energy in material, so any charged particle that made it through the rest of the detector was most likely a muon. Innermost and central was the Central Muon Detector (CMU), four layers of drift chambers organized by ϕ wedges in a barrel on the outside of the central calorimeter behind 5.5 pion interaction lengths of material. The CMU was capable of detecting muons of $p_T > 1.4$ GeV covering $|\eta| < 0.6$. An upgrade, the Central Muon Upgrade (CMP), was added with additional layers outside the magnet return yoke, with a total of 7.8 pion interaction lengths. This detector was capable of detecting muons of $p_T > 2.2$ GeV in the same range. The CMP used the magnet return yoke from as absorber, requiring a box geometry. ϕ gaps in the CMU were covered by the CMP, while η gaps in the CMP were covered by the CMU. Muon coverage was extended from $0.6 < |\eta| \leq 1.0$ by the Central Muon Extension (CMX) for $p_T > 1.4$ GeV and from $1.0 < \eta \leq 1.5$ by the Barrel Muon Detector (BMU) for $p_T > 1.4 - 2.0$ GeV, depending on η. Material before these detector ranged from 6.2 pion interaction lengths in the CMX to 20, increasing with $|\eta|$. Gaps in the ϕ coverage of the CMX were filled in by the CMX Miniskirt and Keystone, giving nearly complete coverage in ϕ. The barrels of the BMU were built around the Run I toroids; the bottom 90°of ϕ were not covered due to the support structures for the toroids. Another component of the muon detection system was

scintillator tiles on the outside of the wire chambers. These scintillators had a readout time of three nanoseconds, providing timing and triggering information about muons. The track stubs found in the CMU/P/X could be linked to tracks in the COT to form a muon trigger that runs at the beam crossing rate. However the gaps in muon coverage make alternative methods of identification advantageous, such as minimum ionizing energy deposits matched to tracks.

5.2.6 Cherenkov Luminosity Counters

The detector systems described above left a 3°opening around the beamline ($3.7 < |\eta| < 4.7$). In this opening were the Cherenkov Luminosity Counters (CLC). These detectors measured the number of inelastic $p\bar{p}$ scatterings in each bunch crossing. Primary particles from these interactions entering the isobutane radiator generated ~ 100 photoelectrons that were collected by PMTs. Using simulation and tests, the average number of $p\bar{p}$ collisions could then be determined. Monte Carlo predicts the number of proton-antiproton interactions corresponding to the number of particles observed. At luminosities up to $3.6^{32}\text{cm}^{-2}s^{-1}$, the most reliable determination is by the method of zero interactions. The average number of interactions is calculated from the fraction of zero-interaction crossings according to Poisson probability: $P_0(\mu) = e^{-\mu}$. The luminosity is measured to an accuracy of 5.9%. The dominant uncertainties on the measurement come from the operation and acceptance of the CLC (4.4%) and the theoretical uncertainty in the inelastic $p\bar{p}$ cross section (4.0%).

5.2.7 Time of Flight Detector

Just outside the COT was the Time-of-Flight detector (TOF), composed of plastic scintillator read out by fine-mesh Photo-Multiplier Tubes (PMTs). This dector improved particle discrimination, particularly of K and π mesons, providing TOF information with a resolution of approximately 100 ps in the region $|\eta| < 1$. It is not used in the analyses discussed here.

5.2.8 Triggering

Collisions ocurred at a rate of $\sim 3MHz$, while the speed for writing events to tape was $150Hz$. Three levels of trigger were applied, reducing the rate successively. Level 1 (L1) was a hardware trigger, reducing the event rate to roughly $10kHz$. A key component of the L1 trigger was the eXtremely Fast Tracker (XFT), which identified high-momentum tracks in the COT. Track segments are found in the axial layers of the COT by comparing cell numbers and hit types to known patterns for tracks with $p_T > 1.5$ GeV. The highest p_T track matching hits in all four layers could be directly triggered on, or used in conjunction with other input streams. The L1CAL stream found calorimeter based objects, including electrons and missing transverse energy. Two calorimeter trigger paths existed. In the first, thresholds were applied to individual tower energies and the number of towers passing each threshold was counted. Single towers could be matched to coincident tracks in order to form an electron trigger. In the second path, the total energy in all towers was summed with weighting by θ to determine the $\not\!\!E_T$ and compare to a threshold. In the L1 MUON stream, muon primitives were identified in the muon scintillators or wire chambers matched to an extrapolated high p_T track. Level 2 (L2) used specialized hardware to perform limited event reconstruction, reducing the rate to roughly $1kHz$. At this stage silicon tracking information was also available. The third stage of triggering, Level 3 (L3), took full advantage of detector information, fully reconstructing events in a processor farm. At this stage particles could be reconstructed, and events could be selected to write to tape. Typical criteria for event selection would be an energetic particle or a large amount of missing transverse energy, possibly indicating that a massive state had been produced in the event. The total running time of the trigger was roughly a second, during which event information was stored in a buffer area.

In our analysis we use data collected from six triggers based on leptons and missing Et, shown in Table 5.1.

MUON_CMUP18
MUON_CMP18_PHI_GAP
MUON_CMU18_ETA_GAP
MUON_CMX18
ELECTRON_CENTRAL_18
MET_PEM

Table 5.1 Triggers used in this analysis

The first four triggers all look for high p_T muons. At L1, a single muon candidate with $p_T > 12$ GeV is required, loosely matching a COT track, a requirement tightened at L2. The L3 trigger selection requires $p_T > 20$ GeV and E_T deposition consistent with a muon. ELECTRON_CENTRAL_18 triggers on a single high-p_T electron. The L1 requirement is a track with $p_T > 8$ GeV matched to an ECAL tower with $E_T > 8$ GeV. At L2, the E_T threshold is raised to 16 GeV, and the ratio of energy deposition in HCAL/ECAL is required to be less than 0.125. At L3, the requirements are further raised to $E_T > 18$ GeV, $p_T > 9$ GeV. The final trigger, MET_PEM, is seeded at L1 by the requirement of an ECAL tower with $E_T > 8$ GeV, and $\not\!\!E_T > 15$ GeV. At L2 the E_T threshold is raised to 20 GeV, and at L3 the E_T and $\not\!\!E_T$ are recalculated and verified.

5.2.9 Detection of Electrons

Electrons interact with a number of detector elements. Electron tracks can be identified in the COT or the complete tracking system including silicon detectors. In the ECAL they shower, producing photons via bremsstrahlung which then produce electron-positron pairs, the process continuing until the particles drop below the necessary energy thresholds. Ultimately the electrons deposit almost all of their energy in the ECAL via ionization. While the direction of the electron is determined from tracking, the magnitude is taken to be equivalent to the ECAL energy. If the electron radiates photons in flight, they will tend to be colinear with the electron, and thus impact on the same calorimeter tower,

giving a more accurate measurement of the electron's original E_T/p_T. The ShowerMax detectors measure the position and profile of the electron shower at the expected shower maximum, and this information is used to match the calorimeter and tracking information. Electron candidates are required to be isolated, with minimal energy deposition in the HCAL. These requirements reduce backgrounds from charged hadrons and semileptonic decays, while photons are distinguished by shower shape. Other backgrounds to electrons include photons that convert in the material before the ECAL, and neutral pions matched to an isolated track. The efficiency for identifying electrons is approximately 90%. Fake rates range from 0.2% to 6%, and depend on E_T and central or plug detector.

5.2.10 Detection of Muons

At collider energies muons primarily lose energy through ionization. However, as minimum ionizing particles muons deposit little energy in any material. For this reason both momentum direction and magnitude are determined from the tracking system. The COT tracks effectively out to $|\eta| < 1.5$, after which the silicon detector improves track finding efficiency. As minimum ionizing particles, muons are capable of traversing the entire detector and leaving a track in the muon systems, referred to as a muon stub. A muon is identified by matching a stub to an isolated track, with little or no energy deposited in the calorimeters. Backgrounds to muons include hadrons either punching through the absorbers or decaying to muons in flight. Muon identification efficiencies range from $74-90\%$, depending on which element(s) of the muon detector the muon is fiducial to. Muons identified from calorimeter information only have an efficiency of $32-60\%$. Fake rates range from 0.5% to 6%, and again depend on the relevant calorimeter and muon detector elements, and the p_T of the muon candidate.

5.2.11 Detection of Tracks

The coverage of the calorimeter and muons systems is limited, with cracks to accomodate electronics and cooling for inner detectors. Events with isolated tracks that are not fiducial

to the calorimeter or to stubs in the muon system are enriched in charged leptons from W decay. Electrons that travel through the uninstrumented region of the calorimeter may radiate photons into adjacent towers, thus failing isolation. These events can be recovered by subtracting adjacent towers in the isolation requirement. The track efficiency is approximately 35% for electrons and 55% for muons. The fake rate is approximately 4%, 20% for the modified isolation requirement.

5.2.12 Detection of Jets

As discussed in Section 2.1, strongly interacting particles producing a cone of hadrons, referred to as hadronization. These particles deposit energy in the HCAL, and those that are charged deposit energy in the ECAL as well. A special case is jets originating from a b-quark. The b-quark travels roughly a millimeter from the interaction point before decaying. silicon tracking information allows the secondary vertex, and thus the b-jet to be identified.

5.2.13 Detection of Missing Energy

Leptonic W boson decays produce neutrinos, which escape the detector without detection. Their presence must be inferred from the rest of the event. We know that particle interactions conserve energy. However, we are limited by the coverage of the CDF detector. Missing energy along the beamline cannot be detected. For this reason we are confined to missing energy transverse to the beamline, the $\not\!\!E_T$. Because other known particles deposit energy in the calorimeter, a large $\not\!\!E_T$ indicates the presence of a neutrino. There are two exceptions which need to be corrected for: muons, which deposit relatively little energy in the detector, and jets, whose energy is subject to corrections. The details of these corrections are discussed in Section 7.5

Chapter 6

Event Simulation

6.1 Monte Carlo Simulation

We model a number of physical processes with Monte Carlo simulation, in which a random number generator is used to draw representative events from an underlying predicted distribution. Monte Carlo generation takes place in a number of steps. Initially, quark and gluon momenta are sampled from parton distribution functions (PDFs), and a hard event is generated, for example pair production of top quarks: $q\bar{q} \rightarrow t\bar{t}$. For our purposes, this will be generated at Leading Order (LO) or Next-to-Leading Order (NLO), referring to which Feynman diagrams are considered in the prediction. Particles in the hard event are then allowed to evolve: radiating, decaying, and hadronizing as appropriate. Finally, in order to compare theoretical prediction to data the detector response to the event must be simulated. After this step, simulation and data can be treated in the same manner.

6.2 Parton Distribution Functions

While the physics of interest is produced by the interaction of two partons, they are initially bound in a proton and anti-proton. Because perturbative QCD cannot be applied at low energies the momentum distributions of the consituent particles cannot be directly calculated, being instead determined by a phenomenological method. Functional forms are fit to the data produced by deep inelastic scattering experiments that probe the structure of the proton, and extrapolated to higher energies [55] and supplemented by high energy hadron collision data including W, Z, and jet cross sections. The result is a set of probabilities for

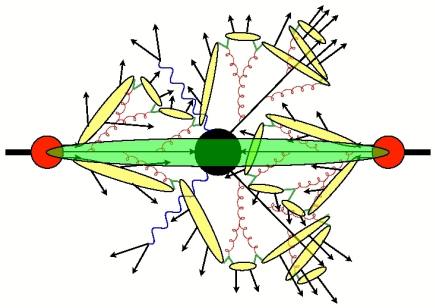

Figure 6.1 An example of the hadronization process. [54]

each type of parton to be carrying a fraction x of the momentum of the proton. PDFs must be matched to the order of the generator. MC@NLO requires NLO PDFs to avoid generating effects already simulated by the hard event generator.

6.3 Hard Scattering

Generators such as Pythia or Alpgen draw initial partons from the PDF distributions. The matrix element of the hard process of interest (e.g. $q\bar{q} \rightarrow t\bar{t}$) is calculated to the required order. This would be leading order for Pythia, or leading order with N jets for Alpgen. NLO generators such as MC@NLO include diagrams of higher order in QCD, including loop diagrams and parton radiation. The four-momenta of the outgoing particles are drawn from probability distributions. Decays of these particles are handled separately in parton showering.

6.4 Showering

As has been previously discussed, partons are not directly observed in the final state. Instead these particles form bound states referred to as hadrons. Once again, perturbative QCD cannot be applied and a phenomenological model must be considered. We generally perform parton showering with Pythia, which uses the Lund string model [56]. QCD field lines connecting $q\bar{q}$ pairs are compressed into strings by the gluon self-interaction. When

an energy threshold is reached, the string fragments to produce new $q\bar{q}$ pairs. This process repeats until the energy of the quarks in low enough to form bound states, referred to as hadronization. MC@NLO interfaces to HERWIG [57] to perform parton showering. In HERWIG, parton showers are generated by a coherent branching algorithm, in which the parton shower is evolved in terms of the parton energy fraction and an angular variable, constrained by interference to be smaller than for the previous branching. When the variable reaches a cutoff, showering stops and the 4-momenta of the shower constituents are determined. Both methods of parton showering have been tuned to reporduce the recoil of non-perturbative hadronic activity against the hard scattering interaction. As a result, the magnitude of the momentum of an additional jet is modeled accurately. However, kinematics relative to jets in the hard interaction, such as the opening angle between jets, may not be well described.

6.5 Fixed and Next-to-Leading Order

In this thesis we are interested in events with multiple jets in the hard event, which are not present for example in WW production at leading order. One option is to calculate all aspects of the interaction consistently at Next-to-Leading Order (NLO) with a generator such as MC@NLO [11]. At NLO, events will be generated with zero and one partons in the hard event. Note that the number of partons in the hard event is not necessarily the same as the number of jets in the final state. In the parton showering step, partons may be radiated with sufficient energy to form detectable jets. Final state hadrons from a single initial parton may be sufficiently separated to form two jets. Conversely, two jets may overlap and be merged, or jets could be lost to detector effects. Thus it is possible to generate a sample of WW events with two or more jets with NLO Monte Carlo. Another approach to event generation is fixed order, where discrete samples are generated at the lowest order that produces the corresponding final state. One sample is generated for the underlying process, for example WW, and another for WW with one additional jet, two additional jets and so on, to a specified number (in our case, three). These samples are combined in order to give a complete prediction for the process. Note the fixed order simulation is also interfaced with a

parton shower simulation to simulate the non-perturbative behaviour of partons that produce jets below the hard jet threshold and addditional jets beyond the maximum jet multiplicity sample. The parton shower generator may radiate jets greater than hard jet threshold which would lead to double counting of event topologies with additional jets but these events are simply eliminated by vetoing radiated jets above the hard jet threshold in all but the highest multiplicity sample using the MLM [58] technique. This is the approach of the Alpgen [13] generator. Both of these methods are capable of generating events with two W bosons and multiple jets. The kinematics of a hard jet in an NLO calculation should be better simulated than those in an equivalent LO calculation of a diagram that explicitly includes the jet in the final state, as NLO effects on the differential cross section are considered. However, additional jets beyond those produced at NLO must then come from parton showering, for which kinematics, particularly relative to the initial jet, are not necessarily well simulated. In fixed order events, additional jets are better simulated, since they are directly produced in the hard scattering and not reliant on the parton shower. In the $H \rightarrow WW + 2$ or more jets search, Alpgen is chosen because of the importance of the relative kinematics, discussed in Section 10.2.4. However, both techniques have advantages and a choice must be made for a given situation based on physics considerations and/or direct comparison to data. We compare the WW differential cross section measurement to predictions from both methods in order to inform such choices elsewhere.

6.6 Detector Response

The response of the detector to the event is described with CDFSim. A detailed model of the CDF detector is created, and the GEANT [59] toolkit is used to describe the interaction of the particles of the showered event with the material of the detector. This includes the loss of energy through ionization, the decay of long-lived particles, and processes such as photon conversion in the material of the solenoid. The response of the detector is also simulated, giving a description of the signals we would expect to see from the generated event. The

behavior of readout and processing electronics is also modeled, resulting in a simulated signal in the same format as that of data.

6.7 Monte Carlo Scale Factors

Detector and reconstruction effiencies are not perfectly modeled by CDFSim. However these efficiencies can be measured in data, as discussed in Secion 7.6. Differences in efficiencies between data and Monte Carlo are accounted for by corrections applied to the Monte Carlo samples separately for each of the lepton pair categories. The formula for scaling is as follows:

$$\frac{\sigma \times \beta \times \epsilon_{filter} \times \epsilon_i^{trg} \times s_i^{lep} \times \epsilon_{vtx} \times \mathcal{L}_i}{N_i^{gen}(|Z_0| < 60\text{cm})} \tag{6.1}$$

Where:

- σ is the cross-section for the Monte Carlo process (as listed in Table 6.2)
- β is the branching fraction for the Monte Carlo process (as listed in Table 6.2)
- ϵ_{filter} is the filter efficiency applied for any filter used in the generation process (as listed in Table 6.2)
- ϵ_i^{trg} is the effective trigger efficiency for the category (see below)
- s_i^{lep} is the effective lepton id scale factor (see below)
- ϵ_{vtz} is the run dependent efficiency of the z-vertex position requirement ($|z_0| < 60$ cm)
- $\mathcal{L}_i$ is the luminosity of the dataset in the good run list in which the lepton category falls (see Table 6.1)

Jets are treated by a similar technique to account for detector effects that also accounts for the additional complexity that measured jets based on calorimeter energy deposits cannot be simply identified one to one with jets of hadrons produced by the simulation, as described in Section 10.5.3.

Good run list	$\mathcal{L}(pb^{-1})$
EM_NOSI	9735.1
EM_CMUP_NOSI	9695.9
EM_MU_NOSI_CMXIGNORED	9653.3
EM_SI	9446.5
EM_CMUP_SI	9409.2
EM_MU_SI_CMXIGNORED	9370.4

Table 6.1 Luminosity for each of the good run lists used in this analysis, including the trigger prescale correction of 1.019.

6.8 Monte Carlo Samples

6.8.1 Background Samples

All samples are CDF centrally generated. WZ, ZZ, and $t\bar{t}$ samples are generated with PYTHIA [12] at leading order, as is zero and one-jet Drell-Yan. With the exception of MC@NLO, all Monte Carlo samples are interfaced to Pythia for parton showering. $W\gamma$ is generated with Baur MC [60] at next-to-leading order. Drell-Yan events with two or more jets are simulated with Alpgen [13] at fixed order. In several cases the Monte Caro must be tuned to address limitations or discrepancies. Simulated cross sections are normalized to theoretical predictions at NLO for WZ and ZZ [61]. In the Higgs search the $t\bar{t}$ cross section is normalized to the NLO prediction [62], while in the WW search it is normalized to a measurement in the dilepton channel [63]. Modeling of the $W\gamma$ background is tested using a control region requiring two leptons of the same charge and $m_{ll} < 16$ GeV. Based on this control region, a scale factor of 0.71 on the overall normalization of the $W\gamma$ sample is obtained to account for mismodeling of photon conversion and detection as a single electron. Modeling of Drell-Yan contributions is particularly difficult, as the $\not\!\!E_T$ requirement means that only events with a mismeasured object pass selection. The zero and one jet base samples are validated in a control region requiring intermediate $\not\!\!E_{T,spec}$ and an ee or $\mu\mu$ pair with $80 < m_{ll} < 99$ GeV. To better model data in this control region, the $\not\!\!E_T$ is shifted down by 4 GeV. In the two or more jet base region, Drell-Yan contributions from NNLO are significant and Alpgen-generated events are used for modeling the background. No need for a $\not\!\!E_T$ shift is observed in this region. Additional information about the generated samples is shown in Table 6.2. Events in which a jet is incorrectly reconstructed as a lepton (W+jets) are not simulated, instead being modeled by the method described in Section 7.7.

6.8.2 WW Samples

The WW signal is modeled with Alpgen [13]. Modeling of WW is checked with MC@NLO [11] interfaced to HERWIG [57] for parton showering and found to be consistent. Both Alpgen

Process	Stntuple	$\sigma \times \beta$ (pb)	K-factor	Filter Eff
$W\gamma \to e\nu\gamma$	re0s6d, re0s6e, re0s6h, re0s6i	32.38×0.5	1.36	1.0
$W\gamma \to \mu\nu\gamma$	re0s6f, re0s6g, re0s6j, re0s6k	32.38×0.5	1.36	1.0
$W\gamma \to \tau\nu\gamma$	re0s6a	13.6	1.36	1.0
WW Alpgen	wt0swa, wt0swb, wt0swc, wt0swd, wt0sw2, wt0sw3, wt0sw6, wt0sw7	11.27×0.105	1.0	1.0
WZ	we0s6d, we0scd, we0shd, we0sld, we0sod, we0sbf, we0shf	3.47×0.101	1.0	0.754
ZZ	we0s7d, we0sdd, we0sid, we0smd, we0spd, we0scf, we0sif	1.446	1.0	0.233
$t\bar{t}$	tsrd73, tsri72, tsri73	7.04	1.0	0.480
$Z \to ee$ Pythia	ze1s6d, ze1sad, ze0scd, ze0sdd, ze0sed, ze0see, ze0seh, ze0sej, ze0sei, ze1sei	355	1.378	1.0
$Z \to \mu\mu$ Pythia	ze1s6m, ze1s9m, ze0scd, ze0sbm, ze0scm, ze0sdm, ze0sem, ze0sfm, ze0sgm, ze0sim	355	1.378	1.0
$Z \to \tau\tau$ Pythia	ze0s8t, ze0sbt, ze0sct	355	1.378	1.0
$Z \to \tau\tau$ Pythia	ze0sat	237	1.378	1.0

Table 6.2 Monte Carlo samples used in this analysis.

$Z \rightarrow ee$ Alpgen	zt0sp0, zt0sp1, zt0szb, zt0s3p, zt0s4p, bt0sz0, bt0sz1, bt0sz2, bt0sz3, bt0sz4, xt0s0p, xt0s1p, xt0s2p, xt0s3p, xt0s4p, zt0so6, zt0so7, zt0so9, zt0soa, zt0sob, yt0s0p, yt0s1p, yt0s2p, yt0s3p, zt0sol, zt0som, zt0son, zt0soo, zt0sop	359	1.345	1.0
$Z \rightarrow ee$ Alpgen	zt0sp5, zt0sp6, zt0szt, zt0s8p, zt0s9p, bt0sz5, bt0sz6, bt0sz7, bt0sz8, bt0sz9, xt0s5p, xt0s6p, xt0s7p, xt0s8p, xt0s9p, zt0soc, zt0sod, zt0sof, zt0sog, zt0soh, yt0s5p, yt0s6p, yt0s7p, yt0s8p, zt0soq, zt0sor, zt0sos, zt0sot, zt0sou	359	1.345	1.0
$Z \rightarrow \tau\tau$ Alpgen	zt0st3, zt0st4, zt0st2, bt0sza, bt0szb, bt0szc, xt0st0, xt0st1, xt0st2, zt0soi, zt0soj, zt0sok, zt0s0h, zt0s1h, zt0s2h, zt0s3h, zt0s4h, zt0sox, zt0soy	359	1.345	1.0

Table 6.3 Monte Carlo samples used in this analysis continued.

and MC@NLO are used to generate theoretical predictions for the cross section as a function of jet multiplicity and transverse energy for comparison to measurements of these cross sections in data. In the Higgs search, the WW cross section is normalized to a theoretical prediction at NLO [44]. The WW samples do not include contributions from gluon fusion, which while only present in diagrams at NNLO or above, contributes potentially signal-like events. Events are reweighted as a function of $\Delta\phi_{ll}$ to incorporate the extra predicted contribution [64]. Additional information about the generated samples is shown in Table 6.2.

6.8.3 HWW Samples

The Higgs samples are generated with Pythia and scaled according to higher order predictions. Gluon fusion is normalized to an NNLL prediction [19], associative production to an NNLO prediction [26], and vector boson fusion to an NLO prediction [23]. In the case of gluon fusion, the p_T distribution given by Pythia is reweighted to match the distribution calculated at NNLL+NLO accuracy by HqT [65] [66] at each mass point. Additional information about the Monte Carlo samples is shown in Tables 6.4- 6.7. The partial widths for all decay processes are computed with HDECAY [67] with the exception of four fermion final states, for which the partial widths are computed with PROPHECY4F [68] [69]. Branching ratios are computed from the relative fractions of the total partial widths.

$M_H(GeV^2)$	Period	Stntuple	σ (pb)	BR ($H \rightarrow WW$)	BR($WW \rightarrow \ell\nu\ell\nu$)
110	0-27	dhgs4a,dhgs6a	1.413	0.0459	0.1027
115	0-27	dhgs4l,dhgs6l	1.240	0.0827	0.1027
120	0-27	dhgs4b,dhgs6b	1.093	0.1364	0.1027
125	0-27	dhgs4m,dhgs6m	0.967	0.2078	0.1027
130	0-27	dhgs4c,dhgs6c	0.858	0.2943	0.1027
135	0-27	dhgs4n,dhgs6n	0.764	0.3910	0.1027
140	0-27	dhgs4d,dhgs6d	0.682	0.4916	0.1027
145	0-27	dhgs4o,dhgs6o	0.611	0.5915	0.1027
150	0-27	dhgs4e,dhgs6e	0.548	0.6891	0.1027
155	0-27	dhgs4p,dhgs6p	0.492	0.7892	0.1027
160	0-27	dhgs4f,dhgs6f	0.439	0.9048	0.1027
165	0-27	dhgs4q,dhgs6q	0.389	0.9591	0.1027
170	0-27	dhgs4g,dhgs6g	0.349	0.9639	0.1027
175	0-27	dhgs4r,dhgs6r	0.314	0.9581	0.1027
180	0-27	dhgs4h,dhgs6h	0.283	0.9325	0.1027
185	0-27	dhgs4s,dhgs6s	0.255	0.8450	0.1027
190	0-27	dhgs4i,dhgs6i	0.231	0.7870	0.1027
195	0-27	dhgs4t,dhgs6t	0.210	0.7588	0.1027
200	0-27	dhgs4j,dhgs6j	0.192	0.7426	0.1027

Table 6.4 Higgs production via gluon fusion.

$M_H(GeV^2)$	Period	Stntuple	σ (pb)	BR ($H \to WW$)	BR($WW \to \ell\nu\ell\nu$)
110	0-27	vhgs1a,vhgs3a,vhgs6a	0.0871	0.0459	0.1027
115	0-27	vhgs2l,vhgs3l,vhgs6l	0.0791	0.0827	0.1027
120	0-27	vhgs1b,vhgs3b,vhgs6b	0.0717	0.1364	0.1027
125	0-27	vhgs2m,vhgs3m,vhgs6m	0.0674	0.2078	0.1027
130	0-27	vhgs1c,vhgs3c,vhgs6c	0.0625	0.2943	0.1027
135	0-27	vhgs2n,vhgs3n,vhgs6n	0.0577	0.3910	0.1027
140	0-27	vhgs1d,vhgs3d,vhgs6d	0.0526	0.4916	0.1027
145	0-27	vhgs2o,vhgs3o,vhgs6o	0.0492	0.5915	0.1027
150	0-27	vhgs1e,vhgs3e,vhgs6e	0.0457	0.6891	0.1027
155	0-27	vhgs2p,vhgs3p,vhgs6p	0.0422	0.7892	0.1027
160	0-27	vhgs1f,vhgs3f,vhgs6f	0.0386	0.9048	0.1027
165	0-27	vhgs2q,vhgs3q,vhgs6q	0.0361	0.9591	0.1027
170	0-27	vhgs1g,vhgs3g,vhgs6g	0.0336	0.9639	0.1027
175	0-27	vhgs2r,vhgs3r,vhgs6r	0.0311	0.9581	0.1027
180	0-27	vhgs1h,vhgs3h,vhgs6h	0.0286	0.9325	0.1027
185	0-27	vhgs2s,vhgs3s,vhgs6s	0.0268	0.8450	0.1027
190	0-27	vhgs1i,vhgs3i,vhgs6i	0.0249	0.7870	0.1027
195	0-27	vhgs2t,vhgs3t,vhgs6t	0.0230	0.7588	0.1027
200	0-27	vhgs1j,vhgs3j,vhgs6j	0.0212	0.7426	0.1027

Table 6.5 Higgs production via vector boson fusion.

$M_H(GeV^2)$	Period	Stntuple	σ (pb)	BR ($H \rightarrow WW$)	Filter Efficiency
110	0-27	fhgs4a,fhgs6a	0.2092	0.0459	0.6880
115	0-27	fhgs4l,fhgs6l	0.1788	0.0827	0.6932
120	0-27	fhgs4b,fhgs6b	0.1529	0.1364	0.6978
125	0-27	fhgs4m,fhgs6m	0.1324	0.2078	0.7004
130	0-27	fhgs4c,fhgs6c	0.1147	0.2943	0.7032
135	0-27	fhgs4n,fhgs6n	0.0993	0.3910	0.7045
140	0-27	fhgs4d,fhgs6d	0.0860	0.4916	0.7065
145	0-27	fhgs4o,fhgs6o	0.0753	0.5915	0.7075
150	0-27	fhgs4e,fhgs6e	0.0660	0.6891	0.7085
155	0-27	fhgs4p,fhgs6p	0.0578	0.7892	0.7098
160	0-27	fhgs4f,fhgs6f	0.0507	0.9048	0.7108
165	0-27	fhgs4q,fhgs6q	0.0444	0.9591	0.7114
170	0-27	fhgs4g,fhgs6g	0.0389	0.9639	0.7125
175	0-27	fhgs4r,fhgs6r	0.0346	0.9581	0.7130
180	0-27	fhgs4h,fhgs6h	0.0307	0.9325	0.7141
185	0-27	fhgs4s,fhgs6s	0.0273	0.8450	0.7149
190	0-27	fhgs4i,fhgs6i	0.0243	0.7870	0.7151
195	0-27	fhgs4t,fhgs6t	0.0217	0.7588	0.7158
200	0-27	fhgs4j,fhgs6j	0.0193	0.7426	0.7165

Table 6.6 Associated Higgs production with a W boson.

$M_H(GeV^2)$	Period	Stntuple	σ (pb)	BR ($H \rightarrow WW$)	Filter Efficiency
110	0-27	uhgs4a,uhgs6a	0.1243	0.0459	0.6930
115	0-27	uhgs4l,uhgs6l	0.1074	0.0827	0.6994
120	0-27	uhgs4b,uhgs6b	0.0927	0.1364	0.7031
125	0-27	uhgs4m,uhgs6m	0.0811	0.2078	0.7061
130	0-27	uhgs4c,uhgs6c	0.0709	0.2943	0.7087
135	0-27	uhgs4n,uhgs6n	0.0620	0.3910	0.7106
140	0-27	uhgs4d,uhgs6d	0.0542	0.4916	0.7122
145	0-27	uhgs4o,uhgs6o	0.0480	0.5915	0.7135
150	0-27	uhgs4e,uhgs6e	0.0425	0.6891	0.7151
155	0-27	uhgs4p,uhgs6p	0.0376	0.7892	0.7155
160	0-27	uhgs4f,uhgs6f	0.0333	0.9048	0.7172
165	0-27	uhgs4q,uhgs6q	0.0295	0.9591	0.7183
170	0-27	uhgs4g,uhgs6g	0.0261	0.9639	0.7184
175	0-27	uhgs4r,uhgs6r	0.0233	0.9581	0.7196
180	0-27	uhgs4h,uhgs6h	0.0208	0.9325	0.7204
185	0-27	uhgs4s,uhgs6s	0.0186	0.8450	0.7212
190	0-27	uhgs4i,uhgs6i	0.0166	0.7870	0.7220
195	0-27	uhgs4t,uhgs6t	0.0150	0.7588	0.7229
200	0-27	uhgs4j,uhgs6j	0.0135	0.7426	0.7239

Table 6.7 Associated Higgs production with a Z boson.

Chapter 7

Event Reconstruction

The goal of event reconstruction is to unambiguously identify the signatures of fundamental SM particles and measure their 4-momenta. Each physics object is formed from available information in the relevant detector components. The result can be compared as directly as possible to simulations of fundamental interactions.

7.1 Electron Reconstruction

In order to maximize acceptance four categories of electrons are considered. The signature of an electron in the detector is energy deposited in the ECAL that is matched to an isolated track. Electrons from W decay are expected to be isolated, while hadrons misidentified as electrons, a major background, are from jets and are not. A distinction is made between electrons fiducial to the central and plug calorimeters, and electrons identified via a cut-based or likelihood-based method. In the cut-based method, the sums of transverse energy and momentum in a cone of $\Delta R = 0.4$ are required to each be less than 10% of the electron E_T. A number of quality requirements are applied. The electron is a charged particle and will leave ionization signatures in each layer of the tracking detector. These can be linked together to form a trajectory used to estimate transverse momentum magnitude from the curvature in the magnetic field and direction, and hits are requried in the axial and stereo layers of the COT (or hits in silicon for plug candidates). Energy in the ECAL and energy estimated by the tracker are required to be consistent, with the more accurate calorimeter measurement used to estimate the final electron momentum magnitude. Energy in the HCAL

	LBE
Region	Central
Fiducial	Track Fiducial to CES
Track P_T	> 10(5 if $E_T < 20$)
Track $\|z_0\|$	< 60 cm
Had/Em	$<= 0.125$
Iso/E_T	< 0.3
Likelihood	> 0.90

Table 7.1 Selection for LBE

should be low, as electrons should fully interact within the 19-21 radiation lengths of the ECAL, as opposed to charged hadrons that are not fully contained by the single hadronic interaction length. Position measurements in the strip detectors are required to match the extrapolated tracks. Shower shape data is also used to discriminate electrons from photons converting in the 0.93 radiation lengths before the ECAL. In the plug, where tracking is performed with silicon, reconstruction instead begins with a high energy tower in the ECAL. Two trajectories are extrapolated back to the silicon detector based on E_T corresponding to positive and negative charge. If consistent hits are found along either trajectory satisfying quality requirements in Table 7.4, an electron candidate is identified. Candidates which fail the cut-based selections are considered for likelihood-based categories. A cut is applied to the electron likelihood, calculated from similar quality and isolation variables. The complete selection for each electron category is given in Tables 7.1- 7.4.

7.2 Muon Reconstruction

Muons are divided into eight categories. Six of these correspond to different elements of the muon system. Generally the CMU and CMP overlap, but muons can be fiducial to both, or point to a crack in one. Other elements are the CMX, the CMX miniskirt and keystone regions, and the BMU. The distinction is made in order to associate categories with trigger

	PLBE
Region	Plug
Pes2DEta	$1.2 < \|\eta\| < 2.8$
Had/EM	< 0.05
Iso/E_T	< 0.3
Track Match	True
NSiHits	$>= 3$
Track $\|z_0\|$	< 60 cm
Likelihood	> 0.90

Table 7.2 Selection for PLBE

	TCE
Region	Central
Fiducial	Track Fiducial to CES
Track p_T	$>= 10$(5 if $E_T < 20$)
Track $\|z_0\|$	$<= 60$ cm
# Ax SL (5hits)	$>= 3$
#St SL (5hits)	$>= 2$
Conversion	$! = 1$
Had/Em	$<= 0.055 + 0.00045E$
Iso/E_T	$<= 0.1$
Lshr	$<= 0.2$
E/P	$< 2.5 + 0.015E_T$
Signed CES ΔX	$-3 <= q\Delta X <= 1.5$ cm
CES$\|\Delta Z\|$	< 3cm
tracks	BcTrk (Larry's Correction if Data)

Table 7.3 Selection for TCE

	PHX
Region	Plug
Pes2DEta	$1.2 < \|\eta\| < 2$
Had/EM	<= 0.5
PEM3x3FitTower	true
PEM3x3χ^2	<= 10
Pes5x9U	>= 0.65
Pes5x9V	>= 0.65
Iso/E_T	<= 0.1
ΔR(Pes,PEM)	<= 3.0
Track Match	true
NSiHits	>= 3
Track $\|Z_0\|$	<= 60cm

Table 7.4 Selection for phoenix electrons (PHX)

requirements and apply appropriate selection criteria. Isolation and track requirements are applied as for electrons, and energy deposits are required to be consistent with a minimum ionizing particle. Stubs in the muon system must be associated to an extrapolated track trajectory, within tolerances for expected scattering and resolution of the muon detectors. The last two categories correspond to candidates that pass similar quality and isolation requirements, but are not fiducial to any part of the muon system, being identified only with tracker and calorimeter information. As with electrons, tracks must pass quality requirements on the number of hits found in the tracking system, and are required to be isolated and consistent with originating at the primary vertex. As minimum ionizing particles, muons are required to have small associated energy deposits from the calorimeter system, and so the tracking system momentum is used to determine the momentum of the muon. Complete muon selection is described in Tables 7.5- 7.9.

7.3 Track Lepton Reconsctruction

A final two categories of leptons are not fiducial to the calorimeter or muon detectors. Isolation and quality requirements are applied to tracking information. It is possible for electrons to fail the isolation requirement by passing through a nonactive region of the calorimeter, radiating photons that deposite energy in adjacent towers. These candidates are recovered by a second category that subtracts energy deposits from ECAL towers adjacent to the track. Note that in these categories, muons and electrons cannot be distinguished, and so isolated tracks are treated as being either in reconstructing the event. The complete selection is described in Table 7.10.

7.4 Jet Reconstruction

We use jets in the calculation of $\not\!\!E_T$ and determination of jet multiplicity. Jets are identified from calorimeter information; being composed of hadrons they are expected to completely interact within the calorimeter system. In both cases we use JetClu jets with a cone size of $\Delta R < 0.4$. This algorithm finds seed towers with $E_T > 1$ GeV, and creates

	CMUP/CMU/CMP
E_{em}	$<= 2 + max(0, (p - 100)0.0115)$
E_{had}	$<= 6 + max(0, (p - 100)0.028)$
Iso/Pt	$<= 0.1$
NAxl(5 hits)	$>= 3$
NStL(5 hits)	$>= 2$
Track $\|Z_0\|$	$<= 60$ cm
Track $\|D_0\|$	$<= 0.2$cm(0.02cm if NSiHit > 0)
χ^2/dof	$<= 4$(3 if run $<= 186598$)
	CMU
CMU Fid	x-fid< 0 cm z-fid < 0cm
$\|\Delta X_{CMU}\|$	$<= 7$cm
CMP veto	Not CMP Fiducial
CMX veto	Not CMX Fiducial
Good Trigger	run $>= 270062$
	CMP
CMP Fid	x-fid< 0 cm z-fid < -3cm
$\|\Delta X_{CMP}\|$	$<= 5$cm
ϕ-gaps	ϕ mod $15^\circ <= 2$ OR $>= 13$
CMU veto	Not CMU Fiducial
	No Bluebeam for run $<= 154449$
Good Trigger	run $>= 229764$
	CMUP
	CMU AND CMP Fiducial
	Otherwise satisfying above CMU/CMP requirements

Table 7.5 Selection for CMUP, CMU, and CMP muons.

	CMX
E_{em}	$<= 2 + max(0, (p - 100)0.0115)$
E_{had}	$<= 6 + max(0, (p - 100)0.028)$
Iso/Pt	$<= 0.1$
NAxl(5 hits)	$>= 3$
NStL(5 hits)	$>= 2$
Track $\|Z_0\|$	$<=$ 60 cm
Track $\|D_0\|$	$<=$ 0.2cm(0.02cm if NSiHit > 0)
χ^2/dof	$<= 4$(3 if run $<=$ 186598)
CMX Fid	x-fid$<$ 0 cm z-fid < -3cm
$\|\Delta X_{CMX}\|$	$<=$ 6cm
ρ_{exit}	$>$ 140cm
Arches	No CMX for run $<$ 150144. No Miniskirt. No Keystone Arches only for all run range Arches removing wedge 14 on West Side for run $>$ 190697
Tracks	BcTrk (Larry's Correction if Data)

Table 7.6 Selection for CMX muons.

	CMXMsKs
E_{em}	$<= 2 + max(0, (p-100)0.0115)$
E_{had}	$<= 6 + max(0, (p-100)0.028)$
Iso/Pt	$<= 0.1$
NAxl(5 hits)	$>= 3$
NStL(5 hits)	$>= 2$
Track $\|Z_0\|$	$<= 60$ cm
Track $\|D_0\|$	$<= 0.2$cm(0.02cm if NSiHit > 0)
χ^2/dof	$<= 4$(3 if run $<=$ 186598)
CMX Fid CMX Fid	x-fid< 0 cm z-fid < -3cm
	$(75^\circ < \phi < 105^\circ$ AND $\|\eta\| < 0)$
	OR
	$(225^\circ < \phi < 315^\circ)$
$\|\Delta X_{CMX}\|$	$< max(6.0, 125.0/p_T)$cm
ρ_{COT}	> 140 cm
Good Trigger	run $>=$ 227704

Table 7.7 CMX Miniskirt and Keystone muon selections.

	BMU
Fiduciality	PES Fiducial
	BMU Fiducial
E_{em}	$<= 2 + max(0, (p - 100)0.0115)$
E_{had}	$<= 6 + max(0, (p - 100)0.028)$
$E_{em} + E_{had}$	> 0.1 GeV
Iso/Pt	$<= 0.1$
Track $\|Z_0\|$	$<= 60$ cm
Track $\|D_0\|$	$<= 0.2$cm(0.02cm if NSiHit > 0)
COT Hit Fraction	> 0.6
C/σ(C)	> 12
NSvxHits	> 3
N_{stub} Hits	> 2
ρ_{BMU}	$471.6 <= \rho_{BMU} <= 766.6$
	OR
	$-433.0 <= \rho_{BMU} <= -764.7$

Table 7.8 BMU muon selection.

	CMIOCES/CMIOPES
E_{em}	$<= 2 + max(0, (p-100)0.0115)$
E_{had}	$<= 6 + max(0, (p-100)0.028)$
Iso/Pt	$<= 0.1$
Uniqueness	Not a CMUP/U/P/X muon
Track $\|Z_0\|$	$<= 60$ cm
Track $\|D_0\|$	$<= 0.2$cm(0.02cm if NSiHit > 0)
$E_{em} + E_{had}$	> 0.1GeV
	CMIOCES
Central	Track CES Fiducial
NAxl(5 hits)	$>= 3$
NStL(5 hits)	$>= 3$
χ^2/dof	$<= 3$
Track	BcTrk (Larry's Correction if Data)
	CMIOPES
Forward	Track PES Fiducial
NSvxHits	> 3
Curvature Significance	> 12
COT Hit Fraction	> 0.6
	No beam contraint on IO tracks

Table 7.9 Selection for CMIOCES and CMIOPES

	CrkTrk/IsoCrkTrk
Track $\|Z_0\|$	<= 60 cm
Track $\|D_0\|$	<= 0.2cm(0.02cm if NSiHit > 0)
NAxl(5 hits)	>= 3
NStL(5 hits)	>= 3
χ^2/dof	<= 3
Uniqueness	Not a CMUP/U/P/X muon
Is in Crack	Not Track CES or PES Fiducial
Conversion	! = 1
Track	BcTrk (Larry's Correction if Data)
	CrkTrk
Iso/P_T	<= 0.1 using CDF Muon OR <= 0.1 using nearest CDF EMObj with $\Delta R < 0.05$
	IsoCrkTrk
Iso/P_T	< 0.125 OR < 0.125 using new cal iso and trkIso < 0.125

Table 7.10 Selection for CrkTrk and IsoCrkTrk.

preclusters in a cone of $R = 0.4$. The centroid of the precluster is calculated from the seed towers' E_T and a cluster is created including towers of $E_T > 100$ MeV. The centroid and cluster are recalculated iteratively until they no longer change or a maximum number of iterations is reached. Corrections to the absolute jet scale are applied as follows:

- Level 0 correction sets the calorimeter energy scale.
- Level 1 correction makes jet energy uniform in eta. Jets outside $0.2 < |\eta| < 0.6$ are scaled to jets inside the region.
- Levels 2 and 3 are no longer in use.
- Level 4 subtracts the average contribution from multiple interactions, parametrized by the number of event vertices.
- Level 5 corrects for non-linearity and energy loss in the un-instrumented regions of the calorimeter.

After these corrections the jet energies can be compared to the Monte Carlo jet energies. Additional corrections can be used to correct the jets to match on average to the energies of the original partons in the fundamental interactions. These higher level out of cone and underlying event corrections are not used to avoid under or overcounting energy in our $\not\!\!E_T$ correction. Instead when measuring jet properties we compare our jets directly to jets formed from hadrons clustered using the same technique, which are largely equivalent to jets formed from calorimeter towers, after an unfolding technique described in Section 10.5.3 is applied to account for detector resolution and uncorrected energy loss. Jets must be isolated from leptons, those within a cone of $\Delta < 0.4$ are not counted.

7.4.1 b Quark Identification

The signature of top quark decay is the presence of b quark and a W boson, which for pairs of top quarks can mimic our signal. As such, identifying b quarks (b-tagging) is important for

identifying events in which top quarks are produced. As the second-most massive quark, the b is sufficiently long-lived to hadronize, but the hadrons travel a mean distance of only 500 microns before decaying within the beam pipe, before reaching any element of the detector. These particles are generally identified by the presence of a displaced vertex, due to the distance traveled by the hadron before decaying. In the search for a Higgs boson decaying to WW, b quarks are identified by the SecVtx tagging algorithm [70]. SecVtx starts with the vertex closest to the triggered lepton, then determines the position of the primary vertex by fitting tracks within ΔZ of ± 1 cm. For each jet, tracks are identified that pass quality cuts. SecVtx attempts to reconstruct a secondary vertex based on three tracks with a significant impact parameter compared to the primary vertex, or two higher-quality tracks if the first attempt is unsuccessful. Significant decay length, defined as the projection of the vector from the primary to secondary vertex onto the jet axis in $r - \phi$, is required to tag a jet. SecVtx Tight has an efficiency of 39% with a mistag rate of 1.4%. In the measurement of the WW cross section, the Higgs Optimized B Identification Tagger (HOBIT) [71] is used. HOBIT combines inputs from a number of previous CDF b-taggers, including SecVtx. These inputs include information about the impact parameter and impact parameter significance, the p_T of tracks relative to the jet, and the presence of muons due to the b hadron decay. Variables are combined in a neural network, the output of which corresponds to the probability that a jet originated from a b. The operating point is defined as the point on the neural net above which a jet is considered to be b-tagged. We find the best signal to background ratio at an operating point of 0.95. This operating point corresponds to a tagging efficiency of 51% with a mistag rate of 1.65%. Note that the information needed by HOBIT is not generally available in the skimmed data used in analyses. For this reason a database of jet information is created. Jet are matched to the database by run and event information and basic jet kinematics, and the b-tag output is read out. Note that it is possible to misidentify a light jet as a b-jet. This is accounted for by applying a mistag matrix to light-jet Monte Carlo. HOBIT performs differently in data and Monte Carlo, necessitating scale factors also be applied. The silicon detector is needed for b-tagging, but in order to maximize acceptance

we include certain events from a small number of runs that do not have silicon information. This is addressed by assuming that the fraction of events with b-jets is the same in events with and without silicon. The $t\bar{t}$ monte carlo is scaled up by 1.02 in the Higgs search and 1.04 in the WW cross section measurement to account for the expected number of b-jet events that were not tagged.

7.5 Missing Transverse Energy Reconstruction

The first step in calculating $\not\!\!E_T$ is to sum transverse energy over the entire calorimeter, using the highest $\sum p_T$ vertex to define directions. Muons are corrected for by subtracting the measured p_T and adding back the calorimeter E_T. For jets that are not matched to leptons, the correction is to subtract corrected E_T and add back raw E_T. CrkTrk leptons are treated as muons because we do not know how much energy was lost for any lepton in the crack. We define two related quantities for use in this analysis. The first is $\not\!\!E_{Tspec}$: $\not\!\!E_T$, multiplied by $\sin(\Delta\phi)$ to the closest lepton or jet if there is one within $\frac{\pi}{2}$ of the $\not\!\!E_T$. If the transverse energy of a lepton or jet is undermeasured, resulting in apparent $\not\!\!E_T$. However this will tend to be parallel to the mismeasured object, and so will contribute minimally to the $\not\!\!E_{Tspec}$. The second variable is the $\not\!\!E_{Tsig}$: $\not\!\!E_T$ divided by the square root of the total E_T. Fluctuations in calorimeter activity in events with greater transverse energy could also result in apparent $\not\!\!E_T$, but $\not\!\!E_{Tsig}$ in such an event will be low. The main background that enters our sample through apparent $\not\!\!E_T$ is Drell-Yan, which has a large production cross section but no neutrinos. Both of these variables are used to identify and reduce this background.

7.6 Trigger and Reconstruction Efficiency Factors

The efficiency of lepton triggering and identification is determined by a tag and probe method. Z candidates are selected in a dilepton invariant mass window of $76 < m_{ll} < 106$ GeV with one tag leg that satisfies full lepton selection, and one probe leg, satisfying the selections defined in Tables 7.11- 7.12. The probe selection efficiency approaches 100% and is expected to be well modeled by Monte Carlo. A sideband subtraction is performed using

the Z mass sidebands from $61 - 76$ and $106 - 121$ GeV, and the efficiency for the probe lepton to pass the full selection is evaluated. A scale factor is applied to account for the difference in efficiencies in data and Monte Carlo. The tracking efficiency for forward leptons is separately evaluated with the PHX tracking probe.

7.7 Data Driven Background Estimates

The W+jets background, in which a jet is incorrectly reconstructed as a lepton, depends on detector and jet evolution effects that are difficult to model. For this reason a data-driven modeling method is employed. The fake rate is calculated in events collected with a jet trigger.

$$f_i \equiv \frac{N_i(\text{IdentifiedLeptons}) - \sum_{\text{j}\in\text{EWK}} \text{N}_{\text{ij}}(\text{IdentifiedLeptons})}{N_i(\text{DenominatorObjects}) - \sum_{\text{j}\in\text{EWK}} \text{N}_{\text{ij}}(\text{DenominatorObjects})} \tag{7.1}$$

The selection for denominator objects is shown in Table 7.13- 7.14, with fiduciality requirements appropriate to each lepton category. Background subtraction is performed with Monte Carlo to correct for events with real leptons in the jet trigger samples. The numerator is then those events passing the full selection of the relevant category. Fake rates range from 0.005 to 0.015 for central electrons and from 0.005 to 0.06 for plug electrons. In both cases the fake rate decreases sharply to a minimum at $E_T = 60$ GeV, slowly increasing thereafter. Fake rates for CMUP/U/P/X muons range from 0.005 to 0.1, and tend to increase slightly with p_T. BMU and CMIOPES muon fake rates peak at low p_T at 0.03 and 0.06 respectively before decreasing to zero. CrkTrk and IsoCrkTrk fake rates are approximately 0.04 and 0.2 respectively, and increase slightly with E_T. The fake rate is applied to a set of W+jets events, where the jets pass the denominator selection. Events are multiplied by the appropriate fake rate, calculated as a function of jet kinematics, in order to determine the rate and distribution of W+jets events misidentified as dilepton events. Events in which two jets are misidentified as leptons are considered a negligible background.

Central Electron Probe
Track or SMX fiducial to CES
Track p_T >= 5
Track Z_0 <= 60cm

PHX ID Probe
Pes2DEta $1.2 < \|\eta\| < 2$
Had/Em <= 0.05
PhxMatch: True
NSiHits >= 3
$\|\text{TrackZ}_0\|$ <= 60cm

PHX Tracking Probe
Pes2DEta $1.2 < \|\eta\| < 2$
Had/Em <= 0.05
Iso/Et <= 0.1
PEM3x3FitTower: True
PEM3x3χ^2 <= 10
Pes5x9U >= 0.65
Pes5x9V >= 0.65
ΔR(Pes,PEM) <= 3.0

PEM Probe
$1.2 <$ PES$\eta < 2.8$
Had/Em < 0.125

Table 7.11 Electron efficiency probes

Central Muon Probe
Track not PES Fiducial
NAxL(5 hits) >= 2
NStL(5 hits) >= 2
Track $\|Z_0\|$ <= 60cm

Forward Muon Probe
Track PES Fiducial
Cot Hit Fraction > 0.6
Track $\|Z_0\|$ <= 60cm

Table 7.12 Muon efficiency probes

FakeableCEM
Track fiducial to CES
Had/Em <= $0.125 + 0.00045E$
Iso/E_T <= 0.3
IsConversion ! = 1

FakeablePHX
Pes2DEta $1.2 < \|\eta\| < 2$
Had/Em <= $0.125 + 0.00045E$
PhxMatch: True
NSiHits >= 3
|TrackZ$_0$| <= 60cm
Iso/E_T <= 0.3

FakablePEM
$1.2 <$ PES$\eta < 2.8$
Had/Em <= $0.125 + 0.00045E$
Iso/E_T <= 0.3 No PhxMatch with
NSiHits >= 3 and |TrackZ$_0$| <= 60cm

Table 7.13 Electron fake rate denominators

FakeableMuonCentral
Track not PES Fiducial
NAxL(5 hits) >= 2
NStL(5 hits) >= 2
Track $\|Z_0\|$ <= 60cm
Track $\|D_0\|$ <= 0.2cm (0,02 cm if NSiHit> 0)
χ^2/dof <= 4 (3 if run <= 186598)
Iso/E_T <= 0.3

FakeableMuonForward
Track PES Fiducial
Cot Hit Fraction > 0.6
Track $\|Z_0\|$ <= 60cm
Track $\|D_0\|$ <= 0.2cm (0,02 cm if NSiHit> 0)
χ^2/dof <= 4 (3 if run <= 186598)
Iso/E_T <= 0.3

Table 7.14 Muon fake rate denominators

Chapter 8

Event Selection

8.1 $H \rightarrow WW$ Analysis Selection

The leptonic WW final topology is characterised by two high-$E_T(p_T)$ leptons of opposite charge, with substantial missing transverse energy. The analysis begins with lepton based triggers with a threshold of 18 GeV described in Section 5.2.8. In the search for a Higgs boson decaying to a WW pair, a base signal region is defined, beginning with a single electron(muon) of $E_T(p_T) > 20$ GeV$(/c)$, in order to ensure uniform trigger efficiency. A second lepton of opposite charge is required, with the $E_T(p_T)$ requirement relaxed to 10 GeV$(/c)$ to increase acceptance. Events in which the muons are tagged as originating from a cosmic ray are vetoed. The leptons are required to be less than 4 cm apart, and have less than 10% calorimeter E_T and track p_T in a cone of $\Delta R = 0.4$. The dilepton invariant mass is required to be greater than 16 GeV$/c^2$ to suppress $W\gamma$ and low-mass backgrounds. Requiring $\not\!\!E_{T,spec} > 25$ GeV helps to suppress events in which the E_T of a lepton or jet has been mismeasured, resulting in apparent $\not\!\!E_T$. Because the primary background that enters the sample this way is Drell-Yan, the requirement is relaxed to 15 GeV for $e - \mu$ events. The two or more jet analysis uses the base selection, with the additional requirement of two or more jets. In the two or more jet region, events are rejected if one or more jets are tagged as b-jets by SecVtx. Events after selection are shown in Tables 8.1-8.2. The dominant background is $t\bar{t}$, which decays to WW and two b-jets. Other substantial backgrounds include Drell-Yan with false $\not\!\!E_T$ due to mismeasurement of a lepton or jet, W+jets where a jet has been reconstructed as a second lepton, and WW. WZ and ZZ, where a boson decays

hadronically or a lepton is lost, contribute a small number of events, as does $W\gamma$ with the photon misidentified as a lepton.

8.2 WW Analysis Selection

The selection for the WW cross section measurement is largely the same as in the HWW search. Two additional requirements are made to reduce the Drell-Yan background. Events with a dilepton mass in a window around the Z ($80 < m_{ll} < 99$ GeV/c^2) are vetoed, unless they are $e - \mu$. The angle between the dilepton pair and $\not\!\!E_T$ ($\Delta\phi(ll, \not\!\!E_T)$ is required to be greater than one to suppress $Z \to \tau\tau$ events. Events are separated by jet multiplicity into zero, one, and two or more jet categories for analysis. One jet events are further separated by transverse energy into bins of $15 < E_T < 25$ GeV, $25 < E_T < 45$ GeV, and $E_T > 45$ GeV. Events with two or more jets are rejected if one or more jets is tagged as a b-jet by HOBIT, with an operating point of 0.95. Events after selection are shown in Table 8.3. Backgrounds vary by jet multiplicity. In the zero jet region W+jets is dominant, followed by $W\gamma$ and Drell-Yan. In the one jet region W+jets remains dominant, with Drell-Yan and $t\bar{t}$ contributing significantly. Note that in these $t\bar{t}$ events one b-jet has been lost. The two or more jet region is similar to the HWW search region, with $t\bar{t}$ the dominant background. W+jets and Drell-Yan also contribute significantly, though Drell-Yan has been heavily suppressed by cuts.

CDF Run II Preliminary	$\int \mathcal{L} = 9.7$ fb^{-1}		
$M_H = 165$ GeV/c^2			
$t\bar{t}$	287	$\pm$	42
DY	150	$\pm$	64
WW	53	$\pm$	12
WZ	11.7	$\pm$	2.2
ZZ	5.3	$\pm$	1.0
W+jets	80	$\pm$	15
$W\gamma$	8.3	$\pm$	2.1
Total Background	596	$\pm$	96
$gg \rightarrow H$	5.0	$\pm$	2.5
WH	4.35	$\pm$	0.61
ZH	2.16	$\pm$	0.29
VBF	2.51	$\pm$	0.41
Total Signal	14.0	$\pm$	2.9
Data	596		

AllSB-2JOS

Table 8.1 Event yields after HWW initial selection in the two or more jet region

$M_H = 125$ GeV

Process	OS 0 Jet High S/B Lep.	OS 0 Jet Low S/B Lep.	OS 1 Jet High S/B Lep.	OS 1 Jet Low S/B Lep.
$gg \to H$	6.9 ± 2.1	2.4 ± 0.7	2.8 ± 1.2	0.91± 0.39
WH	0.41 ± 0.07	0.16 ± 0.03	0.87 ± 0.14	0.30± 0.05
ZH	0.25 ± 0.04	0.08 ± 0.01	0.27 ± 0.04	0.10± 0.02
VBF	0.04 ± 0.01	0.013 ± 0.003	0.23 ± 0.04	0.07± 0.01
Total Signal	7.6 ± 2.1	2.6 ± 0.7	4.2 ± 1.2	1.4± 0.4
Process	OS 2+ Jets	OS Inverse $M_{\ell\ell}$	SS 1+ Jets	
$gg \to H$	1.07±0.53	1.81±0.30	–	
WH	1.59±0.22	0.10±0.02	1.25±0.17	
ZH	0.76±0.10	0.06±0.01	0.18±0.02	
VBF	0.55±0.09	0.05±0.01	–	
Total Signal	3.98±0.71	2.02±0.30	1.43±0.17	

Table 8.2 Higgs Event yields across subchannels

WW($ll\nu\nu$) Cross Section	CDF Run II Preliminary	$\int L = 9.7$ fb^{-1}	
Process	Events (Best Fit)		
	0 Jets	1 Jet	2 or More Jets
WZ	19.8 ± 3.0	16.8 ± 2.3	4.30 ± 0.82
ZZ	13.3 ± 1.9	4.29 ± 0.62	1.35 ± 0.26
$t\bar{t}$	3.7 ± 1.1	77 ± 12	159 ± 16
DY	157 ± 34	84 ± 21	20.2 ± 7.4
$W\gamma$	214 ± 27	44.0 ± 6.8	7.5 ± 1.9
W+jets	681 ± 118	249 ± 47	80 ± 15
Total Background	1088 ± 124	475 ± 57	273 ± 26
WW	961 ± 91	223 ± 29	73 ± 19
Signal+Background	2050 ± 177	698 ± 73	345 ± 39
Data	2090	682	331

Table 8.3 Event yields after WW initial selection

Chapter 9

Background Studies

9.1 Control Regions

Control regions are defined for all significant backgrounds: Drell-Yan, W+jets/$W\gamma$, and $t\bar{t}$. WW, a background for the HWW search, is validated through the differential cross section measurement. Control regions are chosen to be orthogonal to the signal region, but as kinematically similar as possible. The control regions maximize the purity and statistics of the process of interest in order to validate our modeling.

9.1.1 Drell-Yan

We consider opposite-sign dileptons in the Z mass region $76 < M_{ll} < 106$ GeV which is completely dominated by the Drell-Yan process. We require one trigger lepton, a second lepton with $E_T > 10$ GeV, and include events with any number of jets. We require $15 < \not\!\!E_{Tspec} < 25$ GeV, and either ee, $\mu\mu$, or e/μ+track leptons. The $\not\!\!E_{Tspec}$ cut enforces orthogonality of the control region while still having some $\not\!\!E_{Tspec}$ in order to be representative of the background in the signal region. Figure 9.2 shows generally good agreement with Monte Carlo. In the case of jet multiplicity some discrepancy is observed, but prediction is consistent with data to within uncertainties. $\not\!\!E_T$ has been shifted down by 4 GeV in order to agree with data, and the dominant uncertainty is the acceptance uncertainty assessed by a ± 2 GeV shift. Modeling of $\not\!\!E_T$ is related to jet multiplicity as jet fragments slipping through calorimeter cracks is a source of $\not\!\!E_T$ that is difficult to model. In the two or more jet region,

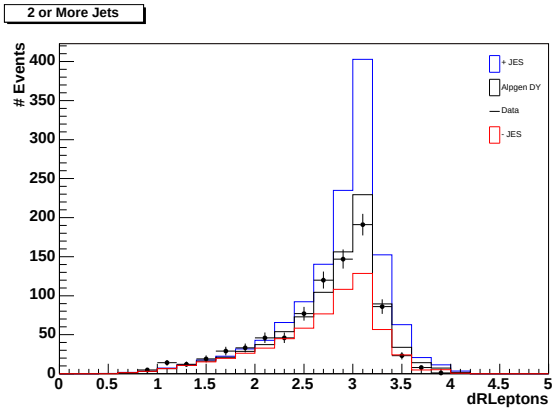

Figure 9.1 The effect of jet energy scaling on dRLeptons in the 2 jet control region

some general shape mismodeling of distributions is observed. However, uncertainty in Jet Energy Scale (JES) well covers the discrepancy, as shown in Figure 9.1.

9.1.2 Same-Sign

To check modeling of the W+jets and $W\gamma$ fake backgrounds we reverse the opposite sign requirement on the signal selection criteria. We include events with any number of jets. The result is a region dominated by fake leptons originating from either jets or photons as shown in Figure 9.3. We observe good agreement in observed and predicted event yields and kinematic distributions.

9.1.3 Top Quark Pair Production

Events with at least one b-tagged jet are removed from the signal region and examined as a ttbar control region. The region is otherwise kinematically identical to the two or more jet signal region, as the b-jet identification efficiency is not strongly dependent on jet kinematics. Plots of various kinematic variables shown in Figure 9.4 demonstrate agreement within uncertainties between MC prediction and data.

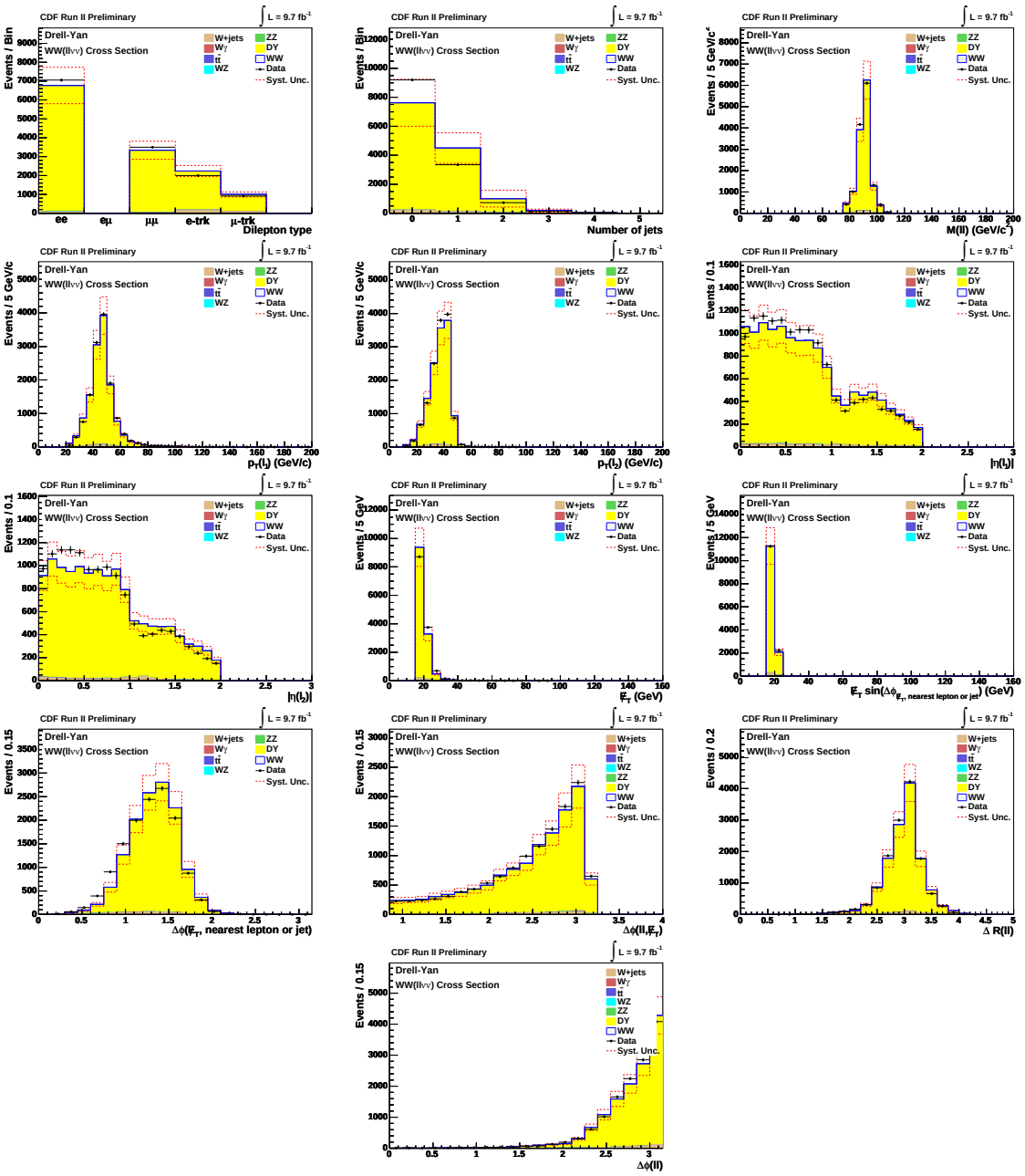

Figure 9.2 jet-inclusive Drell Yan control region

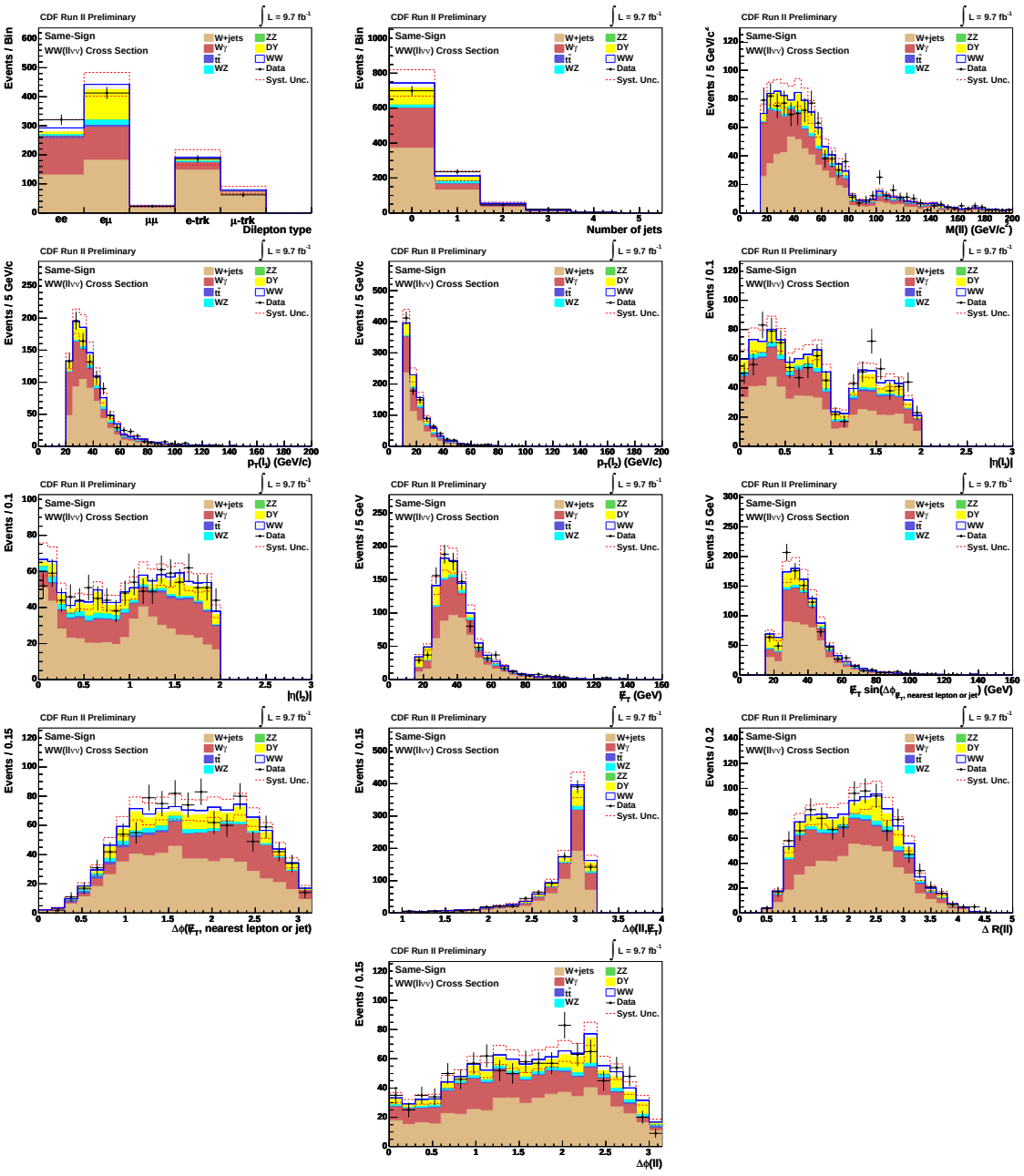

Figure 9.3 Jet-inclusive same sign control region

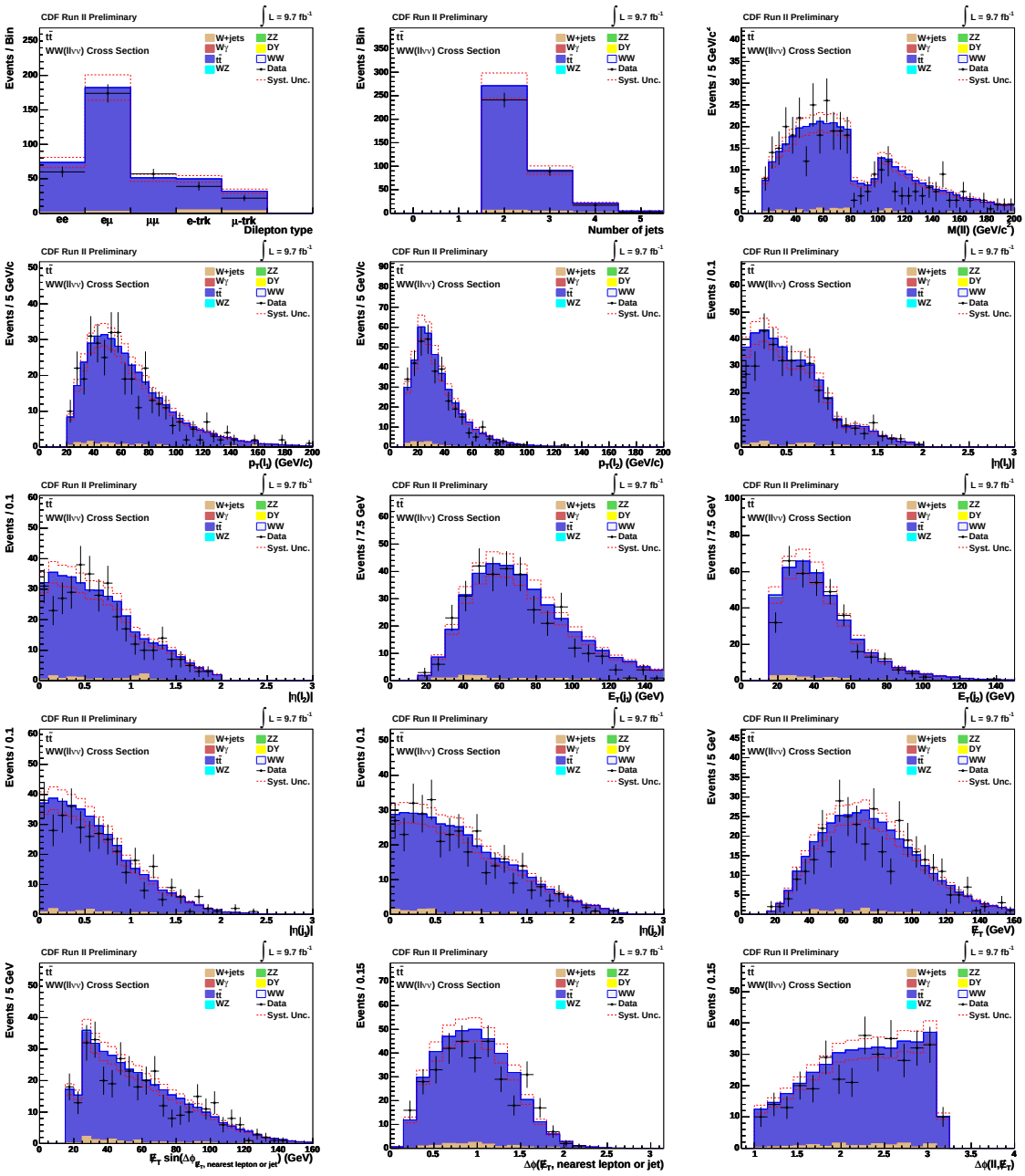

Figure 9.4 $t\bar{t}$ control region

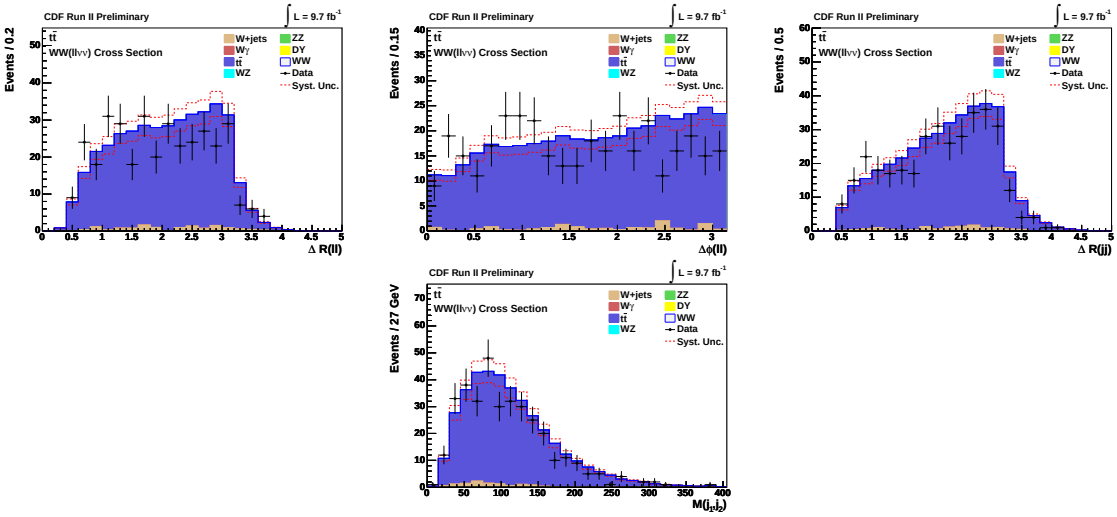

Figure 9.5 $t\bar{t}$ control region continued

Chapter 10

Analysis Method

The signal region is divided by the number of jets, as each jet bin contains particular types of signal and background. This allows optimal techinques and discriminating variables to be chosen for the combination of signal and background in each region. In the Higgs search, the signal is further divided, as discussed in Section 10.3.

10.1 Matrix Element Method

In the 0-jet region we are able to make use of leading order matrix element calcuations using leading order matrix elements from the MCFM[44] package. For each event a matrix element probability is calculated for the processes ZZ, WW, W+jets, and $W\gamma$. The probability is given by

$$P(\vec{x_{obs}}) = \frac{1}{\langle\sigma\rangle} \int \frac{d\sigma_{th}(\vec{y})}{d\vec{y}} \epsilon(\vec{y}) G(\vec{x_{obs}}, \vec{y}) d\vec{y} \tag{10.1}$$

where the variables are as follows

- $\vec{x_{obs}}$ - observed lepton momenta and $\not{E}_T(x, y)$
- $\vec{y}$ - true (unknown) lepton 4-vectors
- σ_{th} - leading order theoretical cross section
- $\epsilon(\vec{y})$ - efficiency and acceptance
- $G(\vec{x_{obs}}, \vec{y})$ - detector resolutions effects

- $1/\langle\sigma\rangle$ - normalization

The function efficiency $\epsilon(\vec{y})$ describes the probability for a generator level lepton, photon, or parton to be reconstructed as an analysis level lepton. Because the neutrinos are unobserved in the final state their energy and direction must be integrated out under the constraint of the observed magnitude and direction of the $\not\!\!\vec{E}_T$. A likelihood ratio is constructed from the probability densities:

$$LR_S(x_{obs}) \equiv \frac{P_S(x_{obs})}{P_S(x_{obs}) + \Sigma_i k_i P_i(x_{obs})} \tag{10.2}$$

Where k_i is the expected fraction for each background, and $\Sigma_i k_i = 1$. The likelihood ratio was used as the final discriminant in the previous WW cross section measurement. It can be used in the zero jet region because zero jet events are well described by leading order calculations. It offers powerful discrimination for any region of the phase space by directly comparing the likelihood of the observed kinematics being consistent with signal or background. However, the quality of separation is reduced by detector and reconstruction smearing, there is considerable overlap with the neural network kinematic inputs, and the matrix elements are computationally intensive to calculate for events with additional jets. For these reasons the likelihood ratio is included as a neural network input in the zero jet region and not used elsewhere.

10.2 Neural Net Method

Neurobayes [72] neural networks are trained to enhance the separation of signal from background while preserving acceptance. Three layers are used, with N_I input nodes in the first layer, N_I+1 nodes in the second layer, and a single output node in the third layer. Neural networks are trained on kinematic inputs, which are chosen based on the underlying physical features of the signal and background processes. Inputs are selected on the basis of physics considerations of what kinematic quantities should distinguish signal from background, as well as direct studies using simulated event distributions. Only kinematic inputs that are

well-modeled by simulation are included. A subset of simulated events is used to train the neural network, reweighted so that the sum of weights is equal to the number of generated and simulated signal events. Neural networks are trained separately for different jet regions to exploit different background composition and signal features. The cross section is determined from a simultaneous fit to each final discriminant template.

10.2.1 WW Zero Jet Region

In the zero jet region dominant background are W+jets, $W\gamma$, and Drell-Yan. The scalar sum of lepton, jet, and missing transverse energy is the most significant discriminant, due to the higher characteristic energy of the WW process. The rapidly falling p_T distribution of fake leptons makes $p_T(l_2)$ a significant input. The likelihood ratio has already been discussed above. The invariant mass of the lepton pair is especially low for $W\gamma$, where the photon is often colinear with the W. And in zero jet Drell-Yan production, the leptons tend to be produced back to back in ϕ. Other inputs of lesser significance are $M_T(ll\not\!\!E_T)$, $p_T(l_1)$, $E(l_1)$ and $\Delta R(ll)$. These inputs are shown in Figure 10.1, and the resultant output in Figure 10.2. The neural network output score is a measure of how signal like a given event is. Good separation of signal from background is achieved, with the background region dominated by W+jets.

10.2.2 WW One Jet Region

Dominant backgrounds in this region are W+jets, Drell-Yan, and $t\bar{t}$. Once again the scalar sum of transverse energy is the most significant input, followed by $p_T(l_2)$. The presence of an additional jet in these events makes $\not\!\!E_{T,spec}$ a more significant input, as it is low in events where apparent $\not\!\!E_T$ is due to a mismeasured jet. Other inputs are $E(l_1)$, $\Delta R(ll)$, $M_T(ll\not\!\!E_T)$, $p_T(l_1)$, and m_{ll}. These input are shown in Figure 10.3, and the neural network output in Figure 10.4. Note that $t\bar{t}$ is particularly difficult to discriminate in this region, though it will be better constrained in the two or more jet region. The one jet region has

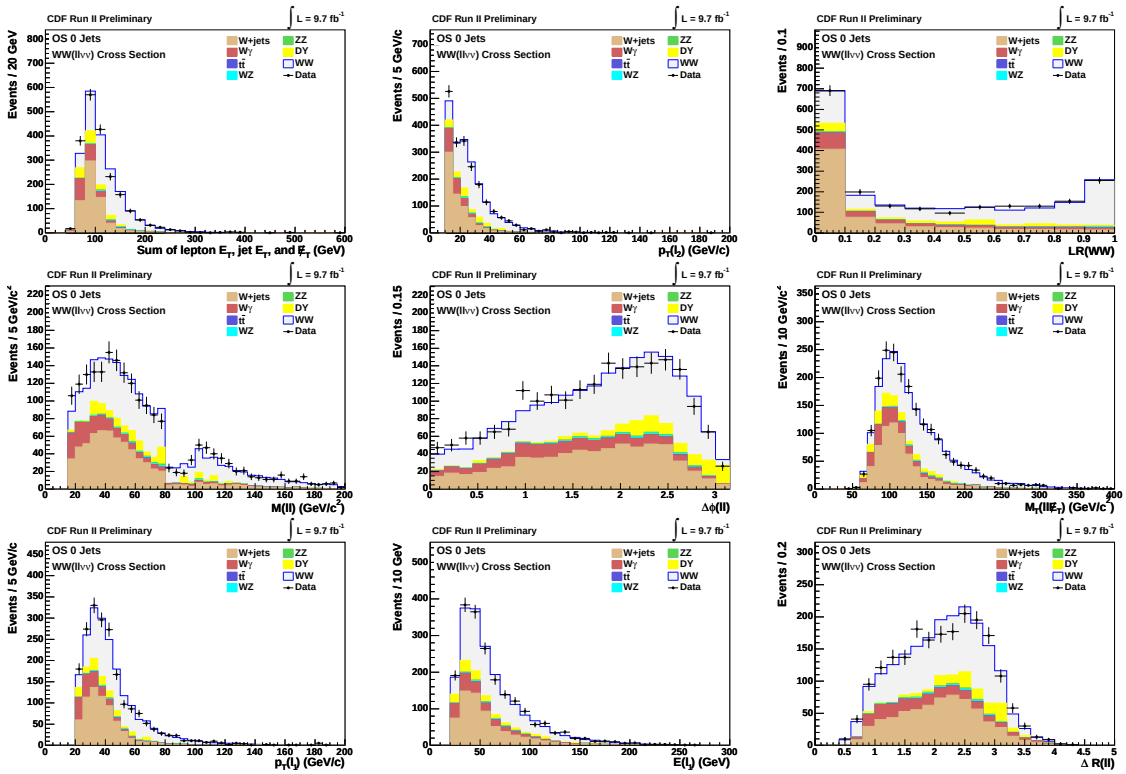

Figure 10.1 0 jet neural net inputs, ordered by significance

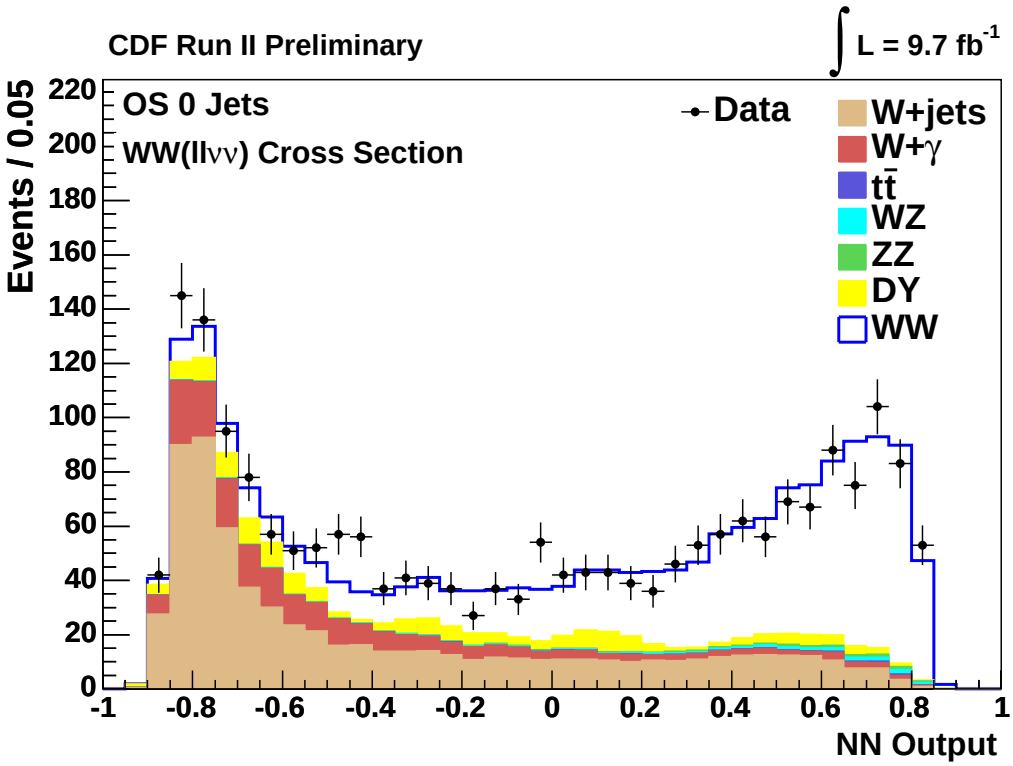

Figure 10.2 0 jet neural net output

the best isolation of the Drell-Yan background. This output is further separated by jet E_T into three templates in order to extract a differential cross section.

10.2.3 WW Two or More Jet Region

In the two or more jet region, the dominant background, even after b-tagging, is $t\bar{t}$, followed by W+jets and Drell-Yan. The scalar sum of transverse energy is still the most significant input, as the characteristic energy of $t\bar{t}$ is even higher than that of WW. The higher energy of $t\bar{t}$ decay products is also visible in the distribution of $p_T(j_1 j_2)$. $\not\!\!E_{T,spec}$ and $p_T(l_2)$ are also present as in the one jet region. Other inputs of lesser significance are $\not\!\!E_T/\sqrt{E_T}$, the aplanarity (a measure of transverse momentum out of the event plane), $M_T(ll\not\!\!E_T)$, $\Delta R(ll)$, $E_T(ll, j_n)$, $M_T(ll\not\!\!E_T j_n)$, $\cos(\Delta\phi(ll_{CM}))$, $\Delta\phi(ll, \not\!\!E_T)$, $E_T(j_n, \not\!\!E_T)$, m_{ll}, $p_T(l_1)$, $\cos(\Psi_{l2})$, and $\Delta\phi(ll)$. These inputs are shown in Figure 10.5, and the output in Figure 10.6. Separation of signal from background is most difficult in this region, but signal enhanced and background enhanced regions are evident, with the background enhanced region dominated by $t\bar{t}$.

10.2.4 Higgs Two or More Jet Neural Network

Neural networks are also used in the Higgs search to enhance separation of signal from background. In the two or more jet region, associative production and vector boson fusion account for approximately 75% of the total signal at a Higgs mass of 125 GeV. These processes have distinctive signatures in the kinematics of jets, either from the decay of the associated vector boson or the radiating quarks. In order to take advantage of these signatures, jet kinematics are included in the HWW neural network. A difficulty in including these variables is the gluon fusion signal. This process has no jets at leading order, and was modeled in Pythia, meaning that the kinematics of individual jets may not be well described. For this reason, one neural network is trained for associative production and vector boson fusion taking advantage of individual kinematics, while a second neural network is trained for gluon fusion without these additional variables. The final discriminant is taken to be the higher of the two neural network outputs, and signal events generally score higher in the

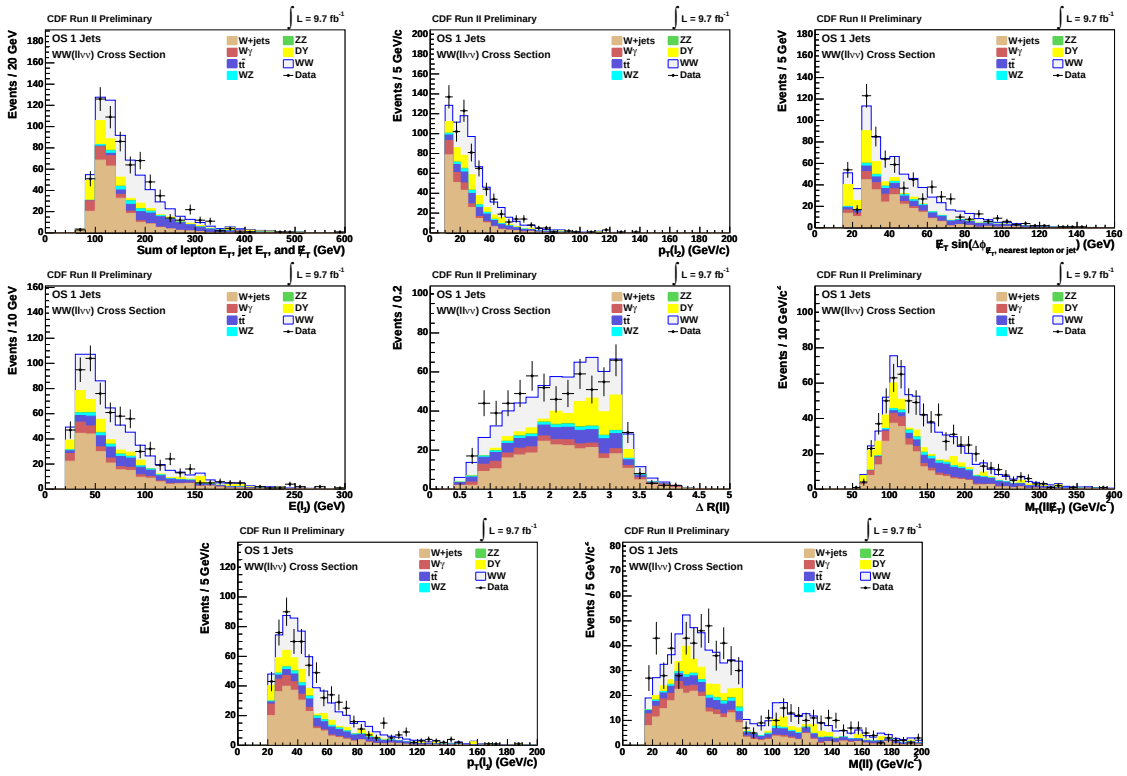

Figure 10.3 1 jet neural net inputs, ordered by significance

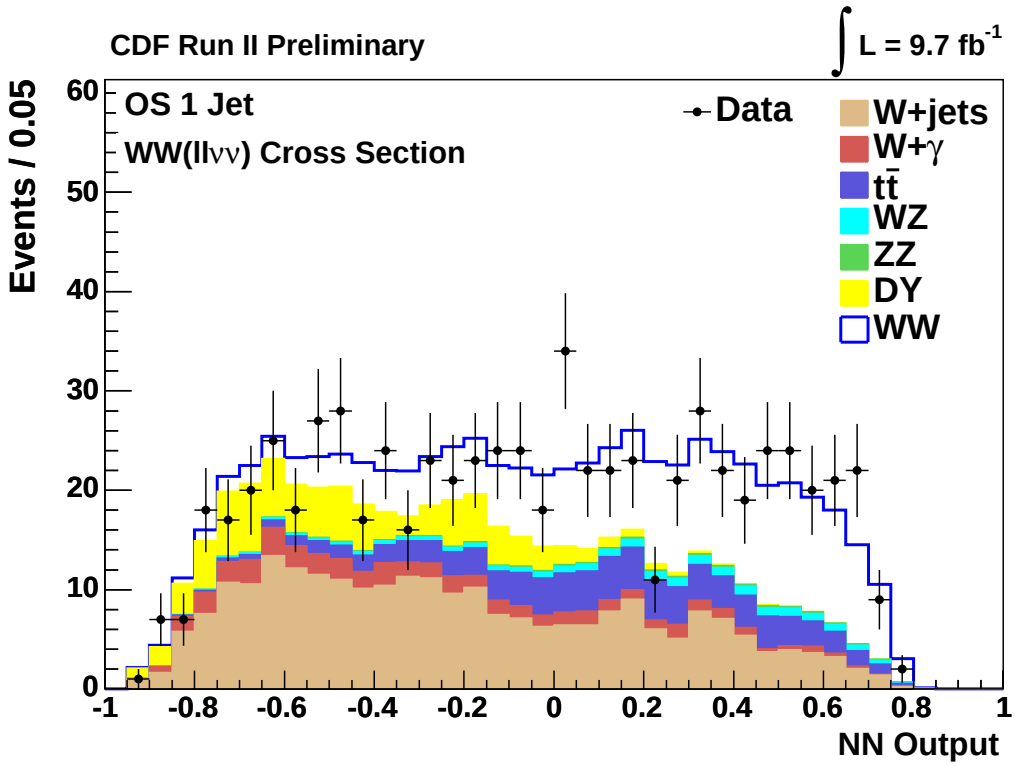

Figure 10.4 1 jet neural net output

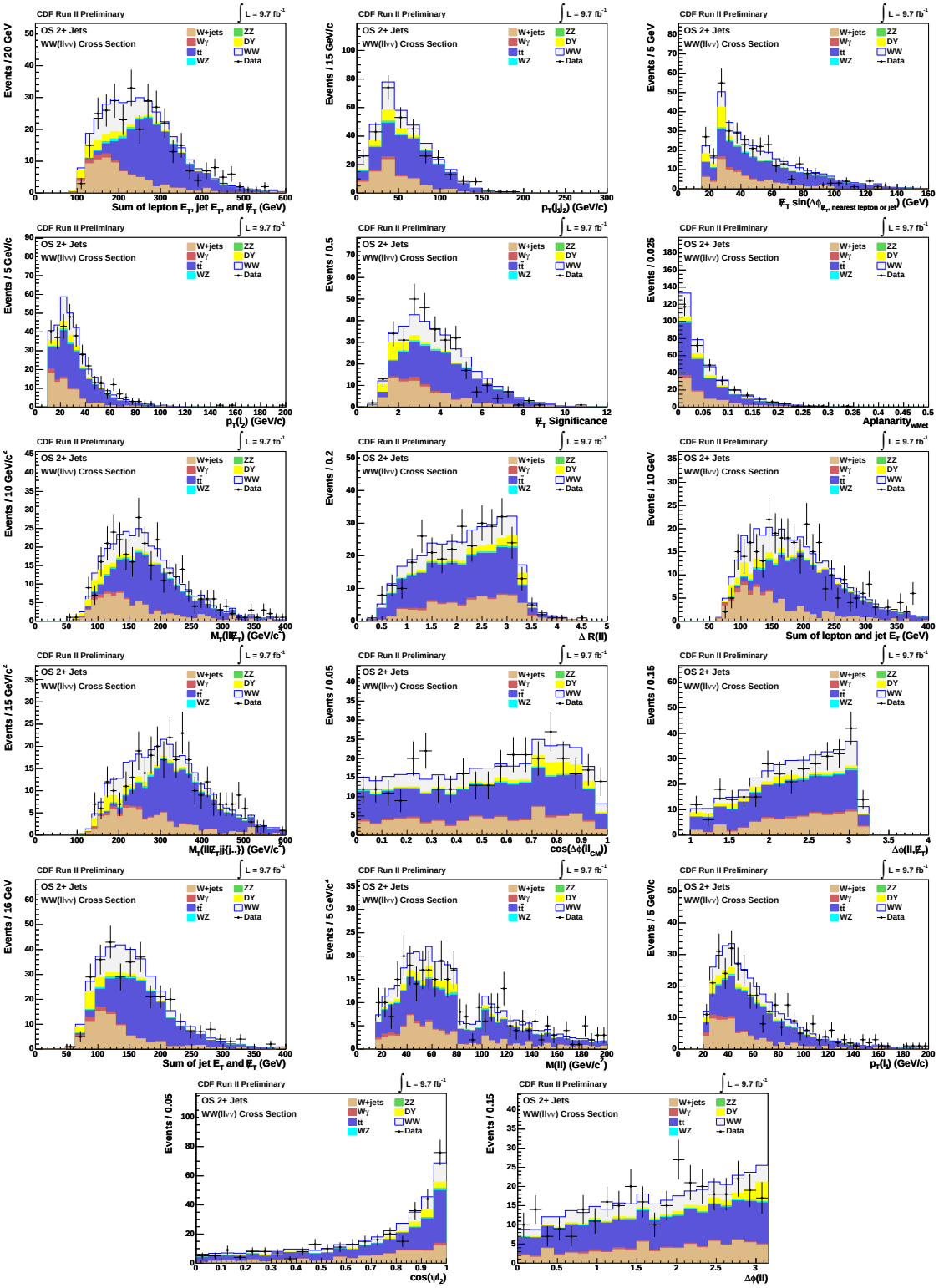

Figure 10.5 2 or more jet neural net inputs, ordered by significance

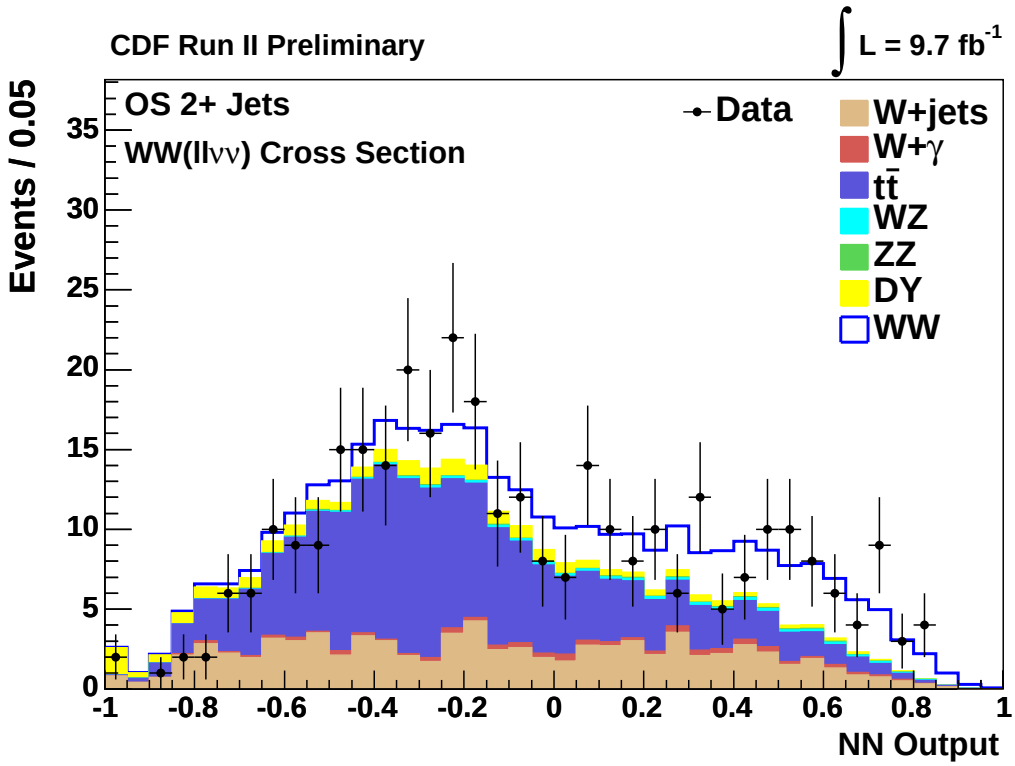

Figure 10.6 2 or more jet neural net output

appropriate neural network. In order to account for gluon fusion events that score higher in the VBF/VH neural network, we include a shape systematic assessed by comparing the gluon fusion neural network score to the higher of the two scores for gluon fusion Monte Carlo as shown in Figure 10.9. Inputs to the neural network include the dilepton mass, effective at rejecting Drell-Yan; the dijet mass, reconstructing the hadronically decaying vector boson in associative production or reflecting the large rapidity gap in vector boson fusion; the sum of transverse energy in the event, characteristic for each process; $\Delta\phi(ll, \not{E}_T)$, particularly low for $Z \to \tau\tau$ events. $\Delta R(ll)$ exploits the spin correlation of the $H \to WW \to ll\nu\nu$ decay. The scalar Higgs boson decays to two spin one W bosons, with spin in opposite directions. The W bosons decay to two spin 1/2 leptons. However, the neutrino must be left-handed, and the anti-neutrino right-handed. As a result they are produced preferentially in the same direction. As a result the charged leptons tend to be produced colinearly as well. These inputs, along with others of lesser significance, are shown in Figure 10.7. Neural networks are trained separately at 5 GeV mass intervals between 110 and 200 GeV in order to optimize the selection in the low-mass region. Outputs are shown in Figure 10.8.

10.3 Other High-Mass Higgs Channels

The $HWW + 2$ or more jets channel is combined with a number of other channels in the high mass Higgs search.

10.3.1 Opposite Sign Zero and One Jet Analyses

These regions contain the majority of the Higgs signal. Dominant backgrounds are WW in the zero jet region and Drell-Yan in the one jet region. The base selection is used, with the additional requirement of zero or one jets. Neural networks are trained on kinematic inputs in the zero and one jet regions as in the two or more jet analysis. However individual jet kinematics are not used. Separate output templates are created for high and low signal to background channels, determined by dilepton type, and then combined in the likelihood

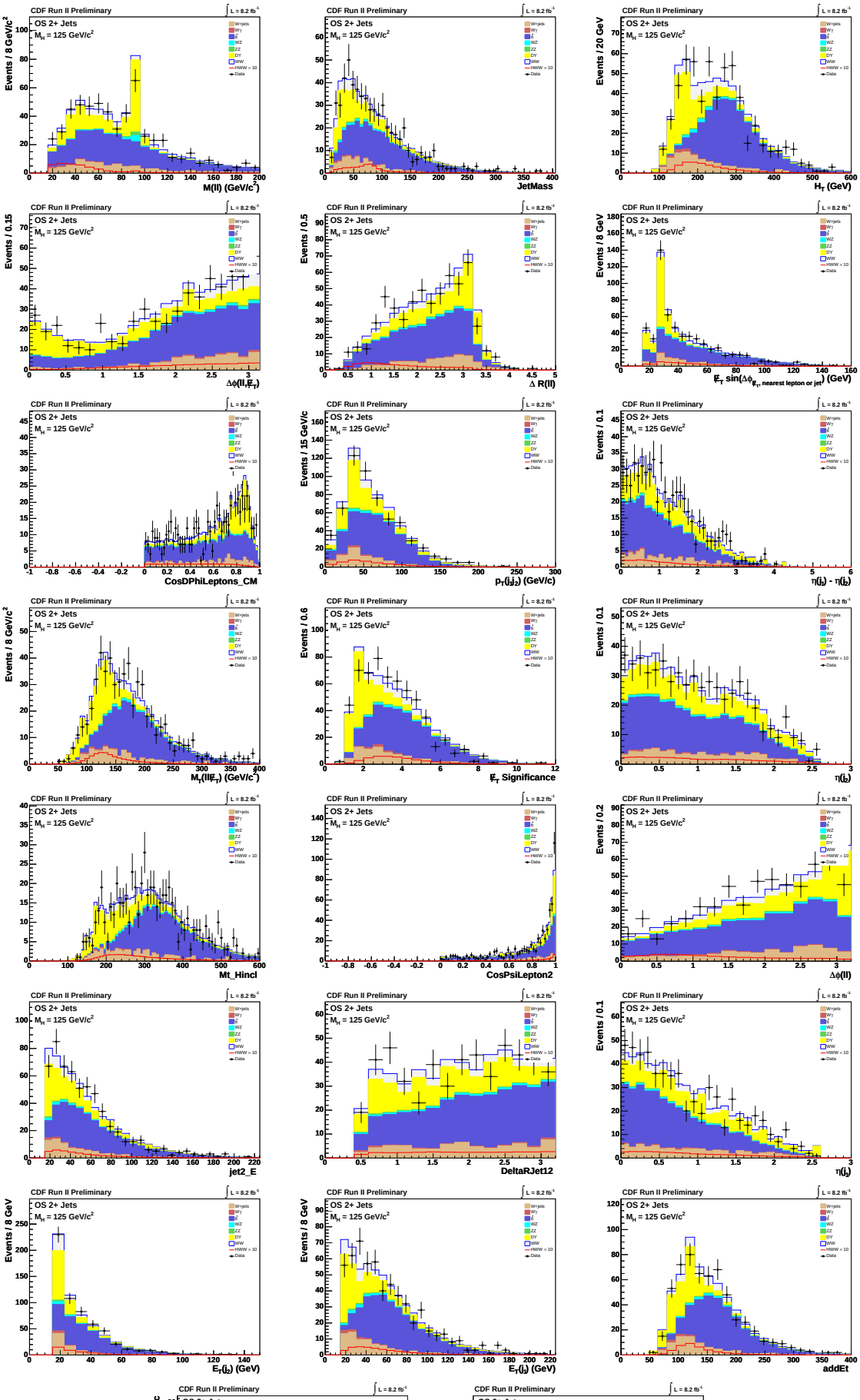
CDF Run II Preliminary
OS 2+ Jets
M_H = 125 GeV/c^2
M(ll) (GeV/c^2)
JetMass
H_T (GeV)
Δφ(ll,ℓ_T)
Δ R(ll)
CosDPhiLeptons_CM
p_T(j_1j_2) (GeV/c)
η(j_1) - η(j_2)
M_T(llℓ_T) (GeV/c^2)
ℓ_T Significance
η(j_2)
Mt_Hincl
CosPsiLepton2
Δφ(ll)
jet2_E
DeltaRJet12
η(j_1)
E_T(j_2) (GeV)
E_T(j_1) (GeV)
addEt

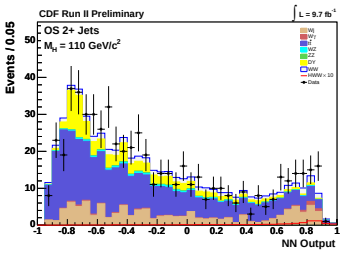
CDF Run II Preliminary
OS 2+ Jets
M_H = 110 GeV/c^2
Events / 0.05
NN Output

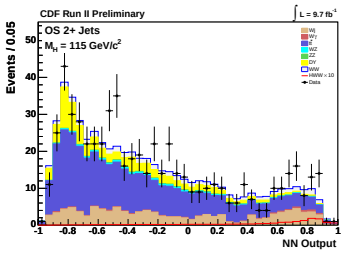
CDF Run II Preliminary
OS 2+ Jets
M_H = 115 GeV/c^2
Events / 0.05
NN Output

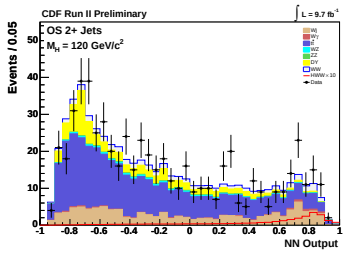
CDF Run II Preliminary
OS 2+ Jets
M_H = 120 GeV/c^2
Events / 0.05
NN Output

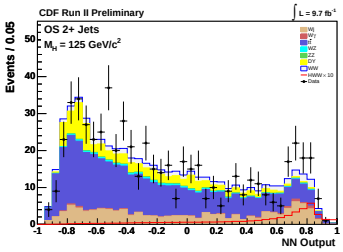
CDF Run II Preliminary
OS 2+ Jets
M_H = 125 GeV/c^2
Events / 0.05
NN Output

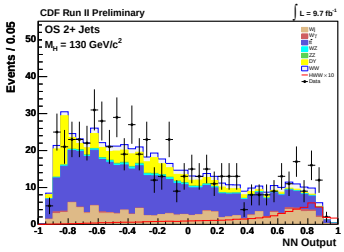
CDF Run II Preliminary
OS 2+ Jets
M_H = 130 GeV/c^2
Events / 0.05
NN Output

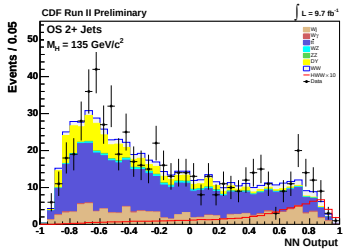
CDF Run II Preliminary
OS 2+ Jets
M_H = 135 GeV/c^2
Events / 0.05
NN Output

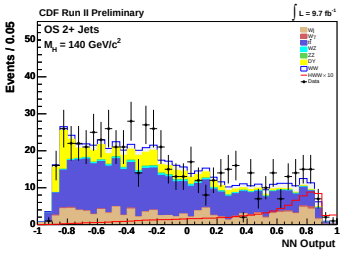
CDF Run II Preliminary
OS 2+ Jets
M_H = 140 GeV/c^2
Events / 0.05
NN Output

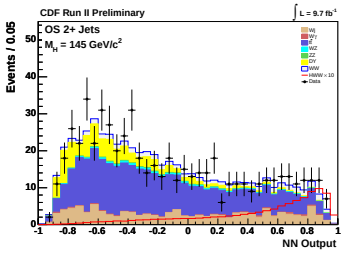
CDF Run II Preliminary
OS 2+ Jets
M_H = 145 GeV/c^2
Events / 0.05
NN Output

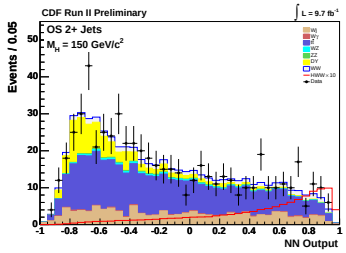
CDF Run II Preliminary
OS 2+ Jets
M_H = 150 GeV/c^2
Events / 0.05
NN Output

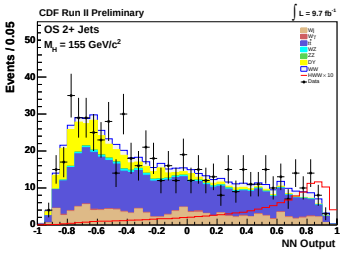
CDF Run II Preliminary
OS 2+ Jets
M_H = 155 GeV/c^2
Events / 0.05
NN Output

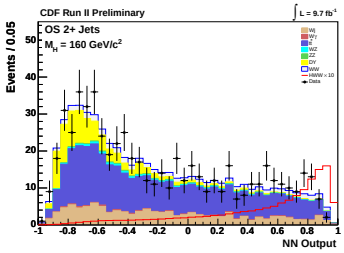
CDF Run II Preliminary
OS 2+ Jets
M_H = 160 GeV/c^2
Events / 0.05
NN Output

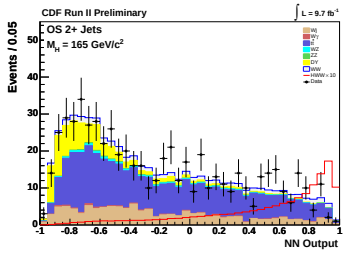
CDF Run II Preliminary
OS 2+ Jets
M_H = 165 GeV/c^2
Events / 0.05
NN Output

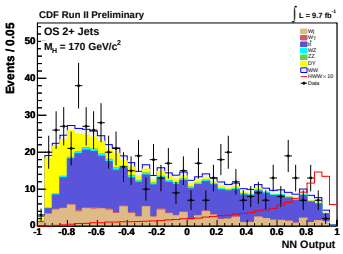
CDF Run II Preliminary
OS 2+ Jets
M_H = 170 GeV/c^2
Events / 0.05
NN Output

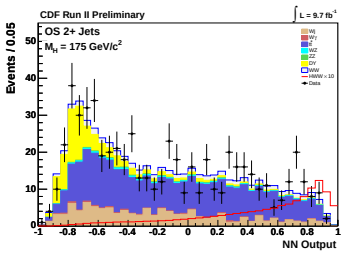
CDF Run II Preliminary
OS 2+ Jets
M_H = 175 GeV/c^2
Events / 0.05
NN Output

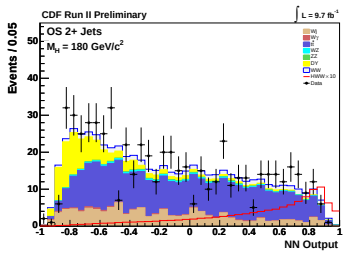
CDF Run II Preliminary
OS 2+ Jets
M_H = 180 GeV/c^2
Events / 0.05
NN Output

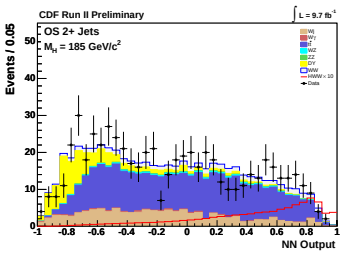
CDF Run II Preliminary
OS 2+ Jets
M_H = 185 GeV/c^2
Events / 0.05
NN Output

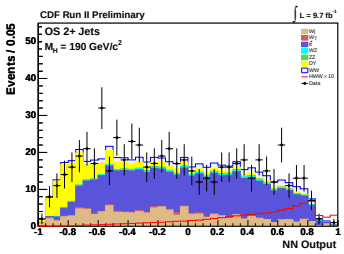
CDF Run II Preliminary
OS 2+ Jets
M_H = 190 GeV/c^2
Events / 0.05
NN Output

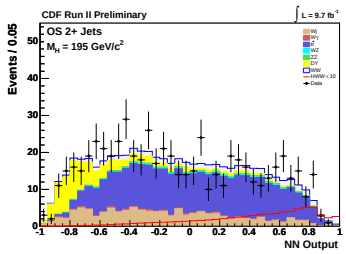
CDF Run II Preliminary
OS 2+ Jets
M_H = 195 GeV/c^2
Events / 0.05
NN Output

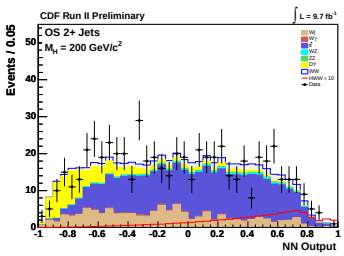
CDF Run II Preliminary
OS 2+ Jets
M_H = 200 GeV/c^2
Events / 0.05
NN Output

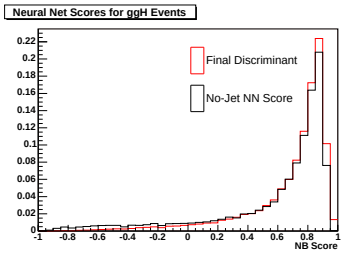

Figure 10.9 Comparison of neural network scores for gluon fusion events in the gluon fusion neural network and final discriminant, assessed as a shape systematic

fit. In the zero jet region, the WW and HWW likelihood ratios are included in the neural network discriminant.

10.3.2 Low m_{ll} Analysis

The low m_{ll} analysis targets the portion of the analysis with $m_{ll} < 16$ GeV. This is potentially significant due tothe spin correlation that results in collinear leptons. Only gluon fusion signal is considered, as other contributions are expected to be negligible. The base selection is used, with the m_{ll} threshold reversed. Events with two or more jets are not considered, and requirements are made to reject low-mass backgrounds: $\not\!\!E_{T,spec} > 4$ for $8.5 < m_{ll} < 10.5$ GeV (υ) and $m_{ll} < 6$ GeV (j/ψ). The dominant background in this region is $W\gamma$, validated in two control regions: low mass same-sign and low mass low $\not\!\!E_{T,spec}$. In the low mass same-sign region, which gives the purest sample of $W\gamma$, it is observed that this background needs to be corrected by a factor of 0.71, which is applied with associated uncertainties in the rest of the HWW and WW analyses. A neural network is trained in the same manner as the base regions.

10.3.3 Same-Sign Dilepton, 1+ Jets Analysis

This region targets associative production, where the associated vector boson and one of the Higgs decay products decay leptonically. Only associative production is considered in thsi region. Dominant backgrounds come from fake and charge misidentified leptons, and so

PHX, LBE and IsoCrkTrk leptons are not considered. Associative production tends to have less missing transverse energy, and Drell-Yan is not as large a background in the same-sign region, so $\not\!\!E_T$ is required. p_T for the second lepton is required to be > 20 GeV/c in order to reduce contamination from fake leptons. At least one jet is required. After selection, the dominant background is W+jets, validated in a zero jet control region. Drell-Yan is validated and scaled in a control region with the $\not\!\!E_T$ requirement reversed. A neural network is trained in the same manner as the base regions. The jet multiplicity is found to be the most significant discriminating variable, the signal being stronger in same-sign events with two or more jets.

10.3.4 Trilepton Analyses

The trilepton analysis also focuses on associative production, where three W bosons or one Z and one W decay leptonically. Events are separated into three categories: ZPeak1Jet and ZPeak2orMoreJets, for events where a dilepton pairing exists with an invariant mass withing ± 15 GeV of the Z, in order to isolate ZH events, and NoZPeak, for WH events. The WH region requires $\not\!\!E_T > 20$ GeV. ZH events generally have less $\not\!\!E_T$, so the requirement is kept to 10 GeV. Dominant backgrounds are WZ and fake lepton events. Control regions are defined with $10 < \not\!\!E_T < 20$ GeV for WH and zero jets for ZH. Neural networks are trained separately in all three regions. Individual jet kinematics are used in this region, including the E_T of the leading jet, and ΔR between the W lepton and leading jet in ZH events.

10.3.5 Hadronic τs

A final analysis category recovers signal from events in which a τ lepton decays hadronically. $\not\!\!E_T$ is required to be greater than 20 GeV, $m_{\tau l} > 20$ GeV, and $\Delta\phi(l\tau, \not\!\!E_T) > 1.5$ and $\Delta\phi(l, \tau) < 1.5$. Electron and muon events are analysed separately. Control samples are defined for W+jets by requiring $\Delta\phi(l, \tau > 2$, for multijet by requiring $\not\!\!E_T < 20$ GeV, and for $Z \to \tau\tau$ and reconstruction efficiencies by requiring $\not\!\!E_T < 20$ GeV and $\Delta\phi(l, \not\!\!E_T) < 0.5$. Final signal selection is accomplished by boosted decision trees which incorporate variables

for identifying hadronically-decaying τs, important for separating signal from W+jets background. Trilepton candidates in which one lepton is a hadronically decaying τ are also considered to maximize acceptance.

10.4 Systematic Uncertainties

We asses systematic uncertainties in three categories: theoretical uncertainty on the cross section, uncertainty on the luminosity, and uncertainties which affect our acceptance. Systematic uncertainties may affect both the normalization and shape of templates used in our analyses. However propogating the effects of shape uncertainties is CPU intensive, and so we only do so when the effect is significant. For this analysis we only found it necessary to apply shape systematics for Drell-Yan jet energy scale, WW PDF and JES variations, and the gluon fusion selection, discussed below. Rate systematics are determined individually for each jet bin, and summarized in Table 10.1-10.5 for the WW cross section measurement, and Table 10.6 for the $HWW + 2$ jet search. Statistics of simulated events are large enough to cause a negligible or sub-dominant effect on the result. However in cases where sufficient statistics could not be generated statistical uncertainties are applied to background distributions.

10.4.1 Cross Section

For background processes we take theoretical uncertainties on the cross-section, which are calculated to next-to-next-to-leading order for $t\bar{t}$[62], next-to-leading order for diboson processes[44][61] and Drell-Yan[73], and leading order for $W\gamma$[60]. For the Higgs processes, associative production is known to NNLO, with an uncertainty of less than 5%[74]. Vector boson fusion is known to NLO, with uncertainty estimated to be less than 10%[74]. Gluon fusion is the dominant contribution to the zero and one jet signal, and as a larger QCD process has larger theoretical uncertainties. Scale uncertainties are varied by a factor of two around M_H using the HNNLO program[75][76][77]. PDF uncertainties are determined with MSTW2008 NNLO PDFs[21].

10.4.2 Luminosity

The standard luminosity uncertainty of 5.9%[78] is assigned to all processes simulated with Monte Carlo. The uncertainty arises from operation and acceptance of the Cherenkov Luminosity Counter, and theoretical uncertainty in the inelastic $p\bar{p}$ cross section.

10.4.3 Lepton ID and Trigger

In the fit, we combine the lepton ID and trigger efficiencies in quadrature. The uncertainties arise from limited statistics in the samples used to measure the efficiency.

10.4.4 Acceptance Variations

Uncertainties are assigned to account for potential acceptance effects of higher order diagrams not used in MC generators. For WZ and ZZ, a 10% uncertainty is assigned based on a comparison of WW generated in Pythia and MC@NLO. A 10% uncertainty is assigned to $W\gamma$ due to the effect of higher order diagrams on extrapolating the normalization obtained in a low-m_{ll} same sign control region. For $t\bar{t}$ we assign an uncertainty of 2.7% due to QCD effects taken from the dilepton $t\bar{t}$ cross section measurement[63], which uses similar Monte Carlo simulation and lepton selection. For WW we do a more detailed acceptance study. We reweight the base sample by the p_T of the WW system, determined from the HEPG banks. To investigate the dependence on scale, Pythia samples are generated with fragmentation scales equal to the W energy and the energy of the total event. We reweight our base sample by the p_T of the WW system in order to determine the change in acceptance. Reweighting by p_T has some effect, particularly in high jet bins, and so we assign both a rate and a shape scale systematic uncertainty. Another source of acceptance uncertainty is due to our knowledge of the underlying parton distribution functions. We generate one million event samples for each of 40 CTEQ6[79] error eigenvectors and 20 α_s variations and reweighting our base sample by the p_T of the WW system. We find the change in acceptance due to α_s variations to be negligible. To evaluate the change in acceptance due to PDF variations we sum the change due to each variation in quadrature, considering positive and negative

variations separately. We take the larger variation as our uncertainty on the acceptance due to PDFs. Shape changes are small and so are not included. Higher order effects on the gluon fusion acceptance are evaluated by reweighting the Pythia samples to the p_T and rapidity distributions given by the HqT program[65][66]. Reweighting by p_T moves events between jet bins, and is referred to as (jets), while reweighting by rapidity moves leptons into or out of the acceptance, and is referred to as (leptons).

10.4.5 Btagging

As discussed in Section 7.4.1, the two or more jet signal region employs b-tagging to reduce ttbar background. For the cut value we chose, an uncertainty of 0.036 is assigned based on determination of the scale factor by a $t\bar{t}$ cross section measurement and an electron conversion method [71]. For SecVtx the uncertainty is 0.032. This only applies to the two or more jet region.

10.4.6 Jet Energy Scale

Uncertainty in Jet Energy Scale (JES) is determined in p_T balancing studies performed on $\gamma^*/Z+$ one jet events [80]. We vary the jet energy scale up and down by one standard deviation to determine the change in acceptance. As discussed in Section 9.1.1. Some shape discrepancy in modeling is observed in the Drell-Yan control region which is well covered by the JES systematic. For this reason we include the JES uncertainty as a shape systematic on Drell-Yan and WW production in the WW and $HWW + 2$ jets analyses.

10.5 WW Analysis

10.5.1 Maximum Likelihood Method

The signal cross sections are extracted from the neural net output shapes, estimated normalizations, and systematic uncertainties of signal and background via a binned maximum likelihood method.

0 Jets			CDF Run II Preliminary			$\int$ L = 9.7 fb^{-1}	
Uncertainty Source	WW	WZ	ZZ	$t\bar{t}$	DY	$W\gamma$	W+jet
Cross Section	6.0%	6.0%	6.0%	4.3%*			
Acceptance							
$\not\!\!E_T$ Modeling					19.0%*		
HO Diagrams		10.0%	10.0%			10.0%*	
$t\bar{t}$ QCD				2.7%			
Conversions						6.8%	
Scale	3.8%						
PDF Modeling	0.8%						
Jet Energy Scale	4.7%	6.4%	3.5%	26.8%	10.2%	3.5%	
Lepton ID Eff.	3.8%	3.8%	3.8%	3.8%			
Trigger Eff.	2.0%	2.0%	2.0%	2.0%			
Jet Fake Rate							17.2%
Luminosity	5.9%	5.9%	5.9%	5.9%			

* indicates uncorrelated systematic. (−) indicates anticorrelated systematic.

Table 10.1 Systematic uncertainties on the zero jet neural net inputs for the WW cross section measurement

1 jet, $15 < E_T < 25$ GeV			CDF Run II Preliminary			$\int \mathrm{L} = 9.7$ fb^{-1}	
Uncertainty Source	WW	WZ	ZZ	$t\bar{t}$	DY	$W\gamma$	W+jet
Cross Section	6.0%	6.0%	6.0%	4.3%*			
Acceptance							
$\not\!\!E_T$ Modeling					21.9%		
HO Diagrams		10.0%	10.0%			10.0%*	
$t\bar{t}$ QCD				2.7%			
Conversions						6.8%	
Scale	0.5%						
PDF Modeling	1.2%						
Jet Energy Scale	−9.6%	−1.0%	−4.6%	−12.9%	−8.7%	−9.5%	
Lepton ID Eff.	3.8%	3.8%	3.8%	3.8%			
Trigger Eff.	2.0%	2.0%	2.0%	2.0%			
Jet Fake Rate							18.9%
Luminosity	5.9%	5.9%	5.9%	5.9%			

* indicates uncorrelated systematic. (−) indicates anticorrelated systematic.

Table 10.2 Systematic uncertainties on the one jet low E_T neural net inputs for the WW cross section measurement

1 jet, $25 < E_T < 45$ GeV			CDF Run II Preliminary			$\int$ L = 9.7 fb^{-1}	
Uncertainty Source	WW	WZ	ZZ	$t\bar{t}$	DY	$W\gamma$	W+jet
Cross Section	6.0%	6.0%	6.0%	4.3%*			
Acceptance							
$\not\!\!E_T$ Modeling					22.1%		
HO Diagrams		10.0%	10.0%			10.0%*	
$t\bar{t}$ QCD				2.7%			
Conversions						6.8%	
Scale	−5.6%						
PDF Modeling	1.2%						
Jet Energy Scale	−5.8%	−1.0%	−4.6%	−12.9%	−22.9%	−9.5%	
Lepton ID Eff.	3.8%	3.8%	3.8%	3.8%			
Trigger Eff.	2.0%	2.0%	2.0%	2.0%			
Jet Fake Rate							18.9%
Luminosity	5.9%	5.9%	5.9%	5.9%			

* indicates uncorrelated systematic. (−) indicates anticorrelated systematic.

Table 10.3 Systematic uncertainties on the one jet mid E_T neural net inputs for the WW cross section measurement

1 jet, $E_T > 45$ GeV			CDF Run II Preliminary			$\int$ L = 9.7 fb^{-1}	
Uncertainty Source	WW	WZ	ZZ	$t\bar{t}$	DY	$W\gamma$	W+jet
Cross Section	6.0%	6.0%	6.0%	4.3%*			
Acceptance							
$\not\!\!E_T$ Modeling					23.0%		
HO Diagrams		10.0%	10.0%			10.0%*	
$t\bar{t}$ QCD				2.7%			
Conversions						6.8%	
Scale	−23.7%						
PDF Modeling	1.3%						
Jet Energy Scale	−2.7%	−1.0%	−4.6%	−12.9%	3.7%	−9.5%	
Lepton ID Eff.	3.8%	3.8%	3.8%	3.8%			
Trigger Eff.	2.0%	2.0%	2.0%	2.0%			
Jet Fake Rate							18.9%
Luminosity	5.9%	5.9%	5.9%	5.9%			

* indicates uncorrelated systematic. (−) indicates anticorrelated systematic.

Table 10.4 Systematic uncertainties on the one jet high E_T neural net inputs for the WW cross section measurement

2 or More Jets			CDF Run II Preliminary			$\int$ L = 9.7 fb^{-1}	
Uncertainty Source	WW	WZ	ZZ	$t\bar{t}$	DY	$W\gamma$	W+jet
Cross Section	6.0%	6.0%	6.0%	4.3%*	5.0%*		
Acceptance							
$\not\!\!E_T$ Modeling					26.0%*		
HO Diagrams		10.0%	10.0%			10.0%*	
$t\bar{t}$ QCD				2.7%			
Conversions						6.8%	
Scale	−13.0%						
PDF Modeling	1.8%						
Jet Energy Scale	−21.5%	−13.2%	−13.3%	−1.7%	−28.7%	−22.0%	
$b-$tag veto				3.6%			
Lepton ID Eff.	3.8%	3.8%	3.8%	3.8%	3.8%		
Trigger Eff.	2.0%	2.0%	2.0%	2.0%	2.0%		
Jet Fake Rate							19.0%
Luminosity	5.9%	5.9%	5.9%	5.9%	5.9%		

* indicates uncorrelated systematic. (−) indicates anticorrelated systematic.

Table 10.5 Systematic uncertainties on the two or more jet neural net inputs for the WW cross section measurement

OS 2+Jets			CDF Run II Preliminary			$\int$ L = 9.7 fb^{-1}	
Uncertainty Source	WW	WZ	ZZ	$t\bar{t}$	DY	$W\gamma$	W+jet
Cross Section	*6.0%*	*6.0%*	*6.0%*	7.0%			
Acceptance							
Scale (jets)	*-8.2%*s						
PDF Model (leptons)							
PDF Model (jets)	*4.2%*						
HO Diagrams		*10.0%*	*10.0%*	10.0%		10.0%	
$\not\!\!E_T$ Modeling					26.0%		
Conversions						6.8%	
Jet Fake Rates							19.0%
Jet Energy Scale	*-20.5%*	*-13.2%*	*-13.3%*	*-1.7%*	*-32.7%*	*-22.0%*	
b-tag Veto				3.6%			
Lepton ID Eff.	*3.8%*	*3.8%*	*3.8%*	*3.8%*	*3.8%*		
Trigger Eff.	*2.0%*	*2.0%*	*2.0%*	*2.0%*	*2.0%*		
Luminosity	*5.9%*	*5.9%*	*5.9%*	*5.9%*	*5.9%*		

Table 10.6 Systematic uncertainties on the $HWW + 2$ or more jet neural net inputs for the $HWW + 2$ or more jets search

OS 2+Jets		CDF Run II Preliminary	$\int$ L = 9.7 fb^{-1}	
Uncertainty Source	$gg \to H$	WH	ZH	VBF
Cross Section				
ScaleInclusive	0.0%			
Scale1+Jets	0.0%			
Scale2+Jets	33.0%			
PDF Model	29.7%			
Total		**5.0%**	**5.0%**	10.0%
Acceptance				
PDF Model (leptons)	4.8%			
PDF Model (jets)	-12.3%			
HO Diagrams		**10.0%**	**10.0%**	**10.0%**
$\not\!\!E_T$ Modeling				
Jet Energy Scale	*-15.1%*	*-4.0%*	*-2.5%*	*-3.8%*
Lepton ID Eff.	*3.8%*	*3.8%*	*3.8%*	*3.8%*
Trigger Eff.	*2.0%*	*2.0%*	*2.0%*	*2.0%*
Luminosity	*5.9%*	*5.9%*	*5.9%*	*5.9%*

Table 10.7 Systematic uncertainties on the $HWW + 2$ or more jet neural net inputs for the HWW_2 or more jets search continued

The best fit is found by maximizing the likelihood function, a product of Poisson probabilities for each neural net bin and Gaussian distributions for each systematic S_c.

$$\mathcal{L} = \left(\prod_i \frac{\mu_i^{n_i} e^{-\mu_i}}{n_i!} \right) \cdot \prod_c e^{\frac{S_c^2}{2}} \tag{10.3}$$

n_i is the number of data events in the i-th bin. μ_i, the total expectation in the i-th bin, is given by

$$\mu_i = \sum_k \alpha_k [\prod_c (1 + \{_k^c S_c)] (N_k^{Exp})_i \tag{10.4}$$

For a process k and systematic S_c, $\{_k^c$ is the fractional uncertainty assigned to that systematic, as shown in Tables 10.1- 10.5. $(N_k^{Exp})_i$ is the expected number of events from process k in bin i. Where applicable, shape systematics are included by evaluating the change in $(N_k^{Exp})_i$ according to the formula[81]

$$(N_k^{Exp})_i = N_{ki}^0 + S_c \frac{N_{ki}^+ - N_{ki}^-}{2} \tag{10.5}$$

α_k is a normalization parameter that is fixed for all processes except the signal.

The MINUIT [82] program varies the nuisance parameters and normalization to maximize the likelihood function. In practice it minimizes the negative log likelihood, which is equivalent to maximizing the likelihood. MINOS is used to extract the asymmetric errors on the minimization, which are used in the cross section measurement.

In the WW cross section measurement, we fit to all jet and leading jet E_T bins simultaneously. α_{WW} is allowed to float independently in each jet bin in order to extract the differential cross section according to the formula

$$\sigma_{WW}^{measured} = \alpha_{WW} \cdot \sigma_{WW}^{NLO} \tag{10.6}$$

Region	Expected Uncertainty (+)	Expected Uncertainty (-)
0 Jet	0.13	0.11
1 Jet, Low E_T	0.19	0.17
1 Jet, Mid E_T	0.25	0.22
1 Jet, High E_T	0.51	0.37
2+Jets	0.45	0.35

Table 10.8 Uncertainties from pseudoexperiment distributions

10.5.2 Pseudoexperiments

In order to quantify our expectations we generate arrays of pseudoexperiments. Minimization is done for each pseudo-experiment exactly as for data. The procedure for generating pseudo-experiments is as follows

- Construct an array of numbers g_c with a Gaussian distribution
- For each systematic a Gaussian fluctuation is applied to (N_k^{Exp}) using g_c for the value of the systematic

$$G_k = N_k^{Exp} \prod_c (1 + \{_k^c g_c) \tag{10.7}$$

- G_k is then used as the mean of a poisson distribution, from which a number of events P_k is drawn.
- P_k events are drawn from the neural net template for process k, with probability according to the template distribution.

Expected uncertainties for the WW analysis are listed in Table 10.8, and the likelihood results are shown in Figure 10.10.

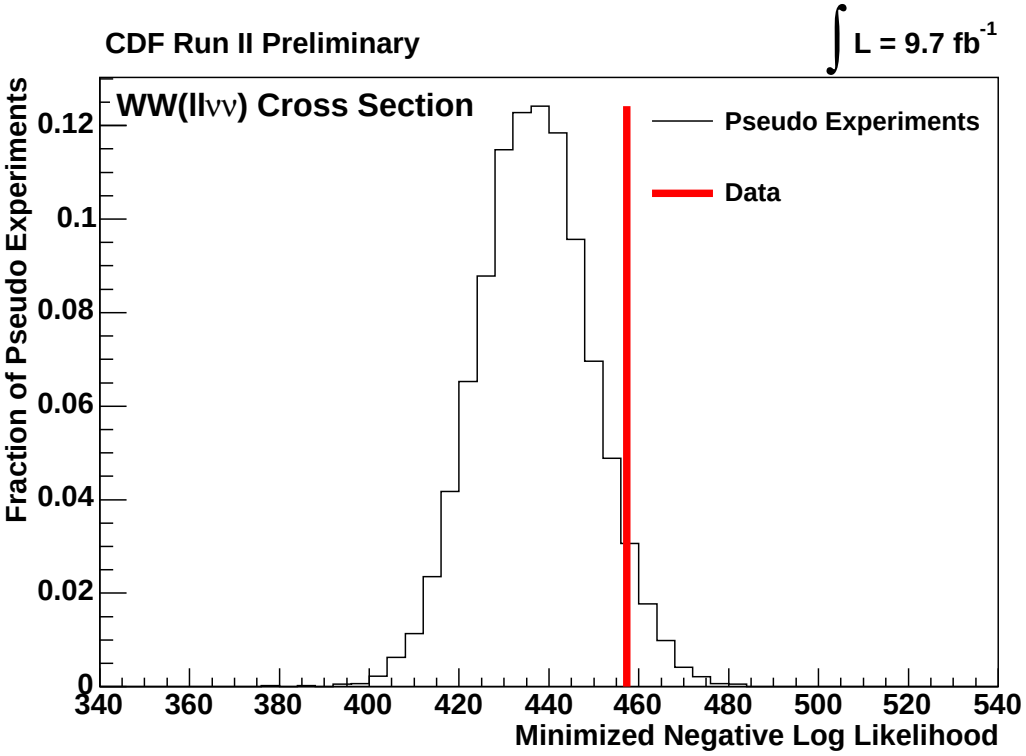

Figure 10.10 Distribution of minimized negative log likelihood values for WW pseudoexperiments.

10.5.3 Unfolding

Jet E_T is distorted by detector effects such as finite resolution and limited acceptance. In addition to changing the measured E_T, this can also affect jet counting when a jet slips under or over threshold. This does not affect the measurement of an inclusive cross section, as in the Higgs result. However in order to compare our differential WW cross section with the theoretical prediction given by the Monte Carlo programs we unfold the observed results back to the level of hadron clustered jets. We cluster jets in the Alpgen Monte Carlo with a cone-based algorithm, and compare them to fully reconstructed jets. Half of the sample is used to create a response matrix M_{ij} that maps the hadron-level jet distribution (H_j) to the reconstructed jet distribution (J_i)

$$J_i = \sum_j M_{ij} H_j \tag{10.8}$$

Events are binned by jet multiplicity, and 1 jet events are further separated into three bins: $15 - 25$ GeV, $25 - 45$ GeV, and > 45 GeV. Each entry is the number of events with reconstructed jet(s) in bin i and hadron-level jet(s) in bin j.

Had. Jets	0	1, Low E_T	1, Mid E_T	1, High E_T	2+
2+	0.554 ± 0.039	1.987 ± 0.052	1.920 ± 0.045	1.269 ± 0.035	14.620 ± 0.063
1, High E_T	0.921 ± 0.089	0.105 ± 0.024	1.343 ± 0.058	12.993 ± 0.179	1.342 ± 0.040
1, Mid E_T	3.557 ± 0.162	2.734 ± 0.085	21.226 ± 0.232	2.257 ± 0.078	2.298 ± 0.055
1, Low E_T	13.800 ± 0.259	26.322 ± 0.280	8.046 ± 0.151	0.002 ± 0.0001	2.992 ± 0.071
0	395.483 ± 2.004	21.920 ± 0.374	0.370 ± 0.039	3e-5 $\pm$ 3e-5	1.211 ± 0.076

Reconstructed Jets

Table 10.9 Unfolding Matrix with uncertainties

We unfold our results with RooUnfold[83] using a Bayesian iterative method. In this method the result is regularized by the number of iterations. The other half of the Monte Carlo is used to verify that the unfolding reproduces the hadronic result, it is found to do so best with a choice of two iterations.

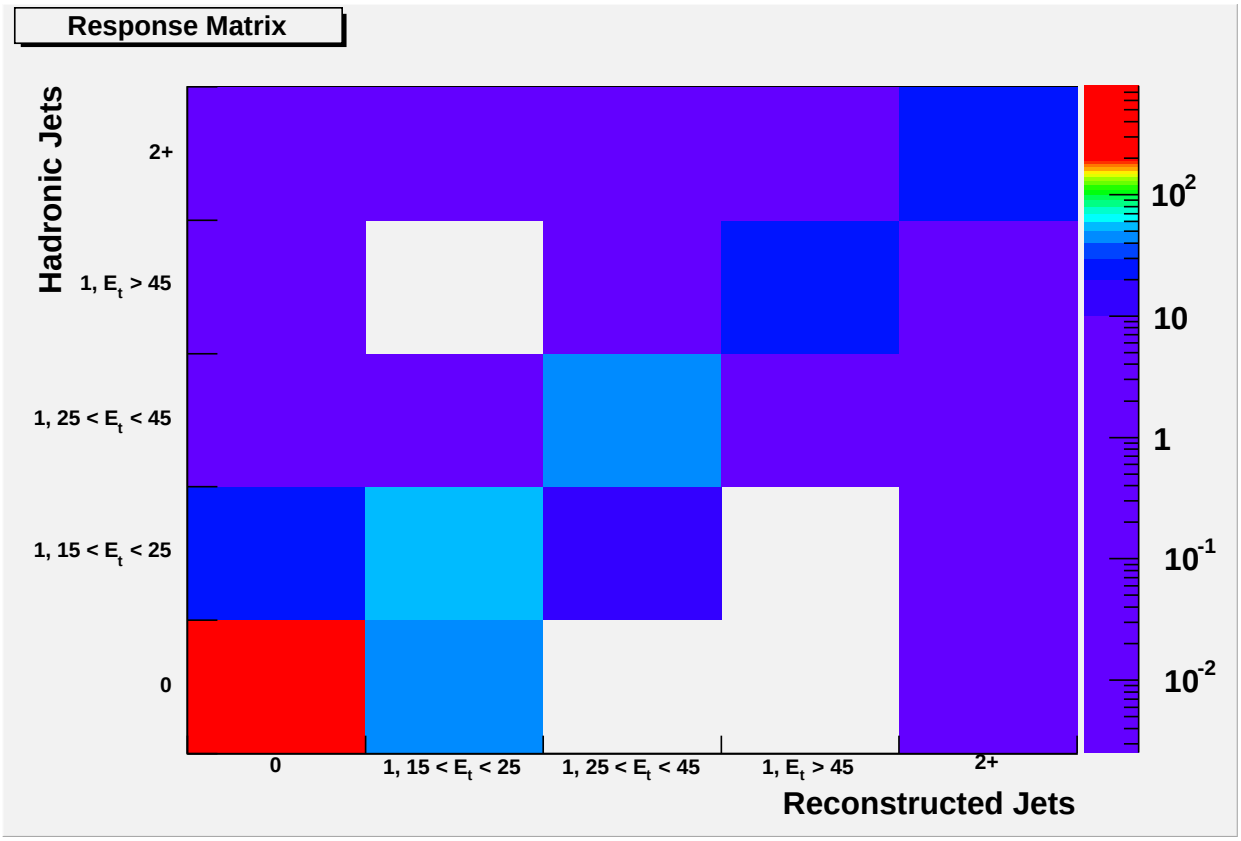

Figure 10.11 Response Matrix: Colors indicated numbers of events in each bin.

10.6 HWW Analysis

Limits on the Higgs boson production cross section are set by the maximum likelihood method discussed in Section 10.5.1. In the Higgs search, we fit to all subchannels simultaneously. However in order to exclude or observe evidence for a Higgs boson, the scale parameter (here referred to as R) is required to be constant across all subchannels. A 95% confidence level limit on the Higgs cross section is obtained from

$$0.95 = \frac{\int_0^{R_{limit}} L'(data|Rs, b)\pi(R)}{\int_0^{\inf} L'(data|Rs, b)\pi(R)} \tag{10.9}$$

Where s is the signal, R is a scale parameter, b is background, and $\pi(R)$ is a uniform prior distribution. The nuisance parameters correctly account for correlations between systematics across subchannels in both analyses. Limits are set on Higgs production by generating an ensemble of background only pseudoexperiments following the method in Section 10.5.2, both for the two or more jets subchannel, and the combination. These limits can be seen in the expected exclusion in Chapter 12. The migration of events between bins will not affect the inclusive cross section beyond the systematic uncertainties that have already been applied to account for global acceptance effects. Therefore unfolding is not necessary in this analysis.

Chapter 11

WW Cross Section Results

The results of the WW fit can be seen in Table 11.1 and Table 11.2. The α_{WW} values multiply the theoretical predicted cross section, with errors shown. The fit values for the nuisance parameters indicate modification of the initial value by the fit as a multiple of standard deviations, where the percentage effect of one standard deviation is given in Tables 10.1- 10.5. Neural network outputs before and after fitting are shown in Figures 11.1- 11.3. In the zero jet region, an excess is observed, but it is confined to the background dominated region. As a result the W+jets and $W\gamma$ yields are increased by the fit. In the one jet region, the Drell-Yan yield is reduced, but the uncorrelated $\not\!\!E_T$ modeling means this does not affect the other regions. In the two or more jet region, the $t\bar{t}$ yield is sightly reduced. In all cases, the changes in the background normalization are consistent with the uncertainties on those backgrounds. We measure an inclusive cross section of $14.0 \pm 0.6(stat)^{+1.2}_{-1.0}(syst) \pm 0.8(lumi)$ pb, consistent with Standard Model predictions. The differential predictions are shown in Table 11 and Figure 11.4. We observe agreement in the differential measurement as well. While some discrepancy may be observed in the two or more jet bin, agreement is still within 1.5 standard deviations.

Parameter	Fit Value	+ Error	- Error
α_{WW}(0J)	1.20	0.13	0.12
α_{WW}(1J, Low E_T)	1.06	0.21	0.18
α_{WW}(1J, Mid E_T)	1.40	0.31	0.28
α_{WW}(1J, High E_T)	1.32	0.65	0.48
α_{WW}(2+J)	1.94	0.72	0.54

Table 11.1 Fit values for signal normalization parameters. α_{WW} multiplies the number of WW events in the appropriate bin, with errors in the positive and negative direction.

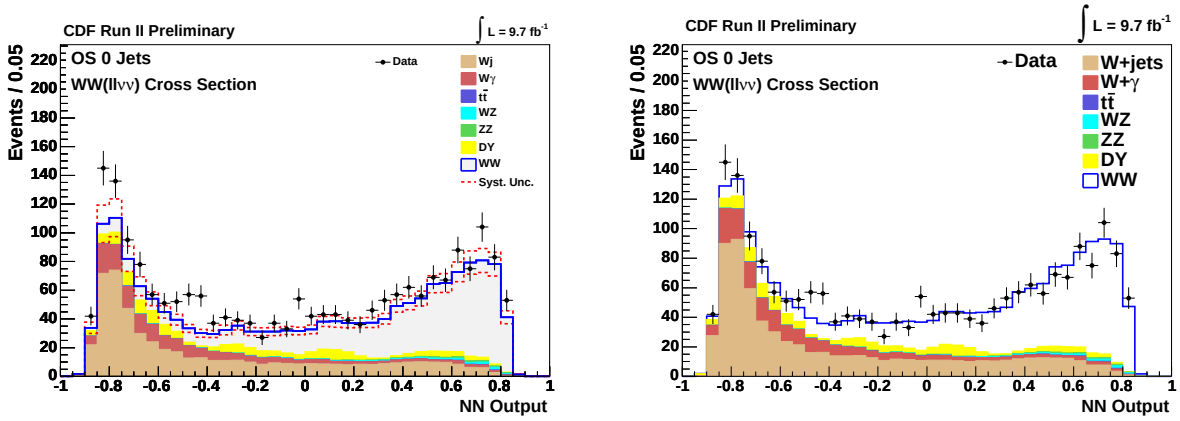

Figure 11.1 Comparison of templates before and after fitting in the 0 jet bin.

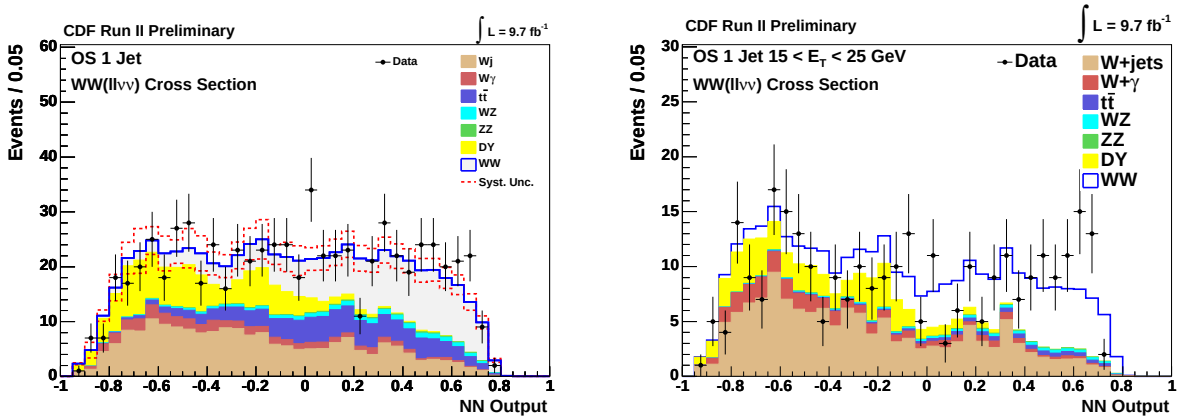

Figure 11.2 Comparison of templates before and after fitting in the 1 jet bin.

Parameter	Fit Value	+ Constraint	- Constraint
MetModel0	0.02	0.92	0.91
MetModel1	−1.21	0.69	0.67
MetModel2	−0.74	1.02	1.04
WgamScale	0.69	0.98	0.98
WgamAcc	0.97	0.97	0.97
DiboAcc	0.00	1.00	1.00
TopAcc	−0.19	0.99	0.99
TrigID	−0.59	0.97	0.97
WW Scale	0.36	0.94	0.92
Fake	1.48	0.45	0.45
Lumi	−0.56	0.94	0.94
BTagVeto	−0.21	0.98	0.98
XS_Diboson	0.00	1.00	1.00
XS_ttbar	−0.30	0.97	0.97
XS_DY	−0.12	1.00	1.00
JES	0.29	0.73	0.62
DY Stat	−0.99	0.61	0.37

Table 11.2 Fit values for nuisance parameters. Fit values are listed in standard deviations offset from prediction. Constraints indicate a multiplicative constraint on the systematic values in Tables 10.1- 10.5

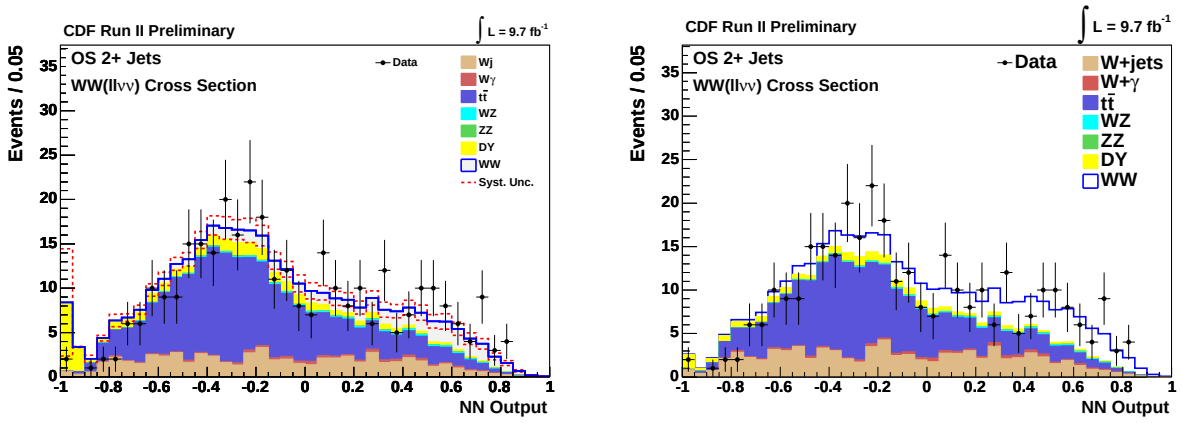

Figure 11.3 Comparison of templates before and after fitting in the 2 or more jet bin.

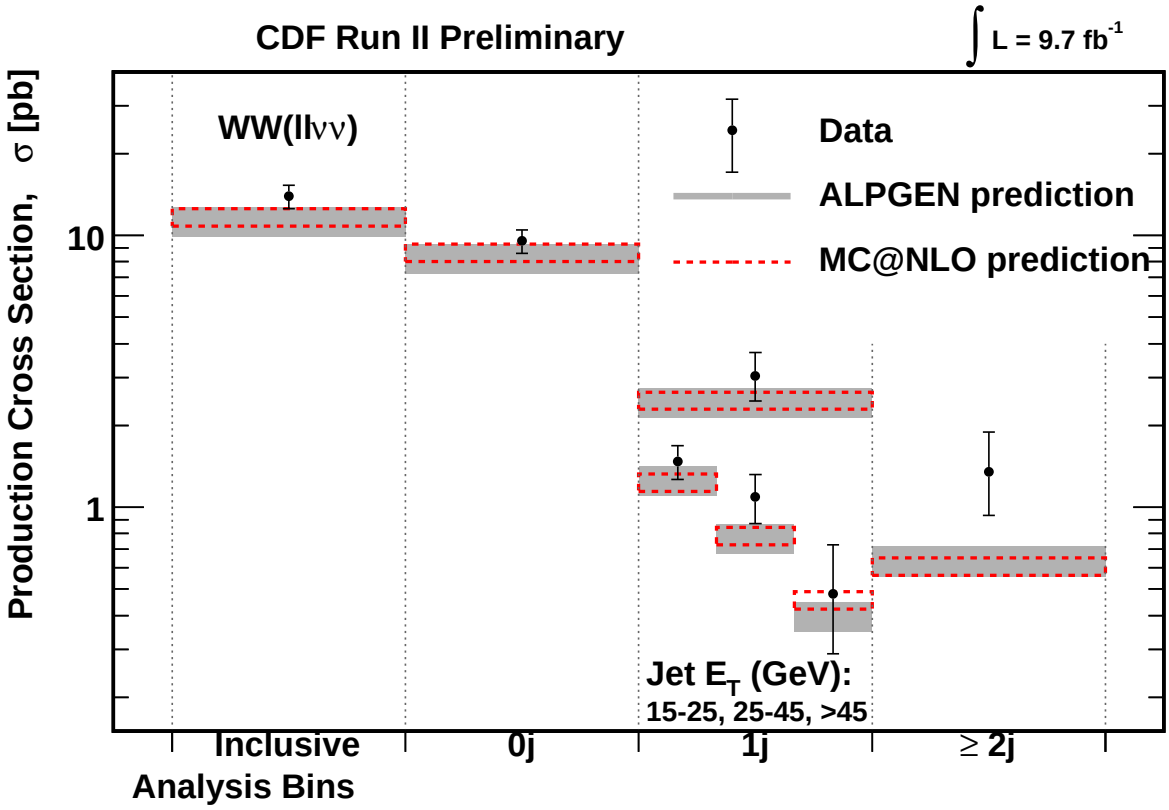

Figure 11.4 WW cross section measurement.

WW($ll\nu\nu$) Cross Section		CDF Run II Preliminary			$\int L = 9.7$ fb^{-1}	
	σ(pb)	Uncertainty(pb)			σ(pb)	
Jet Bin	Measured	Stat.	Syst.	Lumi.	Alpgen	MC@NLO
Inclusive	14.0	± 0.6	$^{+1.2}_{-1.0}$	± 0.8	11.3 ± 1.4	11.7 ± 0.9
0 Jets	9.57	± 0.40	$^{+0.82}_{-0.68}$	± 0.56	8.24 ± 1.04	8.62 ± 0.63
1 Jet Inclusive	3.04	± 0.46	$^{+0.48}_{-0.32}$	± 0.18	2.43 ± 0.31	2.47 ± 0.18
1 jet, $15 < E_T < 25$ GeV	1.47	± 0.17	$^{+0.13}_{-0.09}$	± 0.09	1.26 ± 0.16	1.18 ± 0.09
1 jet, $25 < E_T < 45$ GeV	1.09	± 0.18	$^{+0.14}_{-0.11}$	± 0.06	0.77 ± 0.10	0.79 ± 0.06
1 jet, $E_T > 45$ GeV	0.48	± 0.15	$^{+0.19}_{-0.11}$	± 0.03	0.40 ± 0.05	0.46 ± 0.03
2 or More jets	1.35	± 0.30	$^{+0.45}_{-0.28}$	± 0.08	0.64 ± 0.08	0.61 ± 0.05

Chapter 12

Higgs Search Results

In the Higgs search, $WW+2$ or more jets final state, we set limits on the Higgs production cross section. Expected and observed limits are shown for 5 GeV increments in Table 12.1 and Figure 12.1. If the Standard Model prediction of the signal strength for a value of m_H is larger than the observed 95% confidence level upper limit, that mass is excluded at at least the 95% confidence level. We set limits of $17.03 \times \sigma_{SM}$ at 125 GeV and $2.42 \times \sigma_{SM}$ at 160 GeV. Combined limits are set by the same method, including all subchannels discussed in Section 10.3. These limits are shown in Table 12.2 and Figure 12.2. The multiplicative factor times the Standard Model cross section can be used as a metric of the strength of the search. Limits and combinations of limits tend to improve according to the root of the increase in statistics, such that a combination of four searches, each with independent sensitivity of two times the SM cross section would have sensitivity to the SM cross section. In the combined limit, the two or more jet region is the second most sensitive subchannel, due to the ability to target extra signal from associative production and vector boson fusion. The combined high-mass Higgs search excludes a mass range of $149 - 172$ GeV, and sets a limit of $2.98 \times \sigma_{SM}$ at 125 GeV. The full CDF Higgs search [84] combines four significant channels: 3 from $H \to b\bar{b}$ and the $H \to WW$ search. An expected limit of $1.39 \times \sigma_{SM}$ is set. This is combined with results from the D0 experiment in the Tevatron Higgs search [85], reaching sensitivity to the Standard Model Higgs production cross section. At 125 GeV, the experiments collectively observe an excess of events with a significance of slightly more than three standard deviations. This result is dominated by the $H \to b\bar{b}$ channels which

also achieve significance above three standard deviations, demonstrating tree level coupling of the Higgs boson to a fermion. This observation is consistent with the observation of a Higgs boson reported by the ATLAS [50] and CMS [51] collaborations in decays involving vector bosons.

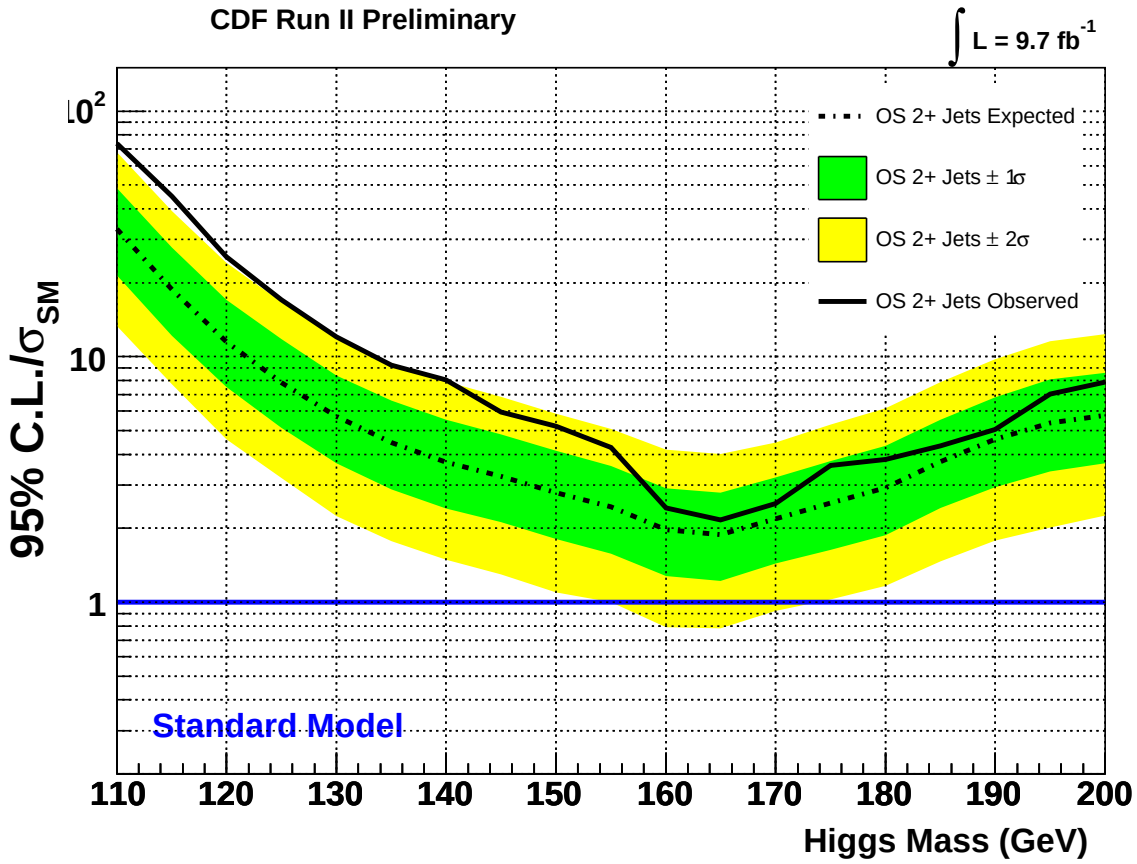

Figure 12.1 $HWW + 2$ or more jet limits.

OS 2+ Jets	110	115	120	125	130	135	140	145	150	155
$-2\sigma/\sigma_{SM}$	13.32	7.72	4.62	3.20	2.24	1.77	1.49	1.29	1.10	1.00
$-1\sigma/\sigma_{SM}$	21.38	12.17	7.52	5.14	3.67	2.88	2.41	2.12	1.81	1.58
Median/$\sigma_{\mathbf{SM}}$	**33.04**	**18.78**	**11.50**	**7.83**	**5.70**	**4.46**	**3.71**	**3.26**	**2.79**	**2.44**
$+1\sigma/\sigma_{SM}$	48.45	27.85	17.06	11.78	8.39	6.61	5.52	4.82	4.14	3.59
$+2\sigma/\sigma_{SM}$	68.01	39.18	24.16	16.71	11.89	9.42	7.91	6.88	5.86	5.08
Observed/$\sigma_{\mathbf{SM}}$	**73.96**	**44.96**	**25.48**	**17.03**	**12.04**	**9.24**	**8.03**	**5.94**	**5.21**	**4.28**
OS 2+ Jets	160	165	170	175	180	185	190	195	200	
$-2\sigma/\sigma_{SM}$	0.79	0.78	0.92	1.03	1.16	1.47	1.78	2.01	2.26	
$-1\sigma/\sigma_{SM}$	1.28	1.22	1.43	1.63	1.88	2.41	2.93	3.41	3.67	
Median/$\sigma_{\mathbf{SM}}$	**1.97**	**1.89**	**2.19**	**2.54**	**2.92**	**3.73**	**4.61**	**5.37**	**5.78**	
$+1\sigma/\sigma_{SM}$	2.91	2.79	3.21	3.76	4.33	5.54	6.84	8.06	8.60	
$+2\sigma/\sigma_{SM}$	4.17	4.01	4.47	5.29	6.17	7.89	9.76	11.52	12.37	
Observed/$\sigma_{\mathbf{SM}}$	**2.42**	**2.16**	**2.52**	**3.60**	**3.81**	**4.34**	**5.04**	**7.03**	**7.89**	

Table 12.1 $HWW + 2$ or more jet limits

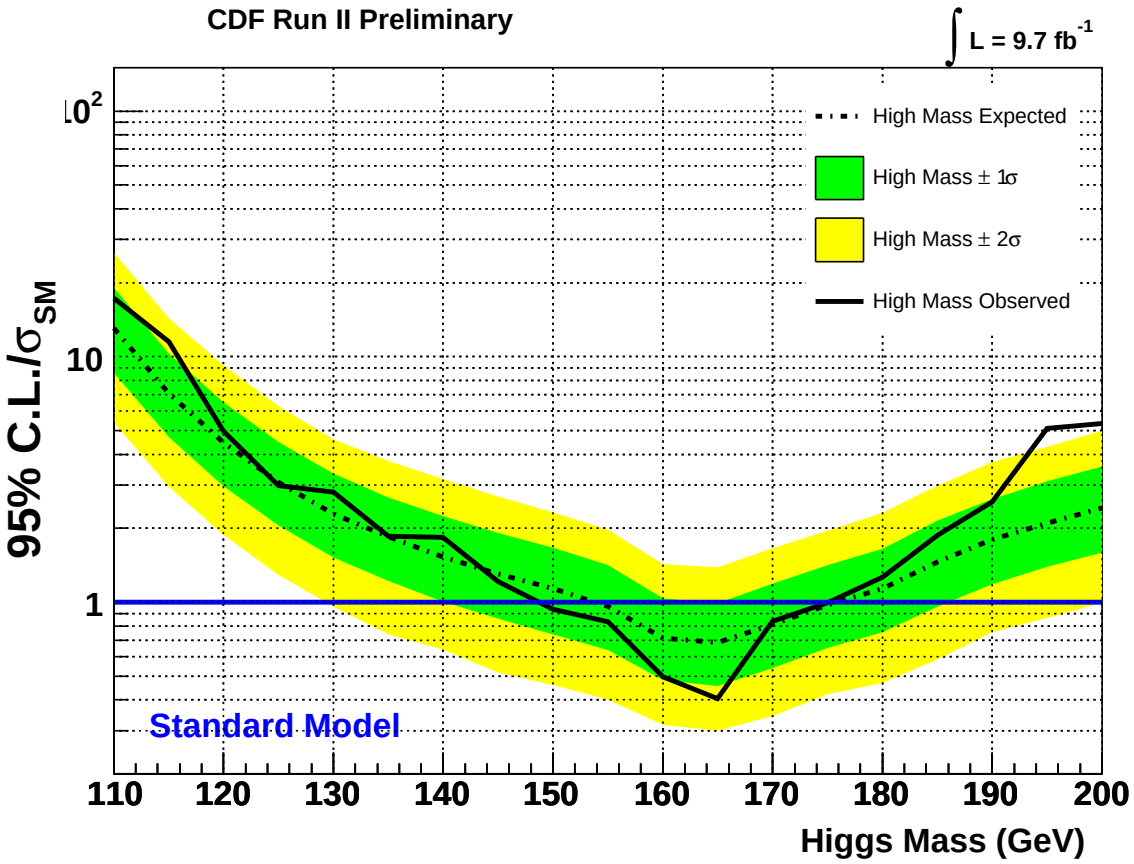

Figure 12.2 HWW combination limits.

High Mass	110	115	120	125	130	135	140	145	150	155
$-2\sigma/\sigma_{SM}$	5.39	2.95	1.88	1.29	0.96	0.74	0.64	0.52	0.46	0.40
$-1\sigma/\sigma_{SM}$	8.61	4.71	2.97	2.05	1.52	1.22	1.01	0.86	0.74	0.64
Median/$\sigma_{\mathbf{SM}}$	**13.06**	**7.07**	**4.47**	**3.08**	**2.29**	**1.85**	**1.53**	**1.31**	**1.13**	**0.96**
$+1\sigma/\sigma_{SM}$	19.03	10.25	6.51	4.49	3.34	2.67	2.24	1.91	1.66	1.41
$+2\sigma/\sigma_{SM}$	26.57	14.32	9.21	6.28	4.62	3.75	3.17	2.69	2.32	1.97
Observed/$\sigma_{\mathbf{SM}}$	**17.28**	**11.52**	**4.96**	**2.98**	**2.81**	**1.85**	**1.84**	**1.22**	**0.94**	**0.83**
High Mass	160	165	170	175	180	185	190	195	200	
$-2\sigma/\sigma_{SM}$	0.32	0.30	0.34	0.42	0.47	0.58	0.75	0.86	1.00	
$-1\sigma/\sigma_{SM}$	0.48	0.46	0.54	0.65	0.75	0.96	1.18	1.40	1.59	
Median/$\sigma_{\mathbf{SM}}$	**0.71**	**0.69**	**0.81**	**0.97**	**1.13**	**1.46**	**1.80**	**2.10**	**2.42**	
$+1\sigma/\sigma_{SM}$	1.03	0.99	1.19	1.41	1.65	2.15	2.63	3.10	3.57	
$+2\sigma/\sigma_{SM}$	1.43	1.39	1.65	1.95	2.31	2.99	3.71	4.30	4.99	
Observed/$\sigma_{\mathbf{SM}}$	**0.50**	**0.40**	**0.84**	**0.99**	**1.26**	**1.87**	**2.56**	**5.10**	**5.33**	

Table 12.2 HWW combination limits.

Chapter 13

Conclusion

We have presented a differential measurement of the WW cross section in event where both W bosons decay leptonically, using the full CDF 9.7fb^{-1} dataset. Events with two oppositely charged leptons and substantial missing transverse energy are selected and separated by jet multiplicity and transverse energy. Signal separation is enhanced by the use of neural networks, and the cross section is measured by a maximum likelihood fit to the neural network output templates. The cross section is measured to be $14.0 \pm 0.6(stat)^{+1.2}_{-1.0}(syst) \pm 0.8(lumi)$ pb, and both inclusive and differential results are consistent with Standard Model predictions. Good agreement with leading techniques for the simulation of events with multiple vector bosons and multiple jets is observed, with differences between NLO and fixed order generation negligible compared to theoretical and experiment uncertainties. These results indicate the suitability of both techniques for simulated diboson plus jets backgrounds in Higgs searches, other new physics searches, or studies of new phenomena in multiple vector boson production such as longitudinal vector boson scattering which includes scattering by a Higgs boson. Searches of this type are a key element of the future physics program of the LHC. This result is unfolded, enabling comparison to any theoretical prediction at the hadronic level. It is the first jet-differential measurement in a massive diboson state, made possible by the reduced $t\bar{t}$ background of the Tevatron relative to the LHC.

We have additionally presented a search for the Higgs boson in the WW with two or more jets final state. Event selection is largely the same as the WW measurement, requiring two oppositely charged leptons, substantially missing transverse energy, and two or more

jets. Additional sensitivity has been achieved by the use of individual jet kinematics to take advantage of characteristic features of associative production and vector boson fusion. This analysis has the second strongest sensitivity in the high-mass Higgs combination, which excludes a mass region from $149 - 172$ GeV and sets a limit of $2.98 \times \sigma_{SM}$ at 125 GeV, and contributes to the sensitivity of the search that has demonstrated evidence for Higgs boson production in proton-antiproton collisions consistent with the Higgs boson that has been observed at the LHC experiments in proton-proton collisions.

LIST OF REFERENCES

[1] R. P. Feynman. *Physical Review*, 80(440), 1950.

[2] S. Tomonaga. *Progress of Theoretical Physics*, 1(2), 1946.

[3] J. Schwinger. *Physical Review*, 73(416), 1947.

[4] S. Glashow. *Nuclear Physics*, 22(4), 1961.

[5] S. Weinberg. *Phys. Rev. Lett.*, 19(1264), 1967.

[6] A. Salam. *Conf. Proc.*, C680519(367), 1968.

[7] F. Englert and R. Brout. *Phys. Rev. Lett.*, 13(321), 1964.

[8] P. W. Higgs. *Phys. Rev. Lett.*, 13(508), 1964.

[9] C. R. Hagen G. S. Guralnik and T. W. B. Kibble. *Phys. Rev. Lett.*, 13(585), 1964.

[10] J. M. Campbell and R. K. Ellis. Update on vector boson pair production at hadron colliders. *Phys. Rev. D*, 60(113006), 1999.

[11] S. Frixione and B. R. Webber. *JHEP*, 0206(029), 2002.

[12] L. Lonnblad T. Sjostrand and S. Mrenna, 2001. hep-ph/0108264.

[13] F. Piccinini R. Pittau A. D. Polosa M. L. Mangano, M. Moretti. Alpgen, a generator for hard multiparton processes in hadronic collisions. *JHEP*, 0307(001), 2003.

[14] C. Anastasiou and K. Melnikov. *Nucl. Phys. B*, 6446(220), 2002.

[15] S. Dawson. *Nucl. Phys. B*, 359(283), 1991.

[16] M. Spira A. Djouadi and P. M. Zerwas. *Phys. Lett. B*, 264(440), 1991.

[17] D. Graudenx M. Spira, A. Djouadi and P. M. Zerwas. *Nucl. Phys. B*, 453(17), 1995.

[18] M. E. Machacek H. M. Georgi, S. L. Glashow and D. V. Nanopoulos. *Phys. Rev. Lett.*, 40(692), 1978.

[19] D. de Florian and M. Grazzini. *Phys. Lett. B*, 674(291), 2009.

[20] R. Boughezal C. Anastasiou and F. Petriello. *J. High Energy Phys.*, 04(003), 2009.

[21] R. S. Thorne A. D. Martin, W. J. Stirling and G. Watt, 2009. 0901.0002/hep-ph.

[22] S. Moch and A. Vogt. *Phys. Lett. B*, 631(48), 2005.

[23] K. A. Assamagan et al.(Higgs Working Group), 2012. arXiv:hep-ph/0406152.

[24] S.-O. Moch P. Bolzoni, F. Maltoni and M. Zaro. *Phys. Rev. Lett.*, 105(011801), 2010.

[25] E. L. Berger and J. M. Campbell. *Phys. Rev. D*, 70(073011), 2008.

[26] J. Baglio and A. Djouadi. *J. High Energy Phys.*, 10(064), 2010.

[27] M. Grazzini G. Ferrera and F. Tramontano. *Phys. Rev. Lett.*, 107(152003), 2011.

[28] A. Djouadi O. Brein and R. Harlander. *Phys. Lett. B*, 579(149), 2004.

[29] S. Dittmaier M. L. Ciccolini and M. Kramer. *Phys. Rev. D*, 68(011801), 2003.

[30] G. Amison et al. (UA1 Collaboration). *Physics Letters B*, 122(1), 1983.

[31] M. Banner et al. (UA2 Collaboration). *Physics Letters B*, 122(5-6), 1983.

[32] et al. ALEPH Collaboration, R. Barate. *Phys. Lett. B*, 484(3-4), 2000.

[33] P. Abreu et al. DELPHI Collaboration. *Phys. Lett. B*, 479(1-3), 2000.

[34] L3 M. Acciarri et al. *Phys. Lett. B*, 496(1-2), 2000.

[35] G. Abbiendi et al. OPAL Collaboration. *Phys. Lett. B*, 493(3-4), 2000.

[36] F. Abe et al. (CDF Collaboration). Evidence for w^+w^- production in $p\bar{p}$ collisions at $\sqrt{s} = 1.8$ tev. *Phys. Rev. Lett.*, 78(4536), 1997.

[37] CDF Collaboration. Measurement of the w^+w^- production cross section and search for anomalous $ww\gamma$ and wwz couplings in $p\bar{p}$ collisions at $\sqrt{s} = 1.96$ tev. *Physical Review Letters*, 104(201801), 2010.

[38] D0 Collaboration. Search for higgs boson production in oppositely charged dilepton and missing energy final states in 9.7fb^{-1} of $p\bar{p}$ collisions at $\sqrt{s} = 1.96$ tev. *Phys. Rev. D*, 88(052006), 2013.

[39] ATLAS Collaboration. Measurement of the w^+w^- cross sections in $\sqrt{s} = 7$ tev pp collisions with the atlas detector and limits on anomalous gauge couplings. *Physics Letters B*, 712(4-5), 2012.

[40] ATLAS Collaboration. Measurement of the w^+w^- production cross section in proton-proton collisions at $\sqrt{s} = 8$ tev with the atlas detector, 2014. ATLAS-CONF-2014-033.

[41] CMS Collaboration. Measurement of the w^+w^- cross section in pp collisions at $\sqrt{s} = 7$ tev and limits on anomalous $ww\gamma$ and wwz couplings. *The European Physical Journal C*, 73(2610), 2013.

[42] CMS Collaboration. Measurement of the w^+w^- and zz production cross sections in pp collisions at $\sqrt{s} = 8$ tev. *Physics Letters B*, 721(4-5), 2013.

[43] D0 Collaboration. Measurement of the ww production cross section with dilepton final states in $p\bar{p}$ collisions at $\sqrt{s} = 1.96$ tev and limits on the anomalous trilinear gauge couplings. *Physical Review Letters*, 103(191801), 2009.

[44] J. Campbell and K. Ellis. Mcfm - monte carlo for femtobarn processes, 2005. http://mcfm.fnal.gov/.

[45] S. Kallweit P. Maierhofer A. von Manteuffel S. Pozzorini D. Rathlev T. Gehrmann, M. Grazzini and L. Tancredi. w^+w^- production at hadron colliders in nnlo qcd, 2014. arXiv:1408.5243v1 [hep-ph].

[46] L3 ALEPH, DELPHI and The LEP Working Group for Higgs Boson Searches OPAL Collaborations. *Phys. Lett. B*, 565(61), 2003.

[47] the Tevatron New Phenomena Higgs Working Group The CDF, D0 Collaborations. Combined cdf and d0 upper limits on standard model higgs boson production with up to 8.6fb^{-1} of data, 2011. FERMILAB-CONF-11-354-E.

[48] CMS Collaboration. Combined results of searches for the standard model higgs boson in pp collisions at $\sqrt{s} = 7$ tev. *Phys. Lett. B*, 710, 2012.

[49] ATLAS Collaboration. Combined search for the standard model higgs using up to 4.9fb^{-1} of pp collision data at $\sqrt{s} = 7$ tev with the atlas detector at the lhc. *Phys. Lett. B*, 710, 2012.

[50] ATLAS Collaboration. Observation of a new particle in the search for the standard model higgs boson with the atlas detector at the lhc. *Phys. Lett. B*, 716, 2012.

[51] CMS Collaboration. Observation of a new boson at a mass of 125 gev with the cms experiment at the lhc. *Phys. Lett. B*, 716, 2012.

[52] CDF Collaboration.

[53] CDF Collaboration. *Nucl. Instrum. Methods A*, 526(249), 2004.

[54] B. Webber. Parton shower monte carlo event generators. Scholarpedia 6(12):10662.

[55] J. Huston H.L. Lai P. Nadolsky W.K. Tung J. Pumplin, D. R. Stump. New generation of parton distributions with uncertainties from global qcd analysis. *J. High Energy Phys.*, 0207(012), 2002.

[56] G. Ingelman B. Andersson, G. Gustafson and T. Sjostrand. Parton fragmentation and string dynamics. *Phys. Rept.*, 97, 1983.

[57] G. Corcella et. al. *JHEP*, 0101(010), 2001.

[58] M. L. Mangano, 2004. mlm.web.cern.ch/mlm/talks/lund-alpgen.pdf.

[59] D. Brun and F. Carminati. Cern program library long writeup w5013, 1993. unpublished.

[60] T. Han U. Baur and J. Ohnemus. *Phys. Rev. D*, 57(2823), 1998.

[61] J. M. Campbell and R. K. Ellis. *Phys. Rev. D*, 60(113006), 1999. hep-ph/9905386.

[62] P. Fiedler M. Czakon and A. Mitov. Total top-quark pair-production cross section at hadron colliders through $o(\alpha_s^4)$. *Phys. Rev. Lett.*, 110(252004), 2013.

[63] T. Aaltonen et al. (CDF Collaboration). Combination of measurements of the top-quark pair production cross section from the tevatron collider. *Phys. Rev. D*, 89(072001), 2014.

[64] N. Kauer T. Binoth, M. Ciccolini and M. Kramer. *J. High Energy Phys.*, 03(065), 2005.

[65] D. de Florian G. Bozzi, S. Catani and M. Grazzini. *Phys. Lett. B*, 564(65), 2003.

[66] D. de Florian G. Bozzi, S. Catani and M. Grazzini. *Nucl. Phys. B*, 737(73), 2006.

[67] J. Kalinowski A. Djouadi and M. Spira. *Comput. Phys. Commun.*, 108(56), 1998.

[68] S. Dittmaier A. Bredenstein, A. Denner and M. Weber. *Phys. Rev. D*, 74(013004), 2006.

[69] S. Dittmaier A. Bredenstein, A. Denner and M. Weber. *J. High Energy Phys.*, 02(080), 2007.

[70] D. Acosta et al. (CDF Collaboration). *Phys. Rev. D*, 71(052003), 2005.

[71] T. Junk M. Kirby R. Snider et al. T. Phillips, J. Freeman. Introduction to hobit, a b jet identification tagger at the cdf experiment optimized for light higgs searches, 2012. CDF/DOC/CDF/PUBLIC/10803.

[72] M. Feindt and U. Kerzel. *Nucl. Instrum. Methods A*, 559(190), 2006.

[73] R. G. Roberts. W. J. Stirling A. D. Martin and R. S. Thorne. *Eur. Phys. J. C*, 28(455), 2003.

[74] F. Maltoni. http://maltoni.home.cern.ch/maltoni/TeVrLHC/SM.html.

[75] S. Catani and M. Grazzini. *Phys. Rev. Lett.*, 98(222002), 2007.

[76] M. Grazzini. *JHEP*, 0802(043), 2008.

[77] M. Grazzini. http://theory.fi.infn.it/grazzini/codes.html.

[78] D. Acosta et al. (CDF Collaboration). *Nucl. Instrum. Methods A*, 494(57), 2002.

[79] P. Nadolsky et al. *Phys. Rev. D*, 78(013004), 2008.

[80] A. Bhatti et al. (CDF Collaboration). Determination of the jet energy scale at the collider detector at fermilab. *Nucl. Inst. A*, 566(2), 2006.

[81] J. S. Conway. Incorporating nuisance parameters in likelihoods for multisource spectra, 2011. data-an/1103.0354v.

[82] F. James and M. Roos. Minuit - a system for function minimization and analysis of the parameter errors and correlations. *Computer Physics Communications*, 10(6), 1975.

[83] T. Adye. Unfolding algorithms and tests using roounfold, 2011. data-an/1105.1160.

[84] T. Aaltonen et al. (CDF Collaboration). Searches for the higgs boson decaying to $w^+w^- \to l^+\nu l^-\bar{\nu}$ with the cdf ii detector. *Physical Review D*, 88(052012), 2013.

[85] The CDF and D0 Collaboration. Higgs boson studies at the tevatron. *Phys. Rev. D*, 88(052014), 2013.